Investigation of artificial electromagnetic structures in terms of lattice symmetry and self-complementarity

Yosuke Nakata
Department of Electronic Science and Engineering
Kyoto University

A thesis submitted for the degree of
Doctor of Engineering

Contents

Chapter 1

Introduction

1.1 Background

In the 19th century, James Clerk Maxwell postulated electromagnetism as a field theory and predicted that the oscillations of electric and magnetic fields propagate as waves. He found that the speed of electromagnetic waves equals that of light and concluded that light itself is an electromagnetic wave. The existence of electromagnetic waves was experimentally confirmed by Heinrich Rudolf Hertz. Since these discoveries, people have applied them in various ways, such as radio communication, radar technology, and traditional optics. Now, electromagnetic waves are playing a critical role in modern society, e.g. information technologies.

Even though electromagnetism's theoretical foundation was formulated more than 100 years ago, many complicated electromagnetic wave scattering problems remain. The degrees of freedom for scatter are infinite; we can freely choose their materials, geometrical shapes, and locations. Such infinite situations can provide various unusual electromagnetic phenomena, which are completely different from our intuitions.

One such unusual phenomena was reported in 1998 by Ebbesen [1], who found that the optical transmission of subwavelength periodic hole arrays (Fig. 1.1) is much higher than single-hole transmission. This phenomenon, which is called extraordinary optical transmission (EOT), cannot be explained by Bethe theory [2] and is considered a cooperative phenomenon.

EOT has the same origins as the diffraction anomaly in gratings [3]. In the early 19th century, Wood reported anomalous light scattering by gratings [4, 5]: the drop from maximum illumination to minimum occurred within a range of wavelengths. This

is called Wood's anomaly and is explained as follows [6]: (i) the lattice interaction shows divergent behavior when a diffracted beam grazes the gratings, and sharp minima of the spectra are observed, and (ii) a lattice resonance can occur at a wavelength to the red of this condition, causing broad maxima of the spectra near the sharp minima. In this theory, we must determine the interaction among the wires, because the lattice resonances and the grazing conditions are modified by the interaction.

At the early stage of EOT research, researchers attributed EOT to coupling through surface plasmon polaritons. However, further studies have revealed that the diffracted field is not only a surface plasmon [7–9]. These researches show that it is hard to understand the physical origin of the phenomena even for such simple hole arrays.

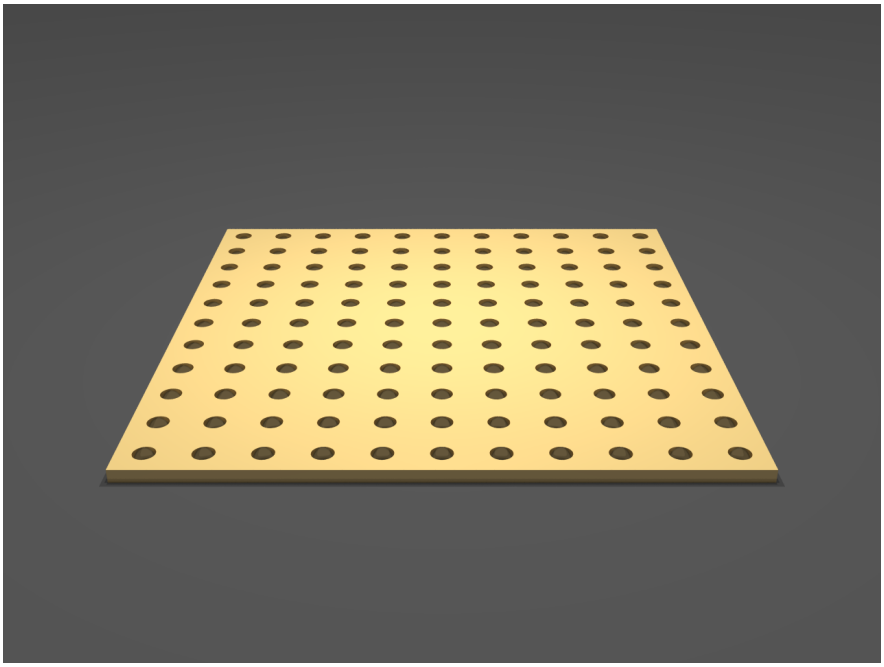

Figure 1.1: Hole array - Holes are periodically perforated in a metal film.

Periodic structures that resemble hole arrays have also been investigated from another perspective. The spontaneous emission in dielectric periodic structures and the energy bands for photons were studied in the 1970s and 1980s [10–13]. Around the same time, strong localization in a disordered dielectric periodic structure was reported by John [14]. After these publications, John and Yablonovitch discussed their ideas and decided to use the word photonic crystal to describe such structures. Since the birth of photonic crystals, the number of research papers on them has grown exponentially.

The eigenmodes of photonic crystals with permittivity $\varepsilon(\boldsymbol{r})$ that varies in space is determined by the following equation [15]:

$$\hat{\Theta}\tilde{\boldsymbol{H}}(\boldsymbol{r}) = \left(\frac{\omega}{c_0}\right)^2 \tilde{\boldsymbol{H}}(\boldsymbol{r}), \tag{1.1}$$

$$\hat{\Theta} = \nabla \times \frac{1}{\varepsilon(\boldsymbol{r})}\nabla\times, \tag{1.2}$$

where magnetic field $\boldsymbol{H}(\boldsymbol{r}, t)$ is represented by $\tilde{\boldsymbol{H}}(\boldsymbol{r})\mathrm{e}^{-\mathrm{i}\omega t} + \text{c.c.}$ with angular frequency ω and c_0 is the vacuum speed of light. Here, c.c. means the complex conjugate. These equations are analogous to the time-independent Schrödinger equation:

$$\hat{H}\Psi(\boldsymbol{r}) = \mathcal{E}\Psi(\boldsymbol{r}), \tag{1.3}$$

$$\hat{H} = -\frac{\hbar^2}{2m}\Delta + V(\boldsymbol{r}), \tag{1.4}$$

with eigenenergy $\mathcal{E}$, mass m, and potential $V(\boldsymbol{r})$. Comparing Eqs. (1.1) and (1.2) with Eqs. (1.3) and (1.4), we can see that permittivity $\varepsilon(\boldsymbol{r})$ plays a role similar to potential $V(\boldsymbol{r})$ of the Schrödinger equation. Periodic dielectric structures can be regarded as "crystals for photons." The terminology of *photonic crystal* is based on this analogy. The concepts of reciprocal space, Brillouin zones, dispersion relations, Bloch wave functions, and band gaps can be applied to the optical waves in photonic crystals.

The first try for experimental demonstration of the photonic band gap was done by Yablonovitch, but it was a pseudogap, which means the forbidden frequency range shrank to zero for certain directions of radiation [16]. The true band gap was realized by Yablonovitch in 1991 [17]. These studies were performed in the microwave regime, in which the wavelength of the electromagnetic waves is $\sim 30\,\mathrm{cm}$, because fabricating photonic crystals is easy. In 1996, Krauss made two-dimensional photonic crystals for the optical regime utilizing a semiconductor industry technique [18].

If we introduce a point defect to a photonic crystal, we can realize a photonic crystal cavity in which light is strongly confined. The sophisticated designs of photonic crystal cavities enable us to realize very high quality factors [19]. The possibility of photonic crystals with ultra high theoretical Q factors that range from 10^7 to 10^8 was theoretically predicted [20], and those with $Q \sim 3 \times 10^6$ were experimentally demonstrated [21].

In the vicinity of the edge of the Brillouin zone, the group velocity of the photon is greatly reduced [22]. This phenomenon is applicable to store light and leads to enhanced light-matter interaction to increase the sensitivity of sensors.

Such artificial electromagnetic structures as metallic hole arrays and photonic crystals lead to a new concept: metamaterial. In March 2000, an invited session called "Metamaterials" was held at the APS meeting where M. Walser gave a talk about the concept of metamaterials [23]. The session included topics on photonic crystals [24], sculptured thin films [25], nanocrystal superlattices [26], artificial dielectric and magnetic molecules [27]. Attendees discussed heterogeneous materials to realize new responses precluded by physics constraints from occurring in the constituent materials[1]. Seven months after the meeting, Smith *et al.* published a paper on negative refractive indexes and used the phrase "left-handed metamaterial" to describe artificial materials with a negative refractive index [28]. In this paper, he used the word metamaterial only in title and abstract.

Negative refractive index materials were first introduced by Veselago in 1964 [29]. He theoretically investigated the electromagnetic wave propagation in a medium with both negative ε and μ. Applying $\nabla\times$ to Faraday's law $\nabla \times \boldsymbol{E} = -\partial \boldsymbol{B}/\partial t$, we obtain

$$\left(-\varepsilon\mu\frac{\partial^2}{\partial t^2} + \Delta\right)\boldsymbol{E} = 0, \tag{1.5}$$

where we use Gauss's law $\nabla \cdot \boldsymbol{D} = 0$. If $\varepsilon\mu > 0$ is satisfied, Eq. (1.5) corresponds to a wave equation and electromagnetic waves can propagate. For $\varepsilon\mu > 0$, there are two cases where both can be either positive or negative[2]. Using Faraday's law and Maxwell-Ampère's law for the plane wave with $\boldsymbol{E} = \check{\boldsymbol{E}}\mathrm{e}^{\mathrm{i}(\boldsymbol{k}\cdot\boldsymbol{x}-\omega t)}$+c.c. and $\boldsymbol{H} = \check{\boldsymbol{H}}\mathrm{e}^{\mathrm{i}(\boldsymbol{k}\cdot\boldsymbol{x}-\omega t)}$+c.c., we have

$$\boldsymbol{k} \times \check{\boldsymbol{E}} = \mu\omega\check{\boldsymbol{H}}, \tag{1.6}$$

$$\boldsymbol{k} \times \check{\boldsymbol{H}} = -\varepsilon\omega\check{\boldsymbol{E}}. \tag{1.7}$$

[1] The title of Yablonovitch's talk was "Photonic Bandgap Structures as Meta-Materials" [24]. Therefore, photonic crystals were considered metamaterials.

[2] We assume both ε and μ are real. When we allow them to have imaginary values, a positive and negative imaginary pair can lead to wave propagation. If the loss and gain are balanced, the energy of the waves does not increase or decrease in the propagation.

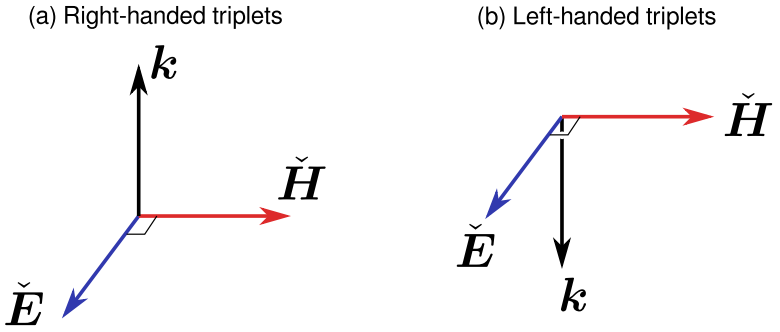

Figure 1.2: Right-handed and left-handed triplets - $\check{\boldsymbol{E}}$, $\check{\boldsymbol{H}}$, and $\boldsymbol{k}$ in (a) usual materials and (b) left-handed materials.

We assume that $\check{\boldsymbol{E}}$ and $\check{\boldsymbol{H}}$ are real vectors, whose components are real values. That is, a wave with a linear polarization is considered. In the usual materials with $\varepsilon > 0$ and $\mu > 0$, $\check{\boldsymbol{E}}$, $\check{\boldsymbol{H}}$, and $\boldsymbol{k}$ form right-handed triplets [Fig.1.2(a)]. In materials with $\varepsilon < 0$ and $\mu < 0$, $\check{\boldsymbol{E}}$, $\check{\boldsymbol{H}}$, and $\boldsymbol{k}$ form left-handed triplet vectors [Fig.1.2(b)], so a medium with both negative ε and μ are called "left-handed" materials. Compared with standard "right-handed" materials, the phase velocity in a left-handed material points in the opposite direction to Poynting vector $\check{\boldsymbol{E}} \times \check{\boldsymbol{H}}^*$. This leads to anomalous refraction between right-handed and left-handed materials. Consider a negative refractive index material placed in $y \leq 0$ (Fig. 1.3). The plane wave with wave vector $\boldsymbol{k}_\mathrm{i}$ is irradiated from $y \geq 0$. We set the x axis parallel to the projected vector of $\boldsymbol{k}_\mathrm{i}$ onto $y = 0$. It is refracted through $y = 0$, and the wave vector of the transmitted wave in $y \leq 0$ is represented by $\boldsymbol{k}_\mathrm{t}$. From the boundary condition, the x component of $\boldsymbol{k}_\mathrm{i}$ equals that of $\boldsymbol{k}_\mathrm{t}$. Because the y component of Poynting vector $\boldsymbol{E} \times \boldsymbol{H}$ is negative in $y \leq 0$, the y component of $\boldsymbol{k}_\mathrm{t}$ must be positive. Then the wave is refracted at the interface in the reverse sense to normal expectations. Here, the angle of incidence is denoted by θ_i. The angle of refraction θ_t represents the angle between the Poynting vector and $-\boldsymbol{e}_y$ in $y \leq 0$, where $\boldsymbol{e}_y$ is an unit vector along the y axis. Therefore, the Poynting vector is denoted by $\boldsymbol{S} = |\boldsymbol{S}|(\sin\theta_\mathrm{t}, -\cos\theta_\mathrm{t})$, where $\theta_\mathrm{t} > 0$ represents normal refraction. Snell's law is usually given by

$$n_1 \sin\theta_\mathrm{i} = n_2 \sin\theta_\mathrm{t}, \tag{1.8}$$

where n_1 is the refractive index in $y \geq 0$ and n_2 is that in $y \leq 0$. If we assume Eq. (1.8) for the refraction between the right-handed and left-handed materials shown in Fig. 1.3,

n_1 is positive and n_2 must be negative because of $\theta_t < 0$. The refractive index of a left-handed material can be described as negative.

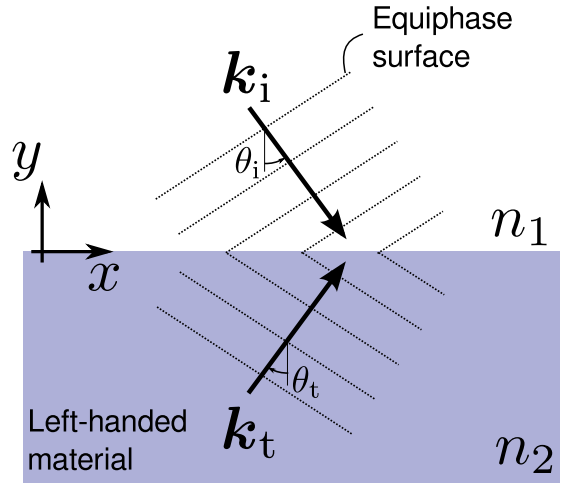

Figure 1.3: Negative refraction - Anomalous refraction occurs between right-handed and left-handed materials.

In addition to the negative refraction, the reversal of the Doppler shift, the Cherenkov radiation, and even the radiation pressure were also predicted in the left-handed materials by Veselago. Although some materials show $\mu < 0$, no material with negative permeability and low losses that coexist with a negative ε was found before the 21st century. To resolve this problem, Smith *et al.* devised a new strategy that utilized two artificial structures for tuning ε and μ.

Relative permittivity $\epsilon(\omega)$ of a metal is described by the Drude model:

$$\epsilon(\omega) = 1 - \frac{\omega_p^2}{\omega^2}. \tag{1.9}$$

Here, ω_p is the plasma frequency, which is in the ultraviolet frequency range in most metals. In 1996, Pendry *et al.* showed that metallic wire arrays are an effective media that obeys the Drude model in the long-wavelength regime [30]. These effective media can have extreme low plasma frequency, and ω_p can be tuned by their geometrical parameters, such as the distance among wires.

Usually, the magnetic responses of materials are much smaller than the electrical ones. For increasing the magnetic response, Pendry *et al.* proposed a novel metallic structure called a split-ring resonator (SRR) [31]. An example of a metal SRR is shown in Fig.1.4(a). SRRs are usually aligned periodically [Fig.1.4(b)]. An SRR can

be considered an LC circuit composed of an inductor (part of a wire coil) and a capacitor that is formed by two wires. It exhibits LC resonance at the resonant frequency when a time-varying magnetic field is normally applied to the plane where the ring is placed. The current induced by the oscillating magnetic field produces a magnetic moment.

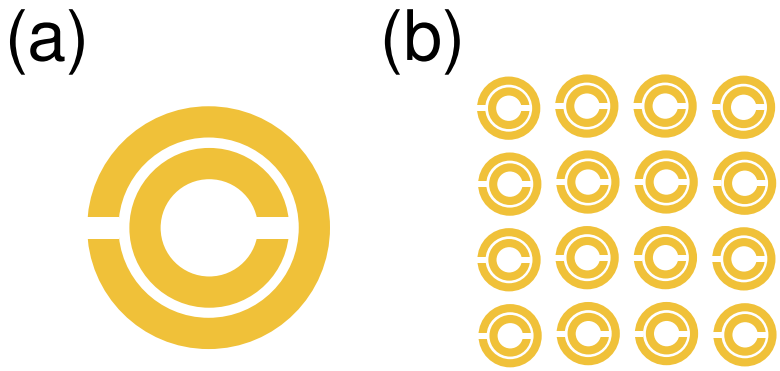

Figure 1.4: Split ring resonators - (a) Example of split ring resonator (SRR); (b) Typically, SRRs are aligned periodically.

SRRs that are isotropically aligned in 3-dimensional space can be described as effective media with magnetic permeability μ in the long-wavelength regime. At a frequency just above the resonance, the induced magnetic moment has the opposite direction to the incident magnetic field, and $\mu < 0$ is realized.

In 2000, Smith *et al.* combined SRRs with wire arrays and simultaneously realized a metamaterial with $\varepsilon < 0$ and $\mu < 0$ [28, 32]. By using a similar metamaterial, Shelby *et al.* demonstrated negative refraction in 2001 [33]. These metamaterials were designed to perform in the microwave frequency where their fabrication is much easier than in other frequency ranges. In 2008, Valentine *et al.* demonstrated negative refraction at an interface using a wedge prism at telecommunication wavelengths [34].

Veselago pointed out an application of negative refraction to a lens in his paper [29]. He considered the left-handed material slab with negative refractive index $n = -1$ [Fig. 1.5]. The slab is placed in $d_1 \leq z \leq d_1 + d_2$. The light emitted at $z = 0$ is refracted by the first interface on the slab with width d_2 and collected at $z = 2d_1$. Then, since the second refraction focuses the light at $z = 2d_2$, the left-handed slab can act as a flat lens.

Pendry theoretically investigated Veselago's lens with $\varepsilon = -\varepsilon_0$ and $\mu = -\mu_0$, where ε_0 and μ_0 are vacuum permittivity and permeability, respectively. Conventional imag-

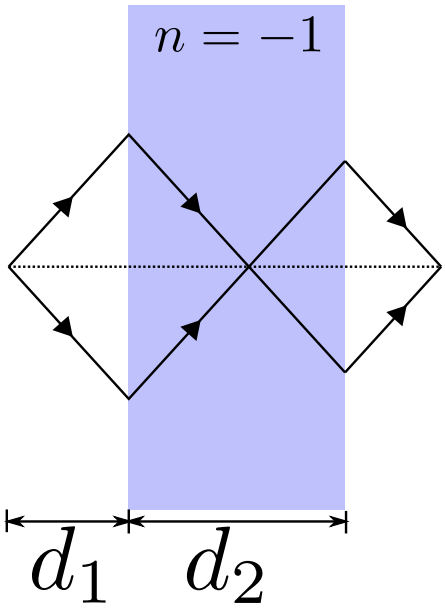

Figure 1.5: Veselago's lens - Left-handed metamaterial slab with $n = -1$ acts as lens.

ing systems with a lens cannot collect high-spatial-frequency components with in-plane wave vector $k_\perp > \omega/c$ because a wave having $k_\perp$ on xy plane decays exponentially along the optical axis (z axis). Pendry showed that the left-handed slab with $\varepsilon = -\varepsilon_0$ and $\mu = -\mu_0$ can "amplify" the evanescent components to realize a perfect lens [35]. Therefore, such a lens is called a "superlens." In the microwave regime, Lagarkov *et al.* experimentally demonstrated the superlens [36], and Aydin *et al.* achieved higher resolution [37].

In the optical regime, it is hard to fabricate a superlens with both $\varepsilon = -\varepsilon_0$ and $\mu = -\mu_0$. To resolve this problem, Pendry also proposed a feasible superlens using only a silver. If the metamaterial slab is very thin, the electric and magnetic fields can be decoupled. Therefore, only $\varepsilon = -\varepsilon_0$ is sufficient for the particular polarization of the incident wave. Similar experiments of optical superlens with ultraviolet (UV) illumination were performed by Melville *et al.* [38–40] and Fang *et al.* [41], and Lee *et al.* improved Fang's result [42]. In the mid-infrared regime, Hillenbrand's group used SiC as the material with $\varepsilon < 0$ and realized a superlens [43, 44].

Pendry also considered the extension of a superlens slab to a cylindrical one using conformal maps [45], and Pendry and Ramakrishna revealed that a cylindrical superlens can magnify the image [46]. To realize cylindrical superlens, in 2006 two groups theoret-

ically proposed an anisotropic layered metamaterial with hyperbolic dispersion [47, 48]. Such a cylindrical medium is called a "hyperlens" because it utilizes a hyperbolic dispersion. In the hyperlens, large transverse wave vectors are gradually compressed as they propagate outwards. Then, the evanescent components are converted into propagating waves. In 2007, Liu *et al.* fabricated a hyperlens, which consisted of a curved periodic stack of Ag (35 nm) and Al_2O_3 (35 nm) deposited on a half-cylindrical cavity on a quartz substrate, and demonstrated a magnifying effect [49]. A different approach for a magnifying superlens for two-dimensional surface plasmons was demonstrated using a concentric polymer grating placed on a metal surface [50].

As described above, researchers have found that there is a remaining degree of freedom to control the electromagnetic waves beyond customary optics. In 2006, two groups independently proposed a novel strategy based on transformation to realize cloaking devices. Leonhardt constructed a cloaking devise based on the invariance of the two-dimensional Helmholtz equation under a conformal map [51]. He utilized the Zhukovski transform, which maps from the Riemann surface with two Riemann leaves into the complex plane, and calculated the refractive index distributions for cloaking [52]. On the other hand, the construction by Pendry *et al.* is based on the invariant property of the Maxwell equations. First, we addressed light propagation in a vacuum. Next, we applied a coordinate transformation, such as

$$r' = \begin{cases} R_1 + r\frac{R_2 - R_1}{R_2} & (r < R_2) \\ r & (r \geq R_2) \end{cases}, \tag{1.10}$$

$$\theta' = \theta, \tag{1.11}$$

$$\phi' = \phi, \tag{1.12}$$

where R_1 is the radius of the cloaked region and $R_2 (> R_1)$ is the device's radius. This transformation is shown in Fig. 1.6. Under the coordinate transformation, Maxwell equations are invariant if we appropriately choose second rank tensors ε and μ. Then the region described by $r' < R_1$ is cloaked. In recent years, Pendry has also applied transformation to subwavelength plasmonic structures which can lead to energy harvesting [53].

Pendry's construction of cloaking devices can be clearly understood by the differential-form approach [54]. Equations $\mathrm{d}D = 0$, $\mathrm{d}H = \partial D/\partial t$, $\mathrm{d}B = 0$, and $\mathrm{d}E = -\partial B/\partial t$ are invariant under diffeomorphism. However, the metric is transformed as $g \to \tilde{g}$

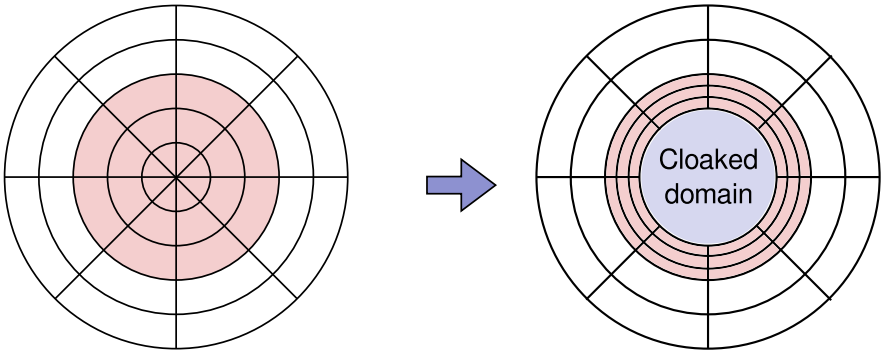

Figure 1.6: Pendry's construction of cloaking device - Red region is transformed.

under it. If we interpret constitutive equations with $(\varepsilon_0, \mu_0, \tilde{g})$ as those with (ε, μ, g), then transformed light propagation can be realized for materials with spatially varying anisotropic (ε, μ).

In the microwave regime, Schurig *et al.* fabricated a two-dimensional cylindrical cloaking device [55]. Although its invisibility is imperfect because of its practical realization, a cloaking effect was confirmed. For the optical regime, Cai *et al.* theoretically suggested a non-magnetic optical cloak with reduced material parameters [56]. Li *et al.* proposed another approach called an optical carpet cloak, whose device is designed to conceal an object placed under a curved reflecting surface that imitates the reflection of a flat surface. This device is constructed by a quasi-conformal map and is only composed of isotropic dielectric materials. The carpet cloak was first demonstrated in the microwave regime [57] and subsequently in the short-wavelength infrared range [58].

As well as three-dimensional metamaterials, two-dimensional metamaterials called metasurfaces have been extensively studied [59]. Similar periodic two-dimensional structures that act as filters in the microwave regime have also been developed to reduce the radar cross section of the large antenna of aircraft and are called frequency selective surfaces [60].

In 2011, Yu *et al.* experimentally studied the generalized Snell's law for metasurfaces [61]. Snell's law is usually written as Eq. (1.8). Here, we consider a metasurface placed on the interface between two media. The metasurface is assumed to be composed of elements spatially variant along the x axis. For this metasurface, Snell's law is generalized as follows:

$$n_1 \sin\theta_\mathrm{i} - n_2 \sin\theta_\mathrm{t} = \frac{\lambda_0}{2\pi}\frac{\mathrm{d}\Phi}{\mathrm{d}x}, \tag{1.13}$$

where Φ is the abrupt phase shift by the metasurface [61]. Yu *et al.* designed V-shaped nanoantennas as meta-atoms to tune the full 2π phase span. Using the metasurface composed of these meta-atoms, they demonstrated the generalized Snell's law for electromagnetic waves with wavelength of $8\,\mu$m. Ni *et al.* fabricated a smaller structure and demonstrated the generalized Snell's law for wavelengths ranging from 1.0 to $1.9\,\mu$m [62]. In spite of these successes, their metasurfaces have large reflection. To reduce it, Pfeiffer *et al.* proposed a new 2-dimensional structure with both designed electric and magnetic polarizabilities and demonstrated its effectiveness in the microwave regime [63]. Monticone *et al.* also proposed a feasible optical metasurface which leads to bending and focusing of light with unprecedented efficiency [64]. Their structures are composed of three layers, where each layer is composed of dielectric and plasmonic materials.

So far, we have described metamaterials for electromagnetic waves. However, note that the concept of metamaterials is not restricted to electromagnetism. Metamaterials enable us to tailor acoustic wave propagation, heat flow, mechanical elasticity, and even quantum matter wave propagation (for a review, see Ref. 65). These developments suggest a promising future for metamaterials.

1.2 Purpose and Outline of Thesis

As in other fields of physics, such as crystallography and atomic or molecular spectroscopy, symmetry plays a fundamental role in artificial structures. The symmetry of the shape or the alignment of meta-atoms affects the electromagnetic response of metamaterials. Then, it is very important to study them from the perspective of symmetry. A group-theoretical method of treating symmetry in metamaterials has been developed and applied for designing and optimizing metamaterials [66–69]. This method has also been utilized for designing metasurfaces [70, 71].

In this thesis, we study the role of symmetry for the electromagnetic response of artificial structures from two standpoints. The schematic figure of the contents is shown in Fig. 1.7. In Chap. 2, we investigate lattice symmetry with respect to the alignment of metallic structures (or meta-atoms). In Chap. 4, we theoretically study another symmetry called *self-complementarity*. The self-complementarity is the symmetry under the replacement of elements. The research of self-complementary

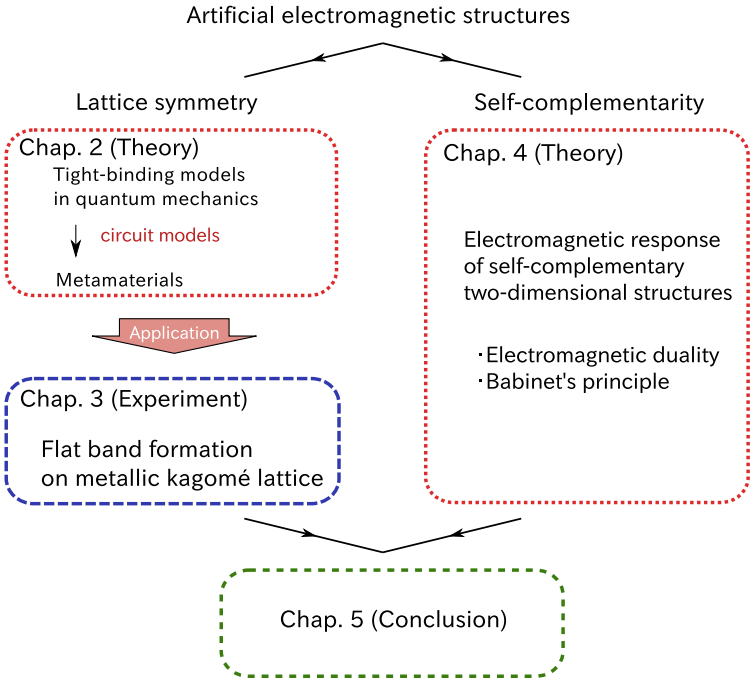

Figure 1.7: Contents - We study artificial electromagnetic structures from two standpoints: symmetry of lattice and self-complementarity.

structures from experimental standpoints will be reported by my coworker. In the following, we briefly describe each chapter.

Chapter 2: Tight-binding models in circuit theory

In this chapter, we consider a tight-binding model, which is often used in quantum mechanics. It treats the transfer of the probability amplitude of electrons from one nucleus to another. Coupling by hopping leads to such hybridization effects as multiple modes and continuum bands. By using tight-binding models, we can easily calculate the energy eigenvalues and eigenmodes. Energy bands critically affect the propagation of electrons. For designing electromagnetic propagation, constructing an analogy between tight-binding models and electromagnetic systems is very useful when we utilize lattice symmetry of metamaterials. This is because the band structures of electrons tightly bounded in various lattices have already been previously calculated. The analogy enables us to realize artificial electromagnetic structures with similar dispersion relations to quantum tight-binding models. To formulate the analogy, we consider electrical circuits, which include the essence of electromagnetic phenomena. First, we describe

the general framework to calculate the eigenvalues and the eigemodes in electrical circuits. Next, we propose two electrical circuits that obey the equations that resemble tight-binding models in quantum mechanics. We discuss artificial structures that can be described by our proposed circuit models. The band structures of several circuits are calculated with this analogy. In particular, we investigate flat-band formation for some specific lattices. This chapter is based on Ref. 72.

Chapter 3: Observation of flat band in metallic kagomé lattice

In this chapter, we experimentally demonstrate an electromagnetic flat band. In flat bands, the group velocity is slowed down in all directions. It is important to study the flat bands in electromagnetic systems in terms not only of fundamental physics but also from an application standpoint, such as slow light; however, there has been no experimental demonstration of electromagnetic flat bands. The dispersion relation of metallic kagomé lattices can become flat, as shown in the previous chapter. Then we focus on a metallic kagomé lattice and realize a flat band in the terahertz regime. This chapter is based on Ref. 73.

Chapter 4: Frequency-independent response of self-complementary metasurfaces

We theoretically study electromagnetic plane-wave scattering by self-complementary metasurfaces. Using Babinet's principle and extending it to metasurfaces with resistive elements, we show that frequency-independent transmission and reflection are realized for the normal incidence of a circularly polarized plane wave onto a self-complementary metasurface, even if there is diffraction. Next, we consider two special classes of self-complementary metasurfaces and show that those with rotational symmetry can act as coherent perfect absorbers and those with translational symmetry compatible with their self-complementarity can split the incident power equally, even for oblique incidences. This chapter is based on Ref. 74.

Chapter 2

Tight-binding models in circuit theory

2.1 Background

Although various unusual effects have been achieved in the field of metamaterials described in Chap. 1, their properties are mainly based on the averaged effects of resonant meta-atoms. That is to say, coupling effects were ignored in early researches of metamaterials. If there exist couplings among meta-atoms, hybridization effects such as multiple modes and continuum bands must be considered. Recently, hybridization effects in metamaterials have generated great interest (for a review, see Ref. 75). In this chapter, we theoretically seek the coupling effects caused by the lattice symmetry after describing the formulation.

For the dielectric photonic crystals, hybridization modes have been analyzed by using the analogy of tight-binding models in quantum mechanics [76–84]. A tight-binding model treats the transfer of electromagnetic energy from one resonator to another as electron hopping in atomic lattices. Recently, the tight-binding method has been applied to metallic systems such as metallophotonic waveguide networks [85], and metamaterials with nontrivial ε and μ [86, 87]. These treatments of hybridization modes in dielectric photonic crystals and metallic systems are based on eigenvalue problems of electromagnetic field quantities extending over the whole space, e.g. shown in Eq. (1.1).

When considering a metamaterial with metallic meta-atoms behaving as LC resonators, such as SRRs, it is much simpler to just consider the electric current or potential in the metallic structures as a basic quantity. This consideration leads to the

approach based on circuit theory. At first, circuit-theoretical approach seems to be less general than Eq. (1.1), but it can be derived exactly from the Maxwell equations [88]. Even optical devices can be designed by using the concept of circuits [89].

The first circuit model of a SRR was simply composed of an inductor and a conductor [90]. Shamonin *et al.* introduced the more accurate model of a SRR by using distributed circuits [91, 92], and it is very intriguing that the complex model can be finally reduced to a simple model. Even the simple model extracts qualitative characteristics. For the circuit-theoretical approach, we need not to look inside the detail if we are interested in the quantitative behavior. Then, we focus on the simple circuit models which can be implemented as metamaterials, and look for phenomena caused by the lattice symmetry. In particular, we treat circuit models composed of inductors and capacitors. Such networks are called *inductor–capacitor circuit networks*. The merit of using these models is that we can intuitively understand the resonance properties by using the circuit concepts such as inductance and capacitance, which are derived from the geometry of the metallic structure.

In the following sections of this chapter, we formulate a method to calculate the resonance condition of arbitrary inductor–capacitor circuit networks for analyzing hybridization modes in metamaterials and apply it to several circuit networks. Then, we establish an analogy between quantum-mechanical systems and electrical circuits. This analogy enables us to design dispersion relationships for metamaterials similar to those for quantum systems. By using this analogy, we can predict new phenomena in metamaterials.

2.2 Analysis method of resonances in inductor–capacitor circuit networks

In this section, we formulate general methods to analyze resonances in an arbitrary inductor–capacitor network, which can model metamaterials. For this purpose, we treat them in the frequency domain and describe all the variables by phasors (complex amplitudes). For example, sinusoidal voltage is represented as $v(t) = \tilde{V}\mathrm{e}^{-\mathrm{i}\omega t} + \mathrm{c.c.}$ with a phasor $\tilde{V}$. Although the time dependence of the variables is assumed to be $\exp(-\mathrm{i}\omega t)$, for impedance we also use the imaginary unit $\mathrm{j} = -\mathrm{i}$, following the convention in

electrical circuits. Here, the resonance condition is that there exists a nontrivial (non-zero) distribution of current or voltage that satisfies Kirchhoff's current law (KCL), Kirchhoff's voltage law (KVL), and all the voltage–current characteristics of the circuit elements.

In order to formulate this condition, we can make two choices of basic variables. The first choice is to use mesh currents satisfying KCL for the basic variables. The second is to use electrical potentials satisfying KVL for the basic variables. We discuss both methods, adapting the bra-ket notation. With this notation, we can perform calculations using the familiar methods of quantum mechanics.

2.2.1 Example

Before presenting the general method for analyzing inductor–capacitor circuit networks, we consider a simple example depicted in Fig 2.1. This example includes the essence of our method.

In Fig 2.1, complex currents $\tilde{J}_1$ and $\tilde{J}_2$ circulate along the two directed meshes α_1 and α_2. We can represent them by the vector $\tilde{\boldsymbol{J}} = [\tilde{J}_1 \ \tilde{J}_2]^{\mathrm{T}}$. The voltage drops along α_1, α_2 are denoted by $\tilde{\boldsymbol{V}} = [\tilde{V}_1 \ \tilde{V}_2]^{\mathrm{T}}$. The voltage drop vector $\tilde{\boldsymbol{V}}$ and the mesh current vector $\tilde{\boldsymbol{J}}$ are related as

$$\tilde{\boldsymbol{V}} = Z(\omega)\tilde{\boldsymbol{J}}. \tag{2.1}$$

The impedance matrix $Z(\omega)$ is given by

$$Z(\omega) = \begin{bmatrix} \mathrm{j}\omega L + 1/\mathrm{j}\omega C_{\mathrm{t}} & -1/\mathrm{j}\omega C' \\ -1/\mathrm{j}\omega C' & \mathrm{j}\omega L + 1/\mathrm{j}\omega C_{\mathrm{t}} \end{bmatrix}, \tag{2.2}$$

where $C_{\mathrm{t}}^{-1} = C^{-1} + C'^{-1}$. Due to the KVL, $\tilde{\boldsymbol{V}}$ must be zero. At resonant frequencies, $\tilde{\boldsymbol{J}} \neq 0$ is required. Then, we can formulate the resonance condition as follows:

$$\det Z = 0. \tag{2.3}$$

From Eq. (2.3), we obtain two modes: the in-phase mode of $\omega = \omega_0$ with the eigenvector $[1 \ 1]^{\mathrm{T}}$ and the anti-phase mode of $\omega = \omega_0\sqrt{1+2\eta}$ with the eigenvector $[1 \ -1]^{\mathrm{T}}$, where $\omega_0 = 1/\sqrt{LC}$, $\eta = C/C'$.

We can solve the same problem by using electrical node potentials instead of mesh currents. The node G is considered as the ground with zero potential. We denote complex electrical potentials at P, Q, and R as $\tilde{\phi}_{\mathrm{P}}$, $\tilde{\phi}_{\mathrm{Q}}$, and $\tilde{\phi}_{\mathrm{R}}$, respectively. They are

represented by the vector $\tilde{\boldsymbol{\phi}} = [\tilde{\phi}_{\mathrm{P}}\ \tilde{\phi}_{\mathrm{Q}}\ \tilde{\phi}_{\mathrm{R}}]^{\mathrm{T}}$. Divergence of currents at P, Q, and R are represented by $\tilde{\boldsymbol{D}} = [\tilde{D}_{\mathrm{P}}\ \tilde{D}_{\mathrm{Q}}\ \tilde{D}_{\mathrm{R}}]^{\mathrm{T}}$. The vector $\tilde{\boldsymbol{D}}$ is linearly dependent on $\tilde{\boldsymbol{\phi}}$ as $\tilde{\boldsymbol{D}} = Y(\omega)\tilde{\boldsymbol{\phi}}$. The admittance matrix $Y(\omega)$ is given by

$$Y(\omega) = \begin{bmatrix} \mathrm{j}\omega C + 1/(\mathrm{j}\omega L) & -\mathrm{j}\omega C & 0 \\ -\mathrm{j}\omega C & 2\,\mathrm{j}\omega C + \mathrm{j}\omega C' & -\mathrm{j}\omega C \\ 0 & -\mathrm{j}\omega C & \mathrm{j}\omega C + 1/(\mathrm{j}\omega L) \end{bmatrix}. \tag{2.4}$$

The KCL demands that $\tilde{\boldsymbol{D}}$ is zero. From $\det Y(\omega) = 0$, we have two modes with $\omega = \omega_0$ and $\omega = \omega_0\sqrt{1+2\eta}$. These are the same modes which we have obtained.

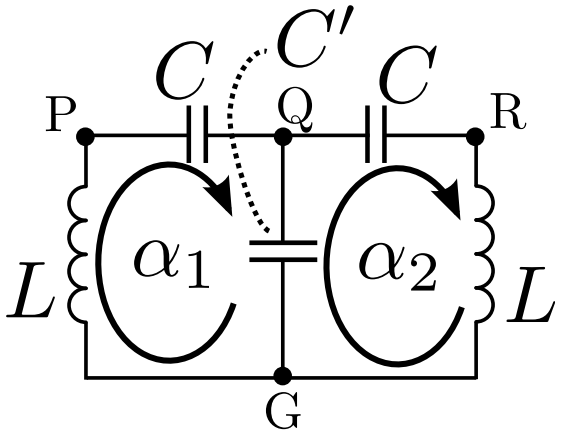

Figure 2.1: A simple example of inductor–capacitor circuit network - P, Q, R, and G are nodes and α_1 and α_2 are meshes.

2.2.2 Mesh current method

In this subsection, we firstly use mesh currents for the basic variables. A mesh current is a current along a mesh (or loop) in an inductor–capacitor circuit network and always satisfies KCL. All current distributions can be represented by the (complex) mesh currents. We denote all independent directed meshes in the circuit network as $\{\alpha_i | i = 1, 2, \cdots\}$ and the mesh current along α_i as $\tilde{J}_i$. Introducing the Hilbert space $\mathcal{H}$ with the orthonormal basis $\{|\alpha_i\rangle | i = 1, 2, \cdots\}$, we can express the current distribution as $|\Psi\rangle = \sum_i \tilde{J}_i |\alpha_i\rangle$, which corresponds to the set of basic variables satisfying KCL.

Secondly, we consider the (complex) voltage drop $\tilde{V}_i$ along α_i. Given a current distribution $|\Psi\rangle$, the voltage distribution $|\Lambda\rangle = \sum_i \tilde{V}_i |\alpha_i\rangle$ is determined. This relation is expressed as $|\Lambda\rangle = \hat{Z}(\omega)|\Psi\rangle$, where ω is the angular frequency and $\hat{Z}(\omega)$ is a linear operator. Because we consider only metamaterials with perfect conductors and

ignore resistances, $\hat{Z}(\omega)$ is skew-Hermitian. The impedance operator $\hat{Z}(\omega)$ contains information on the characteristics of the circuit elements and circuit topology.

Finally, requiring that KVL be satisfied, we obtain the following equation:

$$\hat{Z}(\omega)|\Psi\rangle = 0. \tag{2.5}$$

If there exists a non-zero solution $|\Psi\rangle \neq 0$, it represents a resonance of the circuit. We note that there are no external current and voltage sources. The condition of resonance is that $\hat{Z}(\omega)$ is singular. For circuits with a finite number of elements, $\det[\hat{Z}(\omega)] = 0$ must be satisfied for the resonant frequencies. The current distributions of the resonant modes are the eigenvectors of $\hat{Z}(\omega)$ with eigenvalue zero.

2.2.3 Node potential method

In this subsection, we use electrical potentials for the basic variables. KVL is always satisfied because the voltage drop is determined by the difference of the electrical potential. We can add any constant to the potential because the voltage drops do not change. In order to remove this constant ambiguity of potentials, we assume the potential of a node in each connected component is zero. The node with zero potential is called ground. Here, we denote the electrical potential as $\tilde{\phi}_i$ at π_i, where $\{\pi_i | i = 1, 2, \cdots\}$ are all the nodes except for the grounds. Like in the mesh current method, we introduce a Hilbert space $\mathcal{K}$ with the orthonormal basis $\{|\pi_i\rangle | i = 1, 2, \cdots\}$ and represent the potential distribution as $|\Phi\rangle = \sum_i \tilde{\phi}_i |\pi_i\rangle$, which corresponds to the set of basic variables satisfying KVL.

Now, we consider the current divergence $\tilde{D}_i$ at π_i. We define the current divergence distribution $|\Omega\rangle = \sum_i \tilde{D}_i |\pi_i\rangle$, and $|\Omega\rangle$ is determined by $|\Phi\rangle$ as $|\Omega\rangle = \hat{Y}(\omega)|\Phi\rangle$, where $\hat{Y}(\omega)$ is a skew-Hermitian operator due to resistances being ignored. The admittance operator $\hat{Y}(\omega)$ contains information on the characteristics of the circuit elements and the circuit topology.

Finally, KCL requires $|\Omega\rangle = 0$, and we formulate the circuit problem as follows:

$$\hat{Y}(\omega)|\Phi\rangle = 0. \tag{2.6}$$

For a finite number of circuit elements, $\det[\hat{Y}(\omega)] = 0$ must be satisfied at the resonant frequencies. The potential distributions of the resonant modes are the eigenvectors of $\hat{Y}(\omega)$ with eigenvalue zero.

2.3 Analysis method of resonances in periodic inductor–capacitor circuits

In this section, we consider a *periodic* inductor–capacitor circuit network with translational symmetry like in a crystal. The symmetry can be described by lattice vectors $\{\boldsymbol{a}_1, \boldsymbol{a}_2, \boldsymbol{a}_3\}$. The reciprocal lattice vectors $\{\boldsymbol{b}_1, \boldsymbol{b}_2, \boldsymbol{b}_3\}$ satisfy $\boldsymbol{a}_i \cdot \boldsymbol{b}_j = 2\pi\delta_{ij}$. Here, we consider 3-dimensional symmetry for concreteness, but the extensions to the 1- and 2-dimensional cases are very easy. We first apply the mesh current method. We choose one unit cell of the circuit as the origin and denote the unit circuit displaced by $\boldsymbol{x}_{lmn} = l\boldsymbol{a}_1 + m\boldsymbol{a}_2 + n\boldsymbol{a}_3$ from the origin as *the* (l, m, n)*-unit*, for $(l, m, n) \in \mathbb{Z}^3$. We express the independent meshes in (l, m, n)-units as $\alpha^s_{(l,m,n)}$ $(s = 1, 2, \cdots, S_{\text{mesh}})$, where S_{mesh} is the number of independent meshes in a unit circuit. We introduce the translation operators $\hat{T}_{(p,q,r)}$:

$$\hat{T}_{(p,q,r)}|\alpha^s_{(l,m,n)}\rangle = |\alpha^s_{(l+p,m+q,n+r)}\rangle, \tag{2.7}$$

for $(p, q, r) \in \mathbb{Z}^3$. The translational symmetry of the lattice gives $[\hat{Z}(\omega), \hat{T}_{(p,q,r)}] = 0$. Therefore, we can diagonalize $\hat{Z}(\omega)$ and $\hat{T}_{(p,q,r)}$ simultaneously. We first diagonalize $\hat{T}_{(p,q,r)}$ with the following plane-wave basis:

$$|\psi^s_{\boldsymbol{k}}\rangle = \frac{1}{\sqrt{V_G}} \sum_{(l,m,n)\in\mathbb{Z}^3} \exp(\mathrm{i}\boldsymbol{k} \cdot \boldsymbol{x}_{lmn})|\alpha^s_{(l,m,n)}\rangle, \tag{2.8}$$

where $\boldsymbol{k}$ is a wave vector and V_G is the volume of the first Brillouin zone. The orthonormal condition is satisfied as

$$\langle\psi^s_{\boldsymbol{k}}|\psi^{s'}_{\boldsymbol{k}'}\rangle = \sum_{(l,m,n)\in\mathbb{Z}^3} \delta_{ss'}\delta(\boldsymbol{k} - \boldsymbol{k}' - l\boldsymbol{b}_1 - m\boldsymbol{b}_2 - n\boldsymbol{b}_3). \tag{2.9}$$

Because the impedance operator and translation operators commute with each other, $\hat{Z}(\omega)$ acts separately on each $\boldsymbol{k}$ subspace spanned by $\{|\psi^s_{\boldsymbol{k}}\rangle\}$. Thus, it is sufficient to solve Eq. (2.5) in each $\boldsymbol{k}$ subspace. Now, Eq. (2.5) is reduced to

$$\hat{Z}_{\boldsymbol{k}}(\omega)|\Psi_{\boldsymbol{k}}\rangle = 0, \tag{2.10}$$

where $\hat{Z}_{\boldsymbol{k}}(\omega)$ is the restricted operator of $\hat{Z}(\omega)$ in the $\boldsymbol{k}$ subspace, and $|\Psi_{\boldsymbol{k}}\rangle$ is the state vector with wave vector $\boldsymbol{k}$. The matrix elements of $\hat{Z}_{\boldsymbol{k}}(\omega)$ can be calculated as

$$\left(\hat{Z}_{\boldsymbol{k}}(\omega)\right)_{s's} = \int_{1\text{st. B.Z.}} \mathrm{d}\boldsymbol{k}'\langle\psi^{s'}_{\boldsymbol{k}'}|\hat{Z}(\omega)|\psi^s_{\boldsymbol{k}}\rangle, \tag{2.11}$$

where 1st. B.Z. indicates the first Brillouin zone. Solving $\det[\hat{Z}_{\boldsymbol{k}}(\omega)] = 0$, we can obtain the dispersion relation of the circuit network. The eigenvectors of $\hat{Z}_{\boldsymbol{k}}(\omega)$ with zero eigenvalue represent the current distributions of the resonant modes.

Next we move to the node potential method. In this case, we exchange the roles of the mesh currents and node potentials, and the same discussion can be applied. Then, Eq. (2.6) reduces to

$$\hat{Y}_{\boldsymbol{k}}(\omega)|\Phi_{\boldsymbol{k}}\rangle = 0, \tag{2.12}$$

where $\hat{Y}_{\boldsymbol{k}}(\omega)$ is the restricted operator of $\hat{Y}(\omega)$ in the $\boldsymbol{k}$ subspace, and $|\Phi_{\boldsymbol{k}}\rangle$ is the state vector of wave vector $\boldsymbol{k}$. The state space with $\boldsymbol{k}$ is spanned by

$$|\varphi^s_{\boldsymbol{k}}\rangle = \frac{1}{\sqrt{V_G}} \sum_{(l,m,n)\in\mathbb{Z}^3} \exp(\mathrm{i}\boldsymbol{k}\cdot\boldsymbol{x}_{lmn})|\pi^s_{(l,m,n)}\rangle, \tag{2.13}$$

with $s \in \{1, 2, \cdots, S_{\mathrm{node}}\}$, where S_{node} is the number of nodes except for grounds in a unit. Solving the equation $\det[\hat{Y}_{\boldsymbol{k}}(\omega)] = 0$, we obtain the dispersion relation. The eigenvectors of $\hat{Y}_{\boldsymbol{k}}(\omega)$ with zero eigenvalue represent the potential distributions of the resonant modes.

2.4 Quantum tight-binding model analogy for electrical circuits

In this section, we present two examples of inductor–capacitor networks. These models are extensions of realistic systems experimentally investigated [93, 94]. For these models, we formulate the resonance condition and show the analogy between electrical circuits and quantum tight-binding models in solid-state physics.

2.4.1 Resonant circuits with mutual inductances

We consider resonant circuits, each composed of an inductance L_i and a capacitance C forming a mesh α_i, as shown in Fig. 2.2(a). For simplicity, we assume that all capacitors have the same capacitance C. The currents along α_i and α_j interact by a mutual inductance $M_{ij} = M_{ji}$. Owing to the coupling, electromagnetic excitations can propagate. This corresponds to magnetoinductive (MI) waves in metamaterials [95, 96] which have been experimentally confirmed [93].

For this circuit network, $\hat{Z}(\omega)$ is expressed as

$$\hat{Z}(\omega) = \sum_i \left(\mathrm{j}\omega L_i + \frac{1}{\mathrm{j}\omega C} \right) |\alpha_i\rangle\langle\alpha_i| + \mathrm{j}\omega \sum_{i \neq j} M_{ij} |\alpha_i\rangle\langle\alpha_j|. \tag{2.14}$$

We rewrite the equation $\mathrm{j}\omega C\hat{Z}(\omega)|\Psi\rangle = 0$ as follows:

$$\hat{K}|\Psi\rangle = \left(\frac{\omega_0}{\omega}\right)^2 |\Psi\rangle, \tag{2.15}$$

$$\hat{K} = \sum_i \xi_i |\alpha_i\rangle\langle\alpha_i| - \sum_{i \neq j} \kappa_{ij} |\alpha_i\rangle\langle\alpha_j|, \tag{2.16}$$

with $\omega_0 = 1/\sqrt{LC}$, $\xi_i = L_i/L$, and $\kappa_{ij} = -M_{ij}/L$, where L is an inductance for nondimensionalization. Equation (2.15) corresponds to the eigenvalue problem $\hat{H}|\Psi\rangle = \hbar\omega|\Psi\rangle$ in quantum mechanics. Thus, $\hat{K}$ can be interpreted as a Hamiltonian; $\hat{K}^{(\mathrm{p})} = \sum_i \xi_i |\alpha_i\rangle\langle\alpha_i|$ corresponds to the potential terms and $\hat{K}^{(\mathrm{h})} = -\sum_{\substack{i,j \\ i \neq j}} \kappa_{ij} |\alpha_i\rangle\langle\alpha_j|$ corresponds to the hopping terms. Thus, $\hat{K}$ corresponds to the Hamiltonian of the quantum tight-binding model. The difference between Eq. (2.15) and the quantum tight-binding model is how the eigenvalues of $\hat{H}$ and $\hat{K}$ depend on ω (or E).

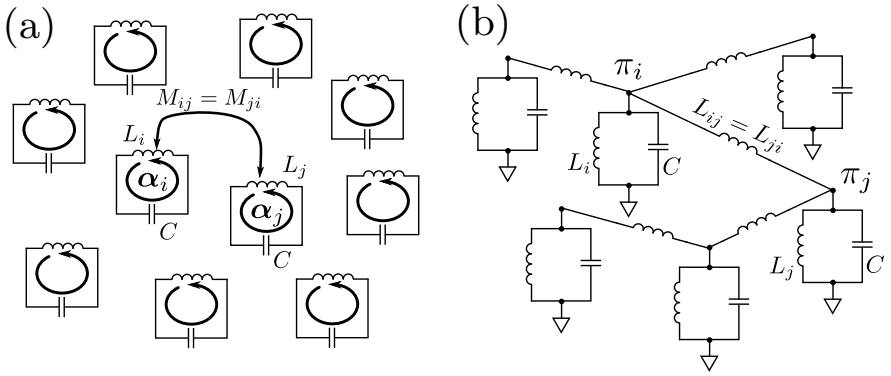

Figure 2.2: (a) Resonant circuits with mutual inductances. (b) Resonant circuits with coupling inductances - These circuits are analogous to the tight-binding models in quantum mechanics.

2.4.2 Resonant circuits with coupling inductances

We now consider resonant circuits, composed of an inductance L_i and a capacitance C connected in parallel to π_i, as shown in Fig. 2.2(b). All capacitors are assumed to have the same capacitance C. Each pair of resonant circuits is connected with a coupling

inductance $L_{ij} = L_{ji}$ between the nodes π_i and π_j. Such a circuit network has been studied to simulate the Scrödinger equation in classical systems [94, 97].

For this circuit network, $\hat{Y}(\omega)$ is expressed as

$$\hat{Y}(\omega) = \sum_i \left(\frac{1}{\mathrm{j}\omega L_i} + \mathrm{j}\omega C \right) |\pi_i\rangle\langle\pi_i| + \sum_{i \neq j} \frac{1}{\mathrm{j}\omega L_{ij}} \left(|\pi_i\rangle\langle\pi_i| - |\pi_i\rangle\langle\pi_j| \right).$$

Introducing an inductance L for nondimensionalization, the equation $\mathrm{j}\omega L\hat{Z}(\omega)|\Phi\rangle = 0$ is written as follows:

$$\hat{K}|\Phi\rangle = \left(\frac{\omega}{\omega_0} \right)^2 |\Phi\rangle, \tag{2.17}$$

$$\hat{K} = \sum_i \xi_i |\pi_i\rangle\langle\pi_i| - \sum_{i \neq j} \kappa_{ij} |\pi_i\rangle\langle\pi_j|, \tag{2.18}$$

where $\omega_0 = 1/\sqrt{LC}$, $\kappa_{ij} = L/L_{ij}$, and $\xi_i = L/L_i + \sum_{j \neq i} \kappa_{ij}$. Thus, $\hat{K}$ can be interpreted as a Hamiltonian with $\hat{K}^{(\mathrm{p})} = \sum_i \xi_i |\pi_i\rangle\langle\pi_i|$ and $\hat{K}^{(\mathrm{h})} = -\sum_{\substack{i,j \\ i \neq j}} \kappa_{ij} |\pi_i\rangle\langle\pi_j|$ representing potential and hoppings. Then, $\hat{K}$ corresponds to the Hamiltonian of the quantum tight-binding model. Unlike in Eq. (2.15), eigenvalues of $\hat{K}$ are dependent on ω quadratically. Then, we must discuss both cases in parallel. The quadratic frequency dependence is also different from that of the quantum tight-binding model.

2.5 1D propagation

In this section, we consider two examples of 1D periodic inductor–capacitor networks. By deriving the dispersion relation, we can obtain information on the propagation, such as the phase velocity and group velocity.

2.5.1 Resonant circuits with mutual inductances

In this subsection, we consider a 1D chain of circuits with mutual inductances shown in Fig. 2.3(a). The resonant elements are spaced by Δx. For simplicity, we assume $L_i = L$, and $M_{ij} = M = -\kappa L$ only for the nearest neighbors. The impedance operator of this circuit can be written as

$$\hat{Z}(\omega) = \left(\mathrm{j}\omega L + \frac{1}{\mathrm{j}\omega C} \right) \hat{1} + \mathrm{j}\omega M \sum_{i \in \mathbb{Z}} \Big(|\alpha_{i-1}\rangle\langle\alpha_i| + |\alpha_{i+1}\rangle\langle\alpha_i| \Big),$$

where $\hat{1}$ is the identity operator. We rewrite the 1D version of Eq. (2.10) as follows:

$$(1 - 2\kappa \cos k\Delta x)|\Psi_k\rangle = \left(\frac{\omega_0}{\omega}\right)^2 |\Psi_k\rangle. \tag{2.19}$$

From this equation, we obtain the dispersion relation as

$$\frac{\omega}{\omega_0} = \frac{1}{\sqrt{1 - 2\kappa \cos k\Delta x}}. \tag{2.20}$$

This dispersion relation is shown in Fig. 2.4(a) for $\kappa = -0.1$.

If $|k|\Delta x \ll 1$ (long-wavelength approximation) and $\kappa < 1/2$ are satisfied, Equation (2.20) is approximated as

$$\frac{\omega}{\omega_0} \sim \frac{1}{\sqrt{1 - 2\kappa}} \left[1 - \frac{\kappa}{2(1 - 2\kappa)}(k\Delta x)^2\right]. \tag{2.21}$$

Equation (2.21) is quadratic in k. The wave behaves like a massive particle. In particular, the group velocity $v_{\rm g} = {\rm d}\omega/{\rm d}k$ is zero at the Γ point (Γ means $k = 0$).

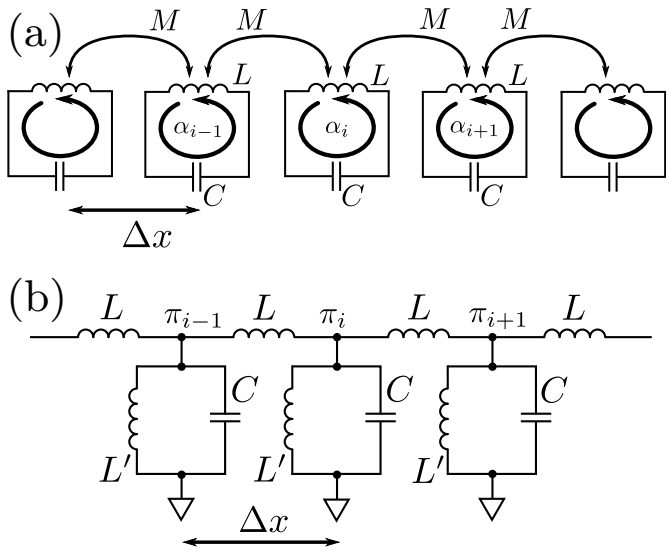

Figure 2.3: 1D resonant circuits - (a) Each resonant circuit has an inductance L, capacitance C, and mutual inductance M arranged at regular intervals of Δx. (b) Each resonant circuit has an inductance L', capacitance C, and coupling inductance L arranged at regular intervals of Δx

2.5.2 Resonant circuits with coupling inductances

In this subsection, we consider a 1D chain of circuits with coupling inductances, shown in Fig. 2.3 (b). For simplicity, we assume $L_i = L' = L/\mu^2$ and $L_{ij} = L$ for nearest

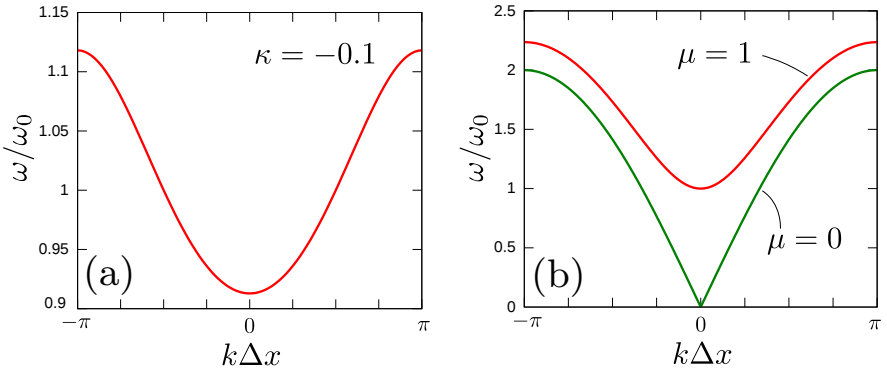

Figure 2.4: 1D dispersion relations - (a) 1D dispersion relation of resonant circuits with mutual inductances in the first Brillouin zone. The coupling constant is given by $\kappa = -0.1$. (b) 1D dispersion relation of resonant circuits with coupling inductances in the first Brillouin zone. The cases with $\mu = 1$ (massive) and $\mu = 0$ (massless) are shown.

neighbors. Here, a dimensionless parameter μ^2 is introduced to describe the ratio of L' and L.

The admittance operator of the circuit can be written as

$$\hat{Y}(\omega) = \left(\frac{1}{\mathrm{j}\omega L'} + \mathrm{j}\omega C\right)\hat{1} + \sum_i \frac{1}{\mathrm{j}\omega L}\Big(2|\pi_i\rangle\langle\pi_i| - |\pi_i\rangle\langle\pi_{i-1}| - |\pi_i\rangle\langle\pi_{i+1}|\Big).$$

We rewrite the 1D version of Eq. (2.12) as follows:

$$\left(\mu^2 + 4\sin^2\frac{k\Delta x}{2}\right)|\Phi_k\rangle = \left(\frac{\omega}{\omega_0}\right)^2|\Phi_k\rangle. \tag{2.22}$$

Solving Eq. (2.22), we obtain the dispersion relation as

$$\frac{\omega}{\omega_0} = \sqrt{\mu^2 + 4\sin^2\frac{k\Delta x}{2}}. \tag{2.23}$$

This dispersion is shown in Fig. 2.4(b) for $\mu = 0$ and 1.

Under the long-wavelength approximation $\sin(k\Delta x/2) \sim k\Delta x/2$, Eq. (2.23) is expressed as

$$\frac{\omega}{\omega_0} \sim \sqrt{\mu^2 + (k\Delta x)^2}. \tag{2.24}$$

This is similar to the dispersion relation of the Klein–Gordon wave equation describing a relativistic spinless free particle with energy $E = \sqrt{m^2c^4 + p^2c^2}$, where m and p are the particle's mass and momentum. Then, we can interpret $\mu\hbar\omega_0/c^2$ as the mass. Moreover, if $|k|\Delta x \ll \mu$ is satisfied, we have

$$\frac{\omega}{\omega_0} \sim \mu + \frac{1}{2\mu}(k\Delta x)^2, \tag{2.25}$$

i.e., the dispersion relation for the Schrödinger wave equation except for the constant term μ. This feature of dispersion is observed in Fig. 2.4(b) with $\mu = 1$ near the Γ point.

Another interesting case is $\mu \to 0$ with keeping the inductance L constant. In this case, L' becomes open ($L' \to \infty$) and the circuit behaves as a transmission line (an LC ladder). Then, the dispersion relation is expressed as

$$\frac{\omega}{\omega_0} = 2\left|\sin\frac{k\Delta x}{2}\right|. \tag{2.26}$$

In the long wavelength regime $|k|\Delta x \ll 1$, Eq. (2.26) is approximated as

$$\frac{\omega}{\omega_0} \sim |k|\Delta x. \tag{2.27}$$

This is a linear dispersion and we obtain massless (plasmonic) propagation. Our picture is valid for this system, which does not have tightly bound eigenmodes. For this dispersion, the group velocity v_g is not zero near the Γ point. This characteristic of dispersion is observed in Fig. 2.4(b) with $\mu = 0$ near the Γ point. This is critically different from the case $\mu > 0$. By using a massless propagation mode, efficient energy transfer can be realized [98, 99].

2.6 Design of a heavy photon

In a solid state lattice with specific symmetries, a flat electron dispersion relation independent of the wave vector is formed and is called *a flat band*. In the flat band, the group velocity of an electron is slowed down for all wave vectors, and the mass becomes very heavy. Therefore, the electron correlation energy exceeds the kinetic energies and ferromagnetism can occur in the system. It is known that Lieb-type [100], Tasaki-type [101], and Mielke-type [102] symmetries cause flat bands and ferromagnetism for electron systems.

The presence of flat bands has already been predicted for some electromagnetic systems, such as two-dimensional photonic crystals [103, 104] and metallophotonic waveguide networks [85, 105].

In this section, we consider the analogy for the heavy electron in an electromagnetic system, namely, *a heavy photon* (strictly speaking, *a heavy plasmon polariton*) in metamaterials. For this purpose, we use the 2D inductor–capacitor circuit networks treated

in Sec. 2.4. The models can be expressed by the Hamiltonian $\hat{K}$ of Eq. (2.16) and Eq. (2.18). We introduce three types of inductor–capacitor circuit networks with Lieb-, Tasaki-, and Mielke-type symmetries, where the formation of flat bands is expected.

2.6.1 Lieb type

We consider a periodic graph with two groups of nodes, A and B. The nodes in A are only connected to ones in B, and vice versa. Such a graph is called *bipartite*. We denote the number of A or B nodes in a unit cell as $|A|$ or $|B|$, and assume $|A| > |B|$ and introduce constant potentials $\xi_i = \xi$. By using the plane-wave basis Eq. (2.8) or Eq. (2.13), the hopping Hamiltonian $\hat{K}^{(\mathrm{h})}_{\boldsymbol{k}}$ can be written as

$$\hat{K}^{(\mathrm{h})}_{\boldsymbol{k}} \doteq \left[\begin{array}{c|c} 0 & K_{AB}(\boldsymbol{k}) \\ \hline K_{BA}(\boldsymbol{k}) & 0 \end{array}\right], \tag{2.28}$$

where "$\doteq$" indicates matrix representation. Here, $\operatorname{rank} K_{AB} < |B|$ is satisfied and then $\operatorname{rank} \hat{K}^{(\mathrm{h})}_{\boldsymbol{k}} < 2|B|$. Therefore, $\dim\ker \hat{K}^{(\mathrm{h})}_{\boldsymbol{k}} > |A| - |B|$ and there exist at least $|A| - |B|$ zero eigenvalues of $\hat{K}^{(\mathrm{h})}_{\boldsymbol{k}}$. Then, the flat band is formed [100]. Next, we consider the eigenvectors of the flat band. Because $\operatorname{rank} K_{BA} < |B|$ leads to $\dim\ker K_{BA} > |A| - |B|$, there exist at least $|A| - |B|$ eigenvectors with a zero eigenvalue of $\hat{K}^{(\mathrm{h})}_{\boldsymbol{k}}$. These eigenvectors have zero amplitudes in B. Thus, we can say that the flat band is composed of eigenvectors having non-zero amplitudes only in A.

For a concrete example, we consider a 2D periodic bipartite graph G_1 shown in Fig. 2.5(a). We assume hopping along edges with $\kappa_{ij} = \kappa$ for simplicity. Then, $\hat{K}^{(\mathrm{h})}_{\boldsymbol{k}}$ is represented as

$$\hat{K}^{(\mathrm{h})}_{\boldsymbol{k}} \doteq -\kappa \begin{bmatrix} 0 & 0 & 1 + \mathrm{e}^{\mathrm{i}\boldsymbol{k}\cdot\boldsymbol{a}_1} \\ 0 & 0 & 1 + \mathrm{e}^{\mathrm{i}\boldsymbol{k}\cdot\boldsymbol{a}_2} \\ 1 + \mathrm{e}^{-\mathrm{i}\boldsymbol{k}\cdot\boldsymbol{a}_1} & 1 + \mathrm{e}^{-\mathrm{i}\boldsymbol{k}\cdot\boldsymbol{a}_2} & 0 \end{bmatrix}. \tag{2.29}$$

Solving the characteristic equation $\det(\hat{K}^{(\mathrm{h})}_{\boldsymbol{k}} - \chi_{\boldsymbol{k}}\hat{1}) = 0$, we obtain the eigenvalue $\chi_{\boldsymbol{k}}$ of $\hat{K}^{(\mathrm{h})}_{\boldsymbol{k}}$ as follows:

$$\chi_{\boldsymbol{k}} = 0, \quad \pm 2\kappa\sqrt{\cos^2\frac{\boldsymbol{k}\cdot\boldsymbol{a}_1}{2} + \cos^2\frac{\boldsymbol{k}\cdot\boldsymbol{a}_2}{2}}. \tag{2.30}$$

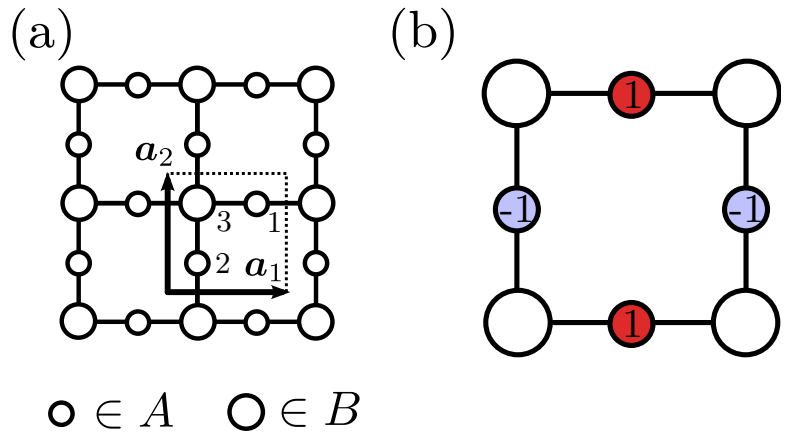

Figure 2.5: (a) Example of Lieb-type lattice G_1 (b) Localized eigenmode - Lattice vectors are denoted as $\boldsymbol{a}_1$ and $\boldsymbol{a}_2$ and the resonator numbers in a unit cell are indicated beside the corresponding circle for (a). The amplitudes of the mode are expressed in the circles for (b).

Here, $\chi_{\boldsymbol{k}}$ is identical to the eigenenergy of the quantum tight-binding model. $\chi_{\boldsymbol{k}} = 0$ corresponds to a flat band, which is composed of the localized eigenmodes shown in Fig. 2.5(b). For this eigenmode, we can observe the destructive interference in hopping. This mode, having zero amplitude in B, is constructed by excess degrees of freedom in A.

We can then determine the band structure of the two types of circuit networks. For resonant circuits with mutual inductances, we obtain the dispersion relation as

$$\frac{\omega}{\omega_0} = \frac{1}{\sqrt{\xi + \chi_{\boldsymbol{k}}}}. \tag{2.31}$$

By using Eq. (2.30) and Eq. (2.31), the band structures of resonant circuits with mutual inductances are calculated and shown in Fig. 2.6(a) for $\kappa = -0.2$ and $\xi = 1$. We find that the second band is flat. If $|\chi_{\boldsymbol{k}}| \ll |\xi|$ is satisfied, Eq. (2.31) is approximated as

$$\frac{\omega}{\omega_0} \sim \frac{1}{\sqrt{\xi}} \left(1 - \frac{\chi_{\boldsymbol{k}}}{2\xi}\right). \tag{2.32}$$

This dispersion relation has the same shape as that of the quantum tight-binding model.

For resonant circuits with coupling inductances, we obtain the dispersion relation as

$$\frac{\omega}{\omega_0} = \sqrt{\xi + \chi_{\boldsymbol{k}}}. \tag{2.33}$$

By using Eq. (2.30) and Eq. (2.33), the band structures of resonant circuits with coupling inductances are calculated and shown in Fig. 2.6(b) for $\kappa = 1$ and $\xi = 5$. We can

see that the second band is flat. If $|\chi_{\boldsymbol{k}}| \ll |\xi|$ is satisfied, Eq. (2.33) is approximated as

$$\frac{\omega}{\omega_0} \sim \sqrt{\xi}\left(1 + \frac{\chi_{\boldsymbol{k}}}{2\xi}\right). \tag{2.34}$$

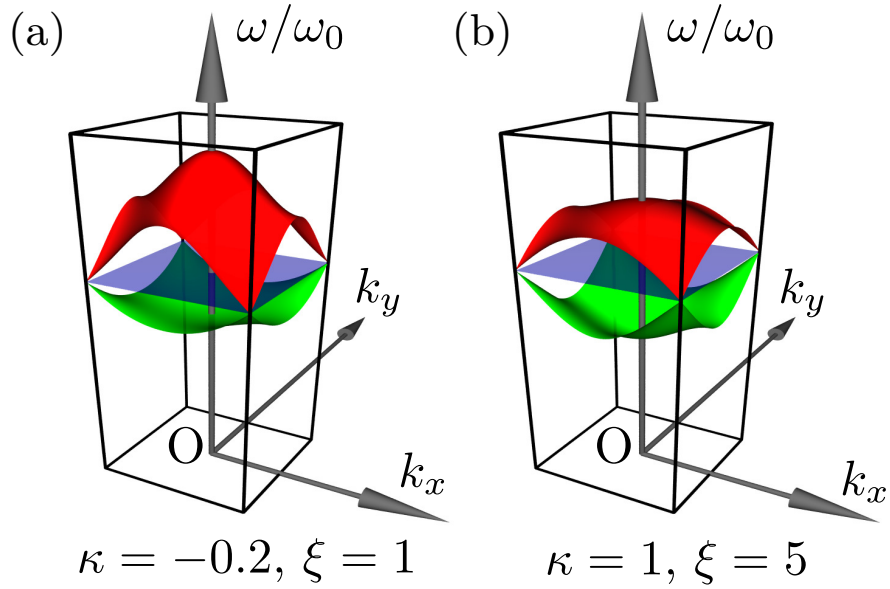

Figure 2.6: Dispersion relations of Lieb lattices - (a) Dispersion relation of resonant circuits with mutual inductances connected to form G_1 for $\kappa = -0.2$ and $\xi = 1$ in the first Brillouin zone. (b) Dispersion relation of resonant circuits with coupling inductances connected to form G_1 for $\kappa = 1$ and $\xi = 5$ in the first Brillouin zone.

2.6.2 Tasaki type

A construction of flat bands by Tasaki [101] starts with a three-site system with the basis $\{|u\rangle, |v\rangle, |w\rangle\}$ and the Hamiltonian

$$\hat{K} = -\kappa(|u\rangle + \lambda|v\rangle + |w\rangle)(\langle u| + \lambda\langle v| + \langle w|), \tag{2.35}$$

where $\lambda \in \mathbb{R}, \lambda \neq 0$. The Hamiltonian $\hat{K}$ has a zero eigenvalue with eigenvectors $[0, -1/\lambda, 1]^{\mathrm{T}}$, $[1, -1/\lambda, 0]^{\mathrm{T}}$ [Fig. 2.7(a)]. For the construction of a flat band, we first prepare two $[0, -1/\lambda, 1]^{\mathrm{T}}$ and bond them at the site with amplitude 1 to make an array of five sites [Fig. 2.7(b)]. Secondly, we prepare two five-site arrays, rotate one by 90° and connect them at the center site [Fig. 2.7(c)]. Finally, we align it periodically [Fig. 2.7(d)]. This procedure ensures that $\hat{K}$ has localized eigenmodes and we can obtain a flat band.

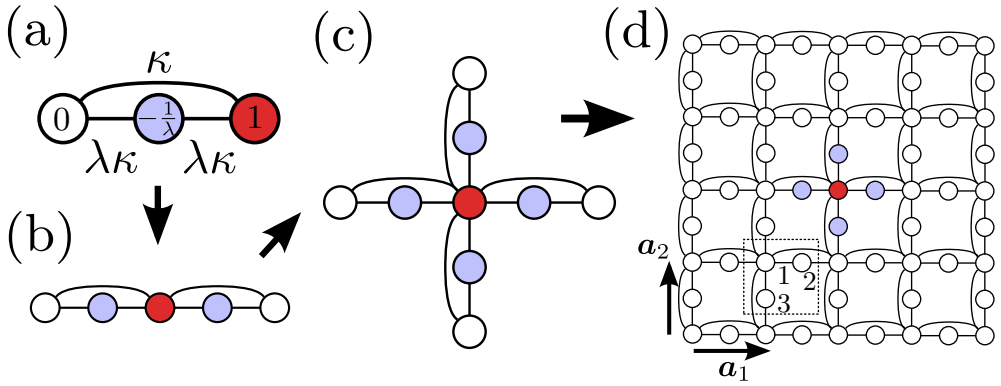

Figure 2.7: Construction of the Tasaki-type flat band - Hopping probability amplitudes are shown near the edges and the amplitudes of modes are expressed in circles. Lattice vectors are denoted as $\boldsymbol{a}_1$ and $\boldsymbol{a}_2$ and the resonator numbers in a unit cell are indicated beside the corresponding circle

For a concrete example, we calculate the band structure for the graph G_2 shown in Fig. 2.7(d). The diagonal terms of $\hat{K}$ are -4κ, $-\lambda^2\kappa$, and $-\lambda^2\kappa$ with respect to resonators 1, 2, and 3 [these are depicted in Fig. 2.7(d)]. They should be positive in circuit networks. Therefore, we add a constant potential ξ and obtain $\hat{K}_{\boldsymbol{k}}$ as

$$\hat{K}_{\boldsymbol{k}} \doteq -\kappa A + \xi I, \tag{2.36}$$

$$A = \begin{bmatrix} 2(2+\cos\boldsymbol{k}\cdot\boldsymbol{a}_1+\cos\boldsymbol{k}\cdot\boldsymbol{a}_2) & \lambda(1+\mathrm{e}^{-\mathrm{i}\boldsymbol{k}\cdot\boldsymbol{a}_1}) & \lambda(1+\mathrm{e}^{\mathrm{i}\boldsymbol{k}\cdot\boldsymbol{a}_2}) \\ \lambda(1+\mathrm{e}^{\mathrm{i}\boldsymbol{k}\cdot\boldsymbol{a}_1}) & \lambda^2 & 0 \\ \lambda(1+\mathrm{e}^{-\mathrm{i}\boldsymbol{k}\cdot\boldsymbol{a}_2}) & 0 & \lambda^2 \end{bmatrix}, \tag{2.37}$$

where I is the identity matrix. By calculating the eigenvalues $\chi_{\boldsymbol{k}}$ of $-\kappa A$, we obtain

$$\chi_{\boldsymbol{k}} = 0,\ -\kappa\lambda^2,\ -\kappa\left(\lambda^2 + 4\cos^2\frac{\boldsymbol{k}\cdot\boldsymbol{a}_1}{2} + 4\cos^2\frac{\boldsymbol{k}\cdot\boldsymbol{a}_2}{2}\right). \tag{2.38}$$

The flat band with $\chi_{\boldsymbol{k}} = 0$ is created by the Tasaki-type localized eigenmodes, and the band with $\chi_{\boldsymbol{k}} = -\kappa\lambda^2$ is formed by the Lieb-type localized eigenmodes [Fig. 2.5(b)] because G_2 includes G_1.

Using Eq. (2.31) and Eq. (2.38), the band structure of resonant circuits with mutual inductances is shown in Fig. 2.8(a) for $\lambda = 2$, $\kappa = -0.2$, and $\xi = 1$. The bands with the second and third highest frequencies are flat. The second is the Lieb-type flat band, and the third is the Tasaki-type flat band.

Using Eq. (2.33) and Eq. (2.38), the band structure of resonant circuits with coupling inductances is calculated and shown in Fig. 2.8(b) for $\lambda = 2$, $\kappa = 1$, and $\xi = 15$.

The bands with the second and third highest frequencies are flat. If ξ is very large, these dispersions have the same shape as that of the quantum tight-binding model.

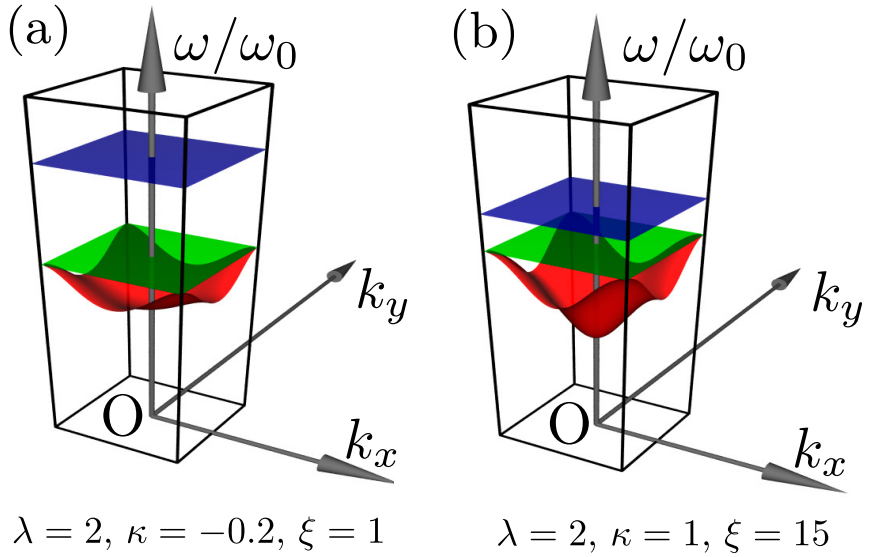

Figure 2.8: Dispersion relations of Tasaki lattices - (a) Dispersion relation of resonant circuits with mutual inductances connected to form G_2 for $\lambda = 2$, $\kappa = -0.2$, and $\xi = 1$ in the first Brillouin zone. (b) Dispersion relation of resonant circuits with coupling inductances connected to form G_2 for $\lambda = 2$, $\kappa = 1$, and $\xi = 15$ in the first Brillouin zone.

2.6.3 Mielke type

The Mielke-type construction uses the notion of graph theory [102]. We first introduce a *simple* graph $G = (V, E)$, where V and E are the sets of vertices and edges that connect the vertices. The modifier "simple" means that there are no multiple edges between any vertex pair and no edge that connects a vertex (loop). We can express how to connect edges between vertices by using the adjacency matrix $A = [A_{ij}]$, where A_{ij} (0 or 1) is the number of edges between vertices v_i and v_j. We can also use the incidence matrix X, where X_{il} is 1 if the edge e_l is connected to the node v_i, and otherwise is zero. The line graph $L(G) = (V_L, E_L)$ of G is constructed as follows. Each edge in G is considered to be the vertex of $L(G)$. Two vertices of $L(G)$ are connected if the corresponding edges in G have a vertex in common. The adjacency matrix A_L of $L(G)$ is represented as

$$A_L = X^{\mathrm{T}} X - 2I \tag{2.39}$$

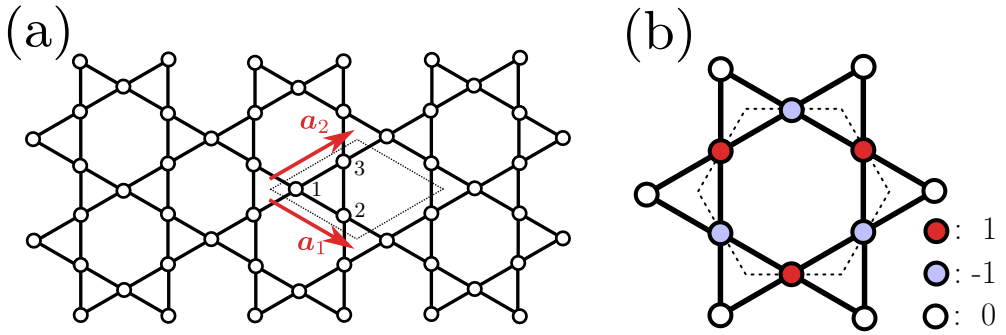

Figure 2.9: Kagomé lattice - (a) Mielke-type kagomé lattice $L(G_3)$. Lattice vectors are denoted as $\boldsymbol{a}_1$ and $\boldsymbol{a}_2$, and the resonator numbers in a unit cell are indicated beside the corresponding circle. (b) Localized eigenmode. The amplitudes of the modes are expressed by the color of the circles. The dotted line presents G_3.

by using X and the identity matrix I. This follows from $\sum_j X_{jk}X_{jl} = 2$ for $k = l$, and $\sum_j X_{jk}X_{jl} = (A_L)_{kl}$ for $k \neq l$.

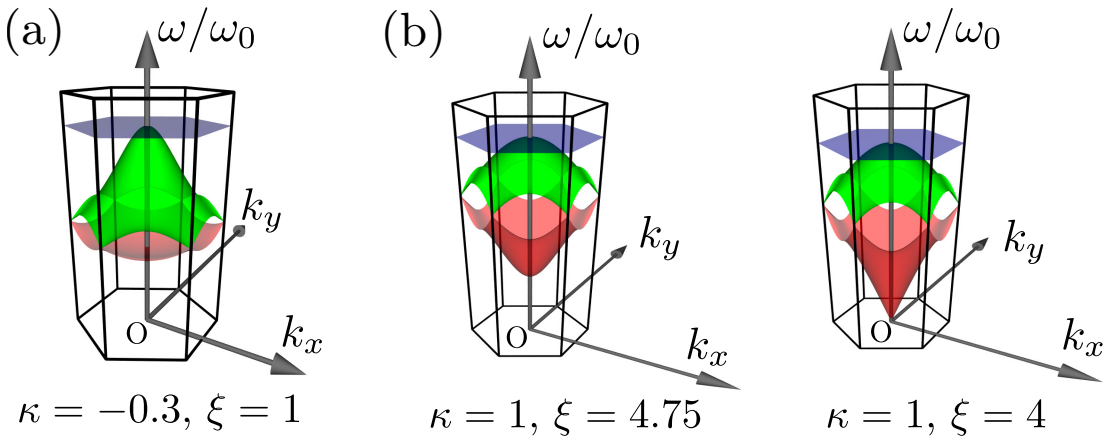

Figure 2.10: Dispersion of kagomé lattices - (a) Dispersion relation of resonant circuits with mutual inductances connected to form $L(G_3)$ for $\kappa = -0.3$ and $\xi = 1$ in the first Brillouin zone. (b) Dispersion relation of resonant circuits with coupling inductances connected to form $L(G_3)$ in the first Brillouin zone. The left graph is for $\kappa = 1$ and $\xi = 4.75$ (massive). The right graph is for $\kappa = 1$ and $\xi = 4$ (massless).

Next, we consider the hopping Hamiltonian $\hat{K}^{(\mathrm{h})} \doteq -\kappa A_L$ and its eigenvalue problem. To solve this problem, we introduce a closed walk. In a graph $G = (V, E)$, a walk is a sequence $(v_1, e_1, v_2, e_2, \cdots, e_{n-1}, v_n)$ where $v_i \in V$, $e_i = \{v_i, v_{i+1}\} \in E$ for $1 \leq i \leq n-1$ and n is the length of the walk. A walk satisfying $v_1 = v_n$ is called a closed walk. Given a closed walk $c = (v_1, e_1, v_2, e_2, \cdots, e_{n-1}, v_1)$ in G, we can construct a vector $v(c) = \sum(-1)^i e_i$. From Eq. (2.39), $v(c)$ is the eigenvector of $\hat{K}^{(\mathrm{h})}$ with the

eigenvalue 2κ for even n. Therefore, if the periodic graph G has at least one closed walk with even length, we can obtain the flat band.

As a concrete example, we calculate the band structure for a kagomé lattice, which is the line graph $L(G_3)$ of a hexagonal lattice G_3, shown in Fig. 2.9(a). $\hat{K}_{\boldsymbol{k}}^{(\mathrm{h})}$ is represented as

$$\hat{K}_{\boldsymbol{k}}^{(\mathrm{h})} \doteq -\kappa \begin{bmatrix} 0 & 1+\mathrm{e}^{-\mathrm{i}\boldsymbol{k}\cdot\boldsymbol{a}_1} & 1+\mathrm{e}^{-\mathrm{i}\boldsymbol{k}\cdot\boldsymbol{a}_2} \\ 1+\mathrm{e}^{\mathrm{i}\boldsymbol{k}\cdot\boldsymbol{a}_1} & 0 & 1+\mathrm{e}^{\mathrm{i}\boldsymbol{k}\cdot(\boldsymbol{a}_1-\boldsymbol{a}_2)} \\ 1+\mathrm{e}^{\mathrm{i}\boldsymbol{k}\cdot\boldsymbol{a}_2} & 1+\mathrm{e}^{-\mathrm{i}\boldsymbol{k}\cdot(\boldsymbol{a}_1-\boldsymbol{a}_2)} & 0 \end{bmatrix}. \tag{2.40}$$

The eigenvalues $\chi_{\boldsymbol{k}}$ of $\hat{K}_{\boldsymbol{k}}^{(\mathrm{h})}$ are

$$\chi_{\boldsymbol{k}} = 2\kappa,\ -\kappa\left[1 \pm \sqrt{3+2F(\boldsymbol{k})}\right], \tag{2.41}$$

where,

$$F(\boldsymbol{k}) = \cos\boldsymbol{k}\cdot\boldsymbol{a}_1 + \cos\boldsymbol{k}\cdot\boldsymbol{a}_2 + \cos\boldsymbol{k}\cdot(\boldsymbol{a}_1-\boldsymbol{a}_2). \tag{2.42}$$

The eigenvalue 2κ of $\chi_{\boldsymbol{k}}$ corresponds to a flat band. The flat band is composed of the localized modes shown in Fig. 2.9(b), where the corresponding closed walk of G_3 is depicted by the dotted line.

Then, we can determine the band structure of the two types of circuit networks with the symmetry of the kagomé lattice. For resonant circuits with mutual inductances, the band structure is shown in Fig. 2.10(a) by using Eq. (2.31) and Eq. (2.41) for $\kappa = -0.3$ and $\xi = 1$. The band with the third highest frequency is flat. For resonant circuits with coupling inductances, we also use Eq. (2.33) and Eq. (2.41), and the band structure can be calculated. The left graph of Fig. 2.10(b) is for $\kappa = 1$ and $\xi = 4.75$, while the right graph is for $\kappa = 1$ and $\xi = 4$. We can observe the massless (plasmonic) dispersion for $\kappa = 1$ and $\xi = 4$. This corresponds to the massless limit ($L_i \to \infty$). For both the massive and massless cases, we can realize flat bands. If ξ is very large, these dispersions have the same shape as that of the quantum tight-binding models.

As a result, we realized Lieb-, Tasaki-, and Mielke-type flat bands in inductor–capacitor circuit networks. This indicates that these three types of flat bands can be realized in metamaterials.

2.7 Summary

In this chapter, we investigated circuit-theoretical analysis method for hybridization modes in metamaterials. For this purpose, we employed circuit models of metama-

terials. We formulated two general methods to calculate the hybridization modes in arbitrary inductor–capacitor circuit networks: the mesh current method and node potential method. In the first method, mesh currents are taken as the basic variables, and we calculate the voltage drops along all meshes and apply the KVL. In the second method, the node potentials are used as the basic variables, and we calculate the divergences of currents at all nodes except for grounds and apply the KCL. We utilized the bra-ket notation and formulated them as eigenvalue problems. Therefore, we can perform calculations using the familiar methods of quantum mechanics. A periodic inductor–capacitor circuit network was also considered. We used plane waves as basis functions and formulated a method to calculate the dispersion relation.

Next, we analyzed two types of circuit networks: resonant circuits with mutual inductances and resonant circuits with coupling inductances. Applying our theory to these circuits, we determined the quantum-mechanical analogy for these circuits. This analogy will enable us to realize metamaterials with similar dispersion relations in quantum tight-binding models. To study the basics of these circuit networks, 1D propagation was analyzed. We then revealed that massive and massless propagation can be seen in these circuit networks.

Finally, by using the quantum-mechanical analogy for inductor–capacitor circuit networks, we predicted heavy photons in metamaterials. We analyzed three types of lattice symmetry: the Lieb-, Tasaki-, and Mielke-type lattices. Then, we showed that flat bands can be formed in metamaterials with all these symmetries. The flatness of the bands can be applied to frequency filters independent of incident angle. Slowing down the group velocity of a photon can also lead to increased interactions with matter.

These results show the predictive power of our theoretical frameworks. Moreover, other band structures in quantum tight-binding models can be realized in inductor–capacitor circuit networks.

Chapter 3

Observation of flat band

3.1 Background

In Chap. 2, we theoretically revealed that flat bands are formed in circuits with Lieb, Tasaki, and Mielke-type lattices. In this chapter, we experimentally demonstrate the flat band formation for a metallic kagomé lattice. Kagomé lattices have attracted considerable interest from the aspect of geometric frustration in condensed-matter physics [106].

At first, we seek a simple system to implement the kagomé lattice. In 2006, Liu *et al.* theoretically analyzed the array of single split ring resonators (SSRRs) in the optical regime. A SSRR is depicted in Fig. 3.1(a). This resonator acts as a simple LC resonator modeled in the bottom of Fig. 3.1(a). When SSRRs are connected as shown in Fig. 3.1(b), we obtain the array which can be modeled as a LC ladder. The LC ladder leads to efficient energy transport as we have shown in Sec. 2.5.2. $\hat{Z}(\omega)$ of the ladder is written as

$$\hat{Z}(\omega) = \sum_i \Bigg\{ \mathrm{j}\omega L|\alpha_i\rangle\langle\alpha_i| + \frac{1}{\mathrm{j}\omega C}|\alpha_i\rangle\Big[\langle\alpha_i| - \langle\alpha_{i+1}|\Big] + \frac{1}{\mathrm{j}\omega C}|\alpha_i\rangle\Big[\langle\alpha_i| - \langle\alpha_{i-1}|\Big] + \mathrm{j}\omega M|\alpha_i\rangle\Big[\langle\alpha_{i-1}| + \langle\alpha_{i+1}|\Big]\Bigg\}, \quad (3.1)$$

where α_i is each loop, L is the inductance of a loop, and C is the capacitance between two adjacent loops. Mutual inductance between adjacent loops are denoted by M, where we consider only the nearest mutual couplings. Note that we assume the current distribution in a ring is represented by a loop current and variation of the current distribution in a ring is ignored in this model.

Now, we introduce adjacency matrix A_{ij}, where A_{ij} is 1 for $j = i + 1$ or $j = i - 1$, otherwise 0. $\hat{Z}(\omega)$ is simply expressed as

$$\hat{Z}(\omega) = \sum_i \left\{ \mathrm{j}\omega L|\alpha_i\rangle\langle\alpha_i| + \frac{1}{\mathrm{j}\omega C}\sum_j A_{ij}|\alpha_i\rangle\Big[\langle\alpha_i| - \langle\alpha_j|\Big] + \mathrm{j}\omega M \sum_j A_{ij}|\alpha_i\rangle\langle\alpha_j| \right\}. \quad (3.2)$$

For $M = 0$, we obtain the same dispersion as shown in Fig. 2.4(b) with $\mu = 0$.

For the experimental confirmation of the band, Liu *et al.* proposed slit-hole resonators (SHRs) composed of slits and holes engraved on a thin metallic plate [99]. They fabricated the SHRs with equal-length slits and different-sized holes shown in Fig. 3.2(a).

These SHRs have the band upper the light line ($\omega = c_0 k$) like optical phonons, while the dispersion curve of SSRRs is under the light line. Here, c_0 is the speed of light. Then, plane waves can couple the eigenmodes of SHRs. They experimentally demonstrated that the excitation of eigenmodes leads to extraordinary transmission. Zhu *et al.* also demonstrated EOT for SHRs with different-length slits and equal-sized holes shown in Fig. 3.2(b) [107].

3.2 Kagomé-type bar-disk resonators

We consider SHRs with the kagomé symmetry shown in Fig. 3.3. This structure is called "kagomé-type slit-hole resonators" (KSHRs). KSHRs can be described by $Z(\omega)$ of Eq. (3.2) with the adjacency matrix A_{ij} of the kagomé lattice. Then, the flat band is formed as described in Chap. 2 if we ignore mutual inductances. However, this structure is not free-standing, so it is impossible to fabricate without a substrate. In order to resolve this problem, we exchange hole with metals, and obtain kagomé-type bar-disk resonators (KBDRs). The KBDRs and KSHRs are complementary structures related through the Babinet's principle, and respond similarly (See Chap. 4 for details of the Babinet's principle).

For Eq. (3.2), we replace each parameters as Table 3.1 to modelize KBDRs. Now,

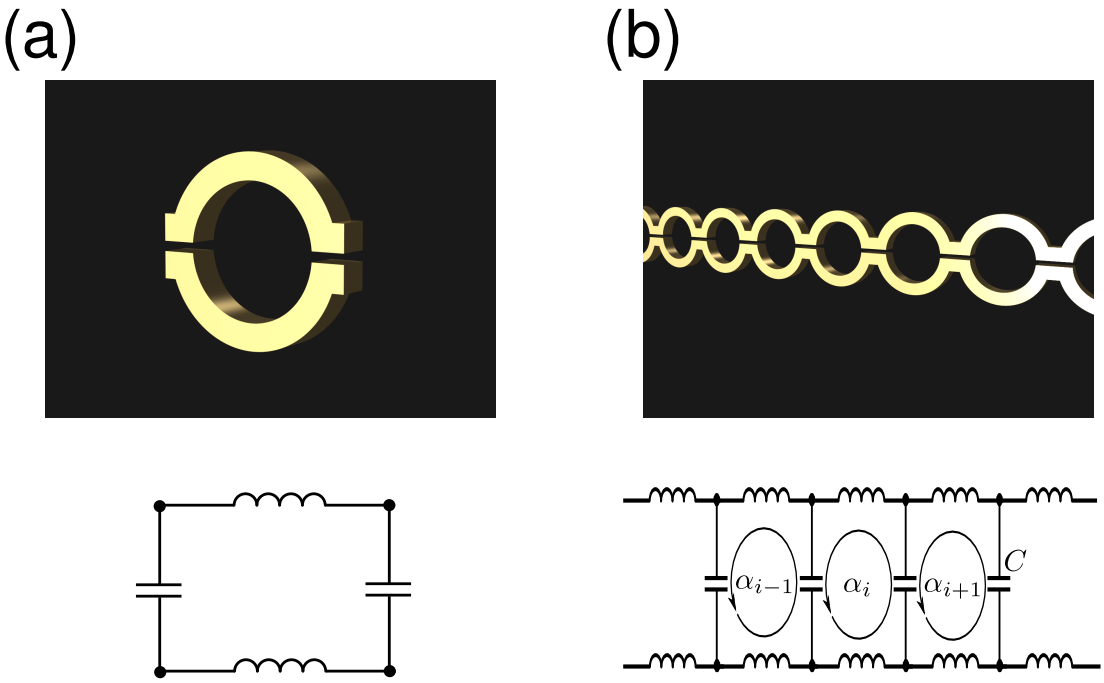

Figure 3.1: Single split-ring resonators (SSRRs) - (a) Unit SSRR. (b) Array of SSRRs. Circuit models are also shown in the bottom.

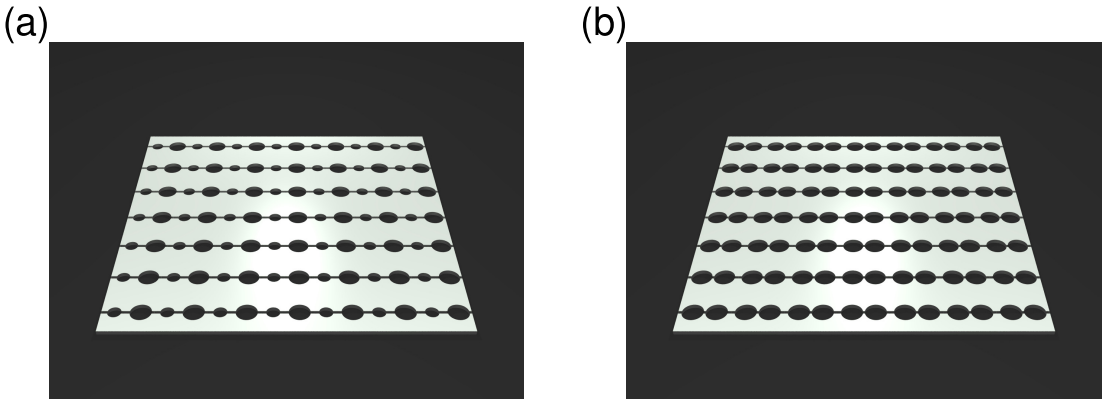

Figure 3.2: Slit-hole resonators - (a) Equal-length slits and different-sized holes. (b) Different-length slits and equal-sized holes.

Slit-hole resonator	Bar-disk resonator
magnetic flux	electric charge
loop α_i	node P_i
loop current $\tilde{J}_i$	node potential $\tilde{\phi}_i$
impedance $\hat{Z}(\omega)$	admittance $\hat{Y}'(\omega)$
inductance L	capacitance C'
mutual inductance M	mutual capacitance C'_{M}
transmission coefficient	reflection coefficient

Table 3.1: Dual entities - slit-hole resonator and bar-disk resonator

we obtain

$$\begin{aligned}\hat{Y}'(\omega) &= \sum_i \left\{ \mathrm{j}\omega C' |\mathrm{P}_i\rangle\langle \mathrm{P}_i| + \frac{1}{\mathrm{j}\omega L'} \sum_j A_{ij} |\mathrm{P}_i\rangle \Big[\langle \mathrm{P}_i| - \langle \mathrm{P}_j| \Big] + \mathrm{j}\omega C'_{\mathrm{M}} \sum_j A_{ij} |\mathrm{P}_i\rangle\langle \mathrm{P}_j| \right\} \\ &= \left(\mathrm{j}\omega C' + \frac{4}{\mathrm{j}\omega L'} \right) \hat{1} + \left(\mathrm{j}\omega C'_{\mathrm{M}} - \frac{1}{\mathrm{j}\omega L'} \right) \sum_{i,j} A_{ij} |\mathrm{P}_i\rangle\langle \mathrm{P}_j|, \end{aligned} \tag{3.3}$$

with the identity operator $\hat{1}$.

Then, eigenmode $|\Phi\rangle$ satisfies

$$\hat{A}|\Phi\rangle = \frac{4 - (\omega/\omega_0)^2}{1 + \kappa\,(\omega/\omega_0)^2} |\Phi\rangle, \tag{3.4}$$

where $\hat{A} = \sum_i \sum_j A_{ij} |\mathrm{P}_i\rangle\langle \mathrm{P}_j|$, $\omega_0 = 1/\sqrt{L'C'}$, and $\kappa = C'_{\mathrm{M}}/C$.

We set y axis parallel to a bar of KBDRs as shown in Fig. 3.5(a). Owing to the lattice symmetry, we can reduce Eq. (3.4) to an eigenvalue problem for a 3×3 matrix and obtain the dispersion relation consisting of three bands as

$$\frac{\omega}{\omega_0} = \sqrt{\frac{6}{1-2\kappa}},\ \sqrt{\frac{3 + 2(3+F)\kappa \pm (1+4\kappa)\sqrt{3+2F}}{1 + 2\kappa - 2(1+F)\kappa^2}}, \tag{3.5}$$

where $F(\boldsymbol{k}_\parallel) = \cos \boldsymbol{k}_\parallel \cdot \boldsymbol{a}_1 + \cos \boldsymbol{k}_\parallel \cdot \boldsymbol{a}_2 + \cos \boldsymbol{k}_\parallel \cdot (\boldsymbol{a}_1 - \boldsymbol{a}_2)$ with wavevector $\boldsymbol{k}_\parallel$ in the xy plane and unit-lattice vectors $\{\boldsymbol{a}_1,\ \boldsymbol{a}_2\}$ are shown in Fig. 3.5(a). The highest band $\omega/\omega_0 = \sqrt{6/(1-2\kappa)}$ is flat or independent of $\boldsymbol{k}_\parallel$ for $C'_{\mathrm{M}} \neq 0$.

In particular, we focus on the case of $\boldsymbol{k}_\parallel = k_\parallel \boldsymbol{e}_x$. We define $\varphi = \boldsymbol{k}_\parallel \cdot \boldsymbol{a}_1 = \boldsymbol{k}_\parallel \cdot \boldsymbol{a}_2$. In this case, the eigenvector corresponding the flat band is

$$[0\ \ -1\ \ 1]^{\mathrm{T}}. \tag{3.6}$$

This mode can be constructed by the localized modes shown in Fig. 2.9(b). The eigenvector of second highest band is given by

$$\left[-\frac{1+\sqrt{3+2F(\boldsymbol{k}_{\parallel})}}{1+\mathrm{e}^{\mathrm{i}\varphi}} \quad 1 \quad 1 \right]^{\mathrm{T}}, \tag{3.7}$$

and that of lowest band is

$$\left[-\frac{1-\sqrt{3+2F(\boldsymbol{k}_{\parallel})}}{1+\mathrm{e}^{\mathrm{i}\varphi}} \quad 1 \quad 1 \right]^{\mathrm{T}}. \tag{3.8}$$

For $\varphi \sim 0$, Eq. (3.7) and (3.8) are reduced to $[-2\ 1\ 1]^{\mathrm{T}}$ and $[1\ 1\ 1]^{\mathrm{T}}$, respectively. These modes are shown in Fig. 3.4.

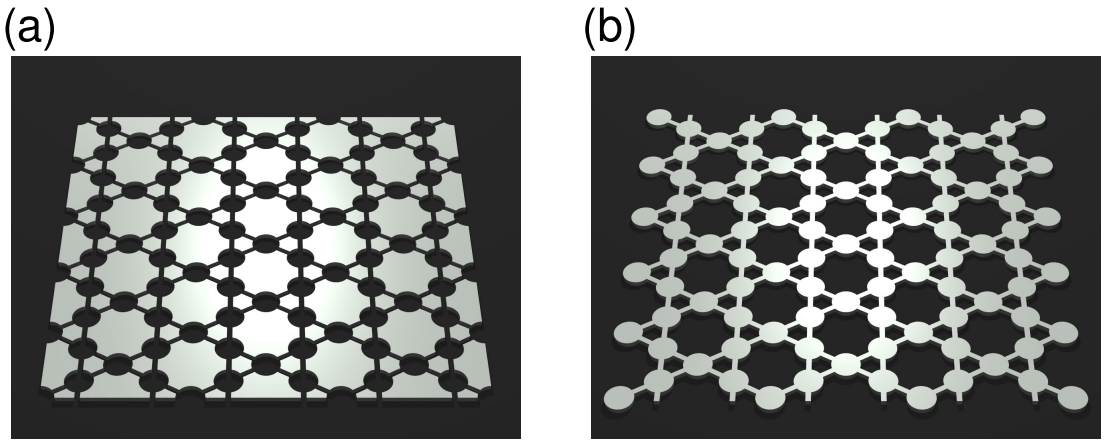

Figure 3.3: Resonators with the kagomé symmetry - (a) Slit-hole resonators. (b) Bar-disk resonators.

3.3 Experiments

3.3.1 Sample preparation

We fabricate KBDRs on a stainless-steel plate by etching. The dimensions depicted in Fig. 3.5(a) are as follows: period between bars $l = 800\,\mu$m, bar width $d = 10\,\mu$m, disk radius $r = 145\,\mu$m, and metal thickness $h = 30\,\mu$m. The size of the area patterned KBDRs is $1.1\,\mathrm{cm} \times 1.1\,\mathrm{cm}$. A photomicrograph of a fabricated sample is shown in Fig. 3.5(b)

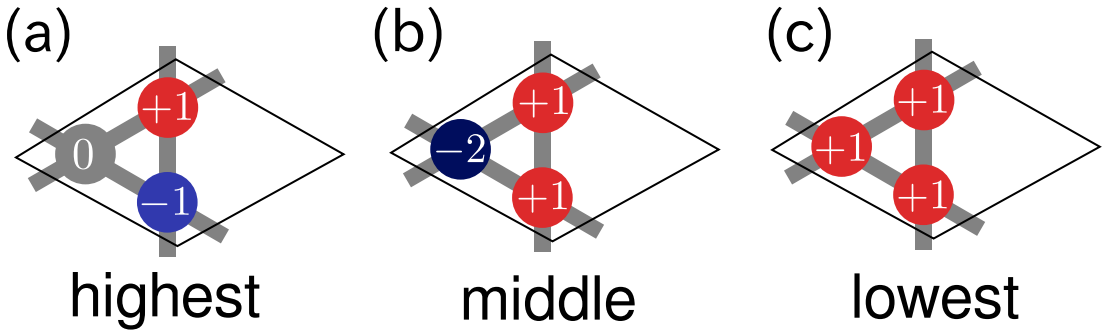

Figure 3.4: Eigenmodes near the Γ point - (a) The eigenmode of the highest band. (b) The eigenmode of the middle band. (c) The eigenmode of the lowest band.

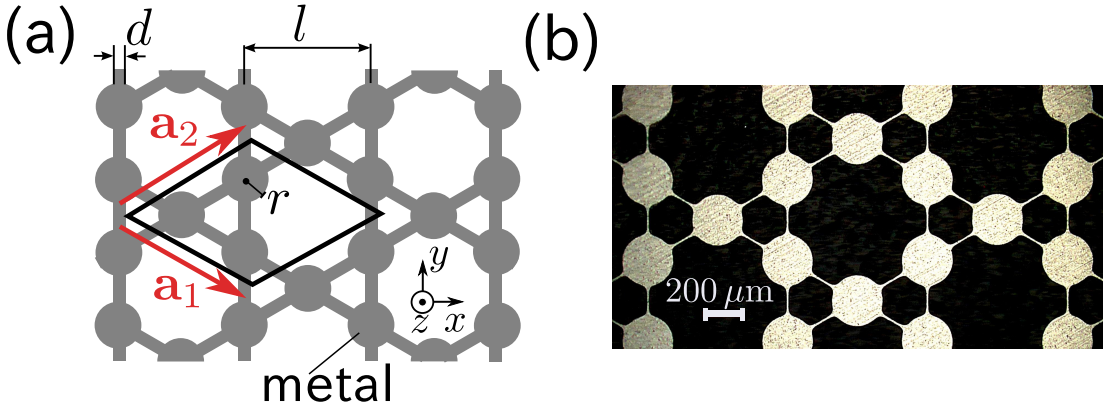

Figure 3.5: Sample of KBDRs - (a) Design. (b) Photomicrograph of a fabricated sample.

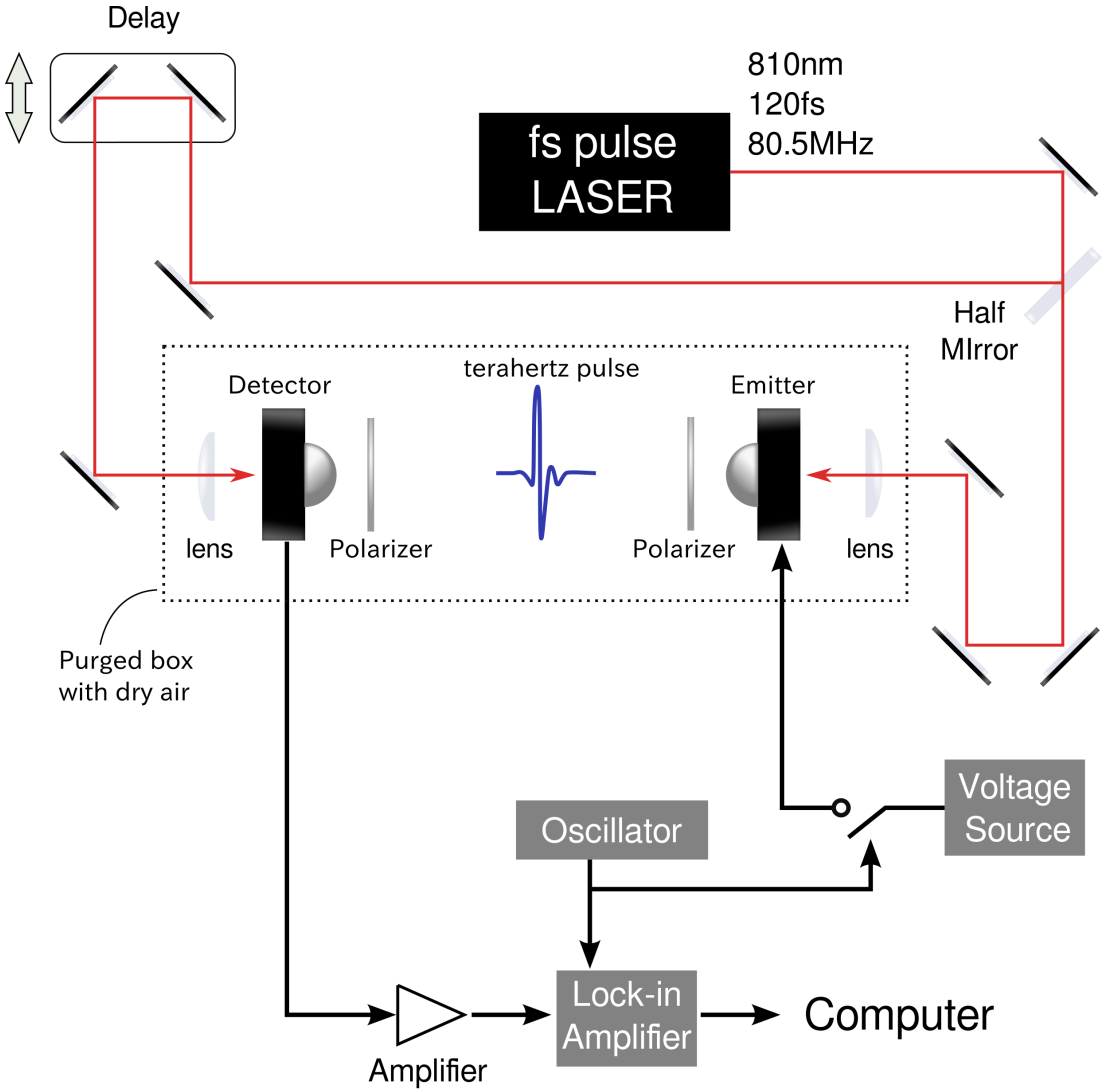

Figure 3.6: Experimental setup for terahertz time-domain spectroscopy - Photoconductive antennas are pumped by the fs laser, and signal is detected by the lock-in amplifier.

3.3.2 Terahertz time-domain spectroscopy

To investigate the dispersion relation experimentally, we use terahertz time-domain spectroscopy (THz-TDS), which is shown in Fig. 3.6. A terahertz emitter and detector (EKSPLA LTD.) with dipole antennas attached to Si lenses are used. These antennas are integrated on low-temperature-grown GaAs (LTGaAs) photoconductors, and driven by a femtosecond fiber laser (F-100, IMRA AMERICA, INC.) with a wavelength of 810 nm, a repetition rate 80.5 MHz, and pulse duration of 120 fs.

The emitter has two parallel metallic lines on the substrate. We apply the DC voltage $V_{\mathrm{DC}} = 45.8\,\mathrm{V}$ between these lines. Without pumping, two metallic lines are charged up. If this optical pulse has energy $\hbar\omega$ which is higher than the bandgap of LTGaAs, electron-hole pairs will be created by the optical pump. When the focused femtosecond pulse laser is irradiated to the gap between the metallic lines, current $I_{\mathrm{PC}}(t)$ flows rapidly and radiate the terahertz wave $\boldsymbol{E}_{\mathrm{THz}}$ as

$$\boldsymbol{E}_{\mathrm{THz}} \propto \frac{\mathrm{d}I_{\mathrm{PC}}(t-\frac{r}{c})}{\mathrm{d}t}, \tag{3.9}$$

where r is the distance between the position of photocurrent and an observation point [108]. Because rapid change of I_{PC} is needed to create a terahertz pulse, LTGaAs is often used as the substrate. LTGaAs has the ultrashort carrier lifetime resulting from a high concentration of defects, at which carriers are trapped and recombined. The generated terahertz beam is collimated with the Si lens near the emitter.

Similar structure is used for the detector. The terahertz beam is focused on the detector by an Si lens. Under pumping the gap with the femtosecond laser, the photocurrent flows as

$$I(t) = \int_{-\infty}^{t} \sigma_{\mathrm{s}}^{\mathrm{eff}}(t-t')E_{\mathrm{THz}}(t')\mathrm{d}t', \tag{3.10}$$

where $\sigma_{\mathrm{s}}^{\mathrm{eff}}(t)$ is the effective transient surface conductivity depending on the pumping femtosecond pulse, antenna shape, lens shape, and etc. For example, $\sigma_{\mathrm{s}}^{\mathrm{eff}}(t)$ includes the diffraction effect which causes the low efficiency of focusing at the low frequency. Then, we can see that photocurrent signal is not an exact replica of $E_{\mathrm{THz}}(t)$, but it is smoothed by $\sigma_{\mathrm{s}}^{\mathrm{eff}}(t)$. In the frequency domain, we have

$$\tilde{I}(\omega) = \tilde{\sigma}_{\mathrm{s}}^{\mathrm{eff}}(\omega)E_{\mathrm{THz}}(\omega). \tag{3.11}$$

The photocurrent of the detector is detected by lock-in technique. The internal oscillator of a lock-in amplifier (SR530, Stanford Research Systems) is used to modulate, and its frequency is set to 80 kHz. The applied DC voltage of the emitter is modulated by a switch synchronized with the oscillator. The photocurrent of the detector is preamplified by a current amplifier (Femto LCA-100K-50M), and detected by SR530. The time constant of the lock-in amplifier is set to 1 ms. In order to measure the waveform in the time domain, the displacement of the mirror is introduced to the laser path of the detector by an optical delay line (ScanDelay 150, APE). To reduce the absorption by water, the terahertz detector and the emitter are put in a box purged with dry air. Wire grid polarizers are used to select the polarization of the terahertz beams. We set the axes of two antennas are set as the same, and adjust the transparent axes of two polarizers as being parallel to the photocurrent.

An example of the measured signal without any samples is shown in Fig. 3.7. The pulse width of the terahertz beam is about 5 ps in time domain, and the band width is about 1.5 THz. Small variation of the curve in the frequency domain could be due to the astigmatism of collimating lenses [109].

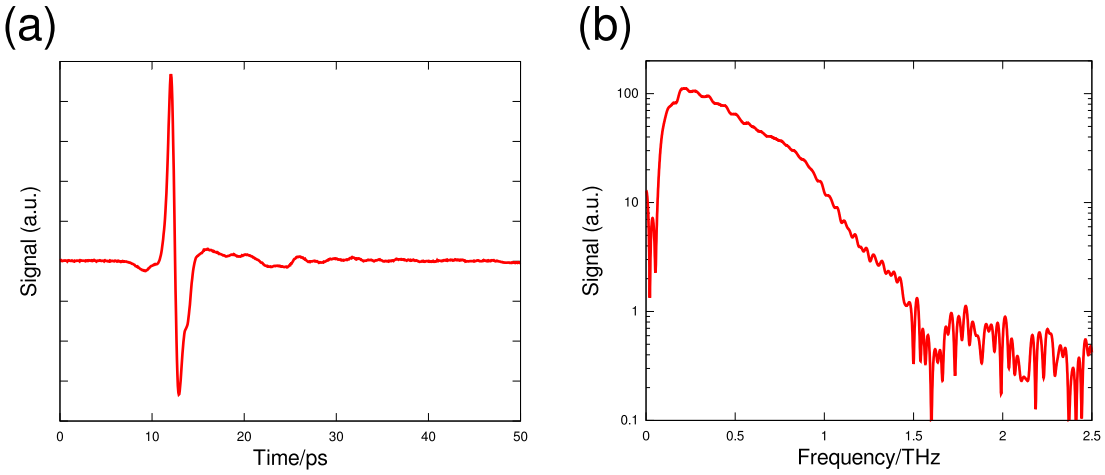

Figure 3.7: Reference signal corresponding to the electric field - (a) Time-domain signal. (b) Frequency-domain signal.

In order to obtain the band structure of KBDRs between the Γ point and the M point, the sample is rotated by θ with respect to the y axis from normal incidence (Fig. 3.8). The angles θ range from $\theta = 0°$ to $\theta = 65°$ with a step $\Delta\theta = 2.5°$. The magnitude of the wavevector $\boldsymbol{k}_{\parallel}$ on the sample plane is given by $k_{\parallel} = (\omega/c_0)\sin\theta$.

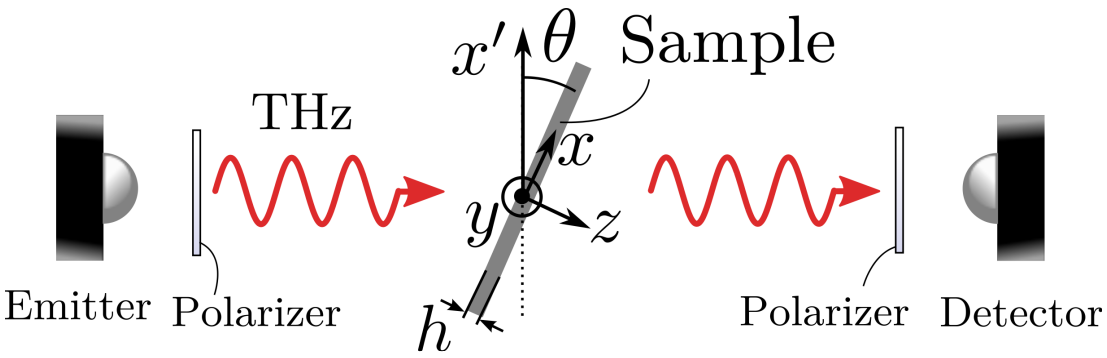

Figure 3.8: Schematic view of the transmission experiment - The plane of a sample is represented by the coordinate system (x, y) shown in Fig. 3.5(a).

We perform transmission experiments for two polarizations along the x' axis (parallel configuration) and y axis (perpendicular configuration). The transmission spectrum $T(\omega)$ is obtained from $|\tilde{I}(\omega)/\tilde{I}_{\mathrm{ref}}(\omega)|^2$, where $\tilde{I}(\omega)$ and $\tilde{I}_{\mathrm{ref}}(\omega)$ are Fourier transformed signals with and without the sample, respectively. Here, it is noted that the frequency-dependent $\tilde{\sigma}_{\mathrm{s}}^{\mathrm{eff}}(\omega)$ is canceled out. We denote the electric field of the incident wave as $\boldsymbol{E}$, and the projection of $\boldsymbol{E}$ to the sample plane as $\boldsymbol{E}_{\parallel}$. For parallel or perpendicular configurations, $\boldsymbol{E}_{\parallel}$ is parallel or perpendicular, respectively, to $\boldsymbol{k}_{\parallel}$. Wire-grid polarizers near the emitter and detector are adjusted so that the emitted and detected fields have the same polarization. The terahertz beam radius is about 3.7 mm, which covers a large number of KBDRs.

3.4 Results

Figure 3.9(a) displays the transmission spectrum for parallel configuration. The wavevectors are estimated as $k_{\parallel} = (\omega/c_0)\sin\theta$. Transmission spectrum minima are observed from 0.21 THz to 0.28 THz. With an increase of wavenumber, the frequency of the transmission minimum decreases from 0.28 THz at the Γ point and approaches 0.21 THz at the M point.

For further investigation, we calculate the electromagnetic response of KBDRs for parallel configuration. A commercial finite-element method solver (Ansoft HFSS) is used. In the simulation, a plane terahertz wave is injected into perfectly conducting KBDRs at an incident angle θ. By using periodic boundaries with some phase shifts, the transmission and the electromagnetic fields in the unit cell are calculated for an oblique

incident plane wave. The measured transmission spectra for $\theta = 20°$ are compared with the simulation in Fig. 3.9(b). The frequency of the transmission minimum and shape of the curve for the simulation are consistent with the experimental result, which confirms the validity of the assumption of perfect conductors.

Figure 3.9(c) shows the calculated distribution of surface electric charges at a minimum (0.255 THz) for $\theta = 20°$. This mode corresponds to the middle band shown in Fig. 3.4(b). Disks along the x axis are alternately charged. The in-phase currents along $\boldsymbol{a}_1$ and $\boldsymbol{a}_2$ are excited by the electromotive force due to $\boldsymbol{E}$. No resonance appears for $\theta = 0$ because the current flowing into a disk is balanced by the current flowing out of it. For the excitation of this mode, a phase-shifted field in the x-direction is needed.

By using Eq. (3.5), the fitting parameters are obtained from experimental data as $\omega_0/(2\pi) = 0.105\,\mathrm{THz}$ and $\kappa = 0.103$. The resultant dispersion curve is represented as a dotted curve in Fig. 3.9(a). Positive charges on one disk induce negative charges on the other; therefore, $\kappa < 0$ is ordinarily expected in the static limit ($\omega \to 0$). It seems strange that κ would be positive. In our situation, it can be explained by a retardation effect [110]. The phase shift between nearest disks is given by $(\omega_c/c) \times l/\sqrt{3} \sim 0.77 \times \pi$ at the center frequency $\omega_c/(2\pi) = 0.25\,\mathrm{THz}$ of the middle band. The near π shift leads to $\kappa > 0$. Although κ depends on frequency, we can approximately regard it as a constant between 0.2 THz and 0.3 THz.

Figure 3.10(a) displays the transmission spectrum for perpendicular configuration. Unlike in the case of parallel configuration, the flat band of the transmission minima is observed around 0.28 THz.

In order to confirm that the flat band is due to the interference, we perform a simulation for perpendicular configuration. A calculated transmission spectrum by simulation for $\theta = 20°$ is shown in Fig. 3.10(b) with the experimental data. We see a good agreement in the frequency of the transmission minimum and the shape of the curve. The calculated distribution of surface electric charges at a minimum (0.278 THz) for $\theta = 20°$ is shown in Fig. 3.10(c). The resonant mode has antisymmetric amplitudes on the right two disks and there is no charge stored on the left disk. This mode corresponds to the eigenmode in Fig. 3.4(a). Therefore, the flat transmission minima are caused by the topological nature of the kagomé lattice. The mode is excited by anti-phase electromotive force caused by $\boldsymbol{E}$ along bars parallel to $\boldsymbol{a}_1$ and $\boldsymbol{a}_2$. The electromotive force along vertical bars does not contribute to the storage of charges on

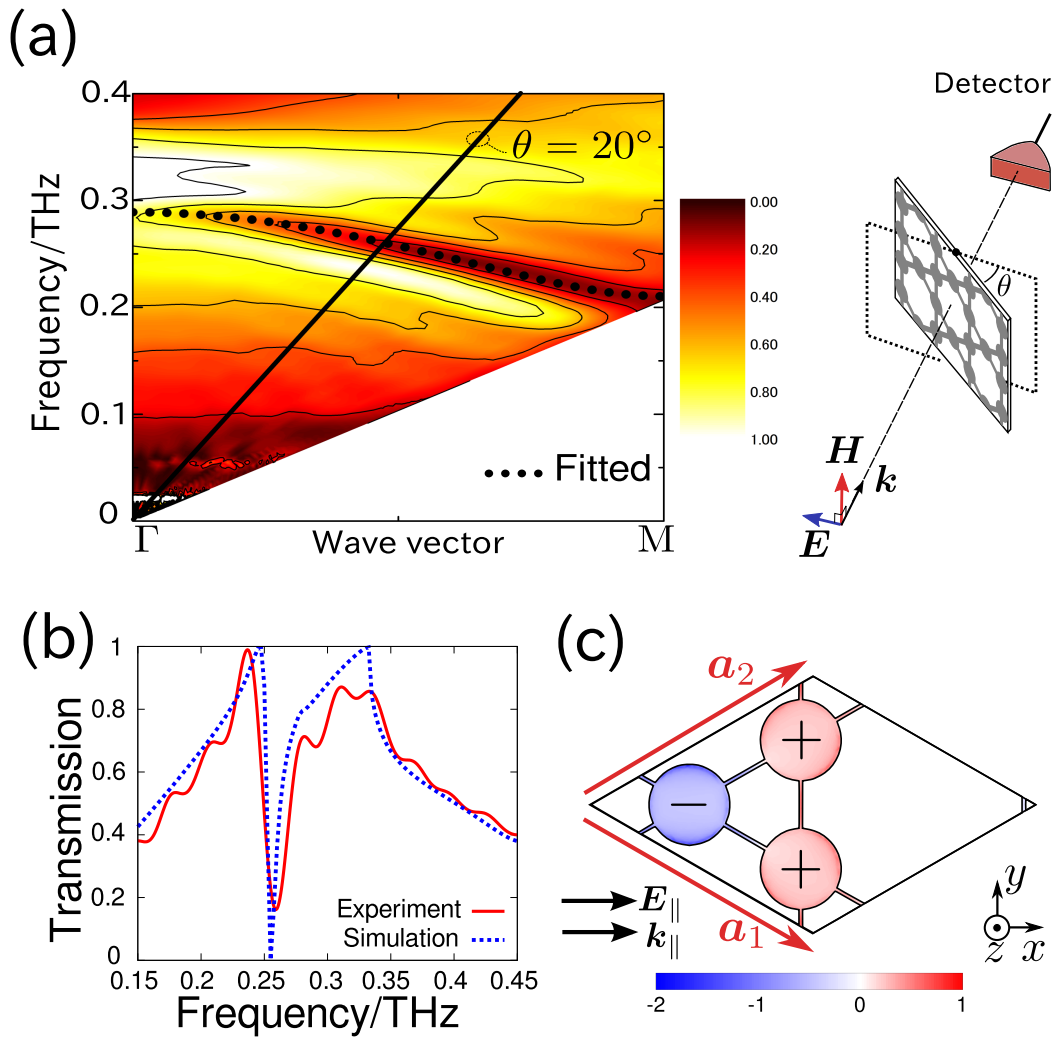

Figure 3.9: Parallel configuration ($\boldsymbol{E}_{\parallel} \parallel \boldsymbol{k}_{\parallel}$) - (a) Experimentally obtained transmission diagram of KBDRs. Transmission minima between 0.21 THz and 0.28 THz are observed and theoretically fitted by a dotted line. The experimental setup is also shown in the right. The solid line corresponds to $\theta = 20°$. (b) Transmission spectrum for $\theta = 20°$ obtained by simulation and experiment. (c) Surface electric charge distribution obtained by simulation at the transmission minimum 0.255 THz for $\theta = 20°$ in the unit cell.

disks because the currents flowing into and out of a disk are balanced. In the case of $\theta = 0$, the current flowing into a disk is equal to the current flowing out of it and the flat-band mode cannot be excited.

A dotted line in Fig. 3.10(a) represents the highest band given by Eq. (3.5) with the previously derived parameters $\omega_0/(2\pi) = 0.105\,\mathrm{THz}$ and $\kappa = 0.103$. It fits well with the minima experimentally obtained. The bend of the flat band caused by coupling to second (or higher) nearest sites is negligibly small, so the assumption of only nearest mutual disk coupling is appropriate.

3.5 Discussion

In Sec. 3.2, we derived the model of KBDRs through the model of KSHRs. Here, we derive another model of KBDRs directly. The electric potential of ϕ_i at the i-th disk can be described by charge q_j at j-th one as follows:

$$\phi_i = Uq_i + U' \sum_j A_{ij} q_j, \tag{3.12}$$

where we only consider self and nearest neighbor couplings, and U^{-1} have the dimension of capacitance. Assuming wave vector $\boldsymbol{k}_\parallel$ in the Fourier domain, Eq. (3.12) is reduced as

$$\begin{bmatrix} \tilde{\phi}_1 \\ \tilde{\phi}_2 \\ \tilde{\phi}_3 \end{bmatrix} = U \begin{bmatrix} 1 & [1+\mathrm{e}^{-\mathrm{i}\boldsymbol{k}_\parallel\cdot\boldsymbol{a}_2}]\eta & [1+\mathrm{e}^{-\mathrm{i}\boldsymbol{k}_\parallel\cdot\boldsymbol{a}_1}]\eta \\ [1+\mathrm{e}^{\mathrm{i}\boldsymbol{k}_\parallel\cdot\boldsymbol{a}_2}]\eta & 1 & [1+\mathrm{e}^{\mathrm{i}\boldsymbol{k}_\parallel\cdot(\boldsymbol{a}_2-\boldsymbol{a}_1)}]\eta \\ [1+\mathrm{e}^{\mathrm{i}\boldsymbol{k}_\parallel\cdot\boldsymbol{a}_1}]\eta & [1+\mathrm{e}^{\mathrm{i}\boldsymbol{k}_\parallel\cdot(\boldsymbol{a}_1-\boldsymbol{a}_2)}]\eta & 1 \end{bmatrix} \begin{bmatrix} \tilde{q}_1 \\ \tilde{q}_2 \\ \tilde{q}_3 \end{bmatrix} \tag{3.13}$$

with $\eta = U'/U$.

Next, we define current I_{ij} flowing from the j-th disk to the i-th disk. We assume that the bar between the i-th and j-th disks has only self-inductance L and ignore mutual inductance. The charge and the current induce electric field E_{ij} along I_{ij} as

$$E_{ij} \propto \phi_j - \phi_i - L\frac{\mathrm{d}I_{ij}}{\mathrm{d}t}. \tag{3.14}$$

For the case of no external excitation, $E_{ij} = 0$ must be satisfied. Then, we obtain

$$\frac{\mathrm{d}I_{ij}}{\mathrm{d}t} = -\frac{1}{L}(\phi_i - \phi_j). \tag{3.15}$$

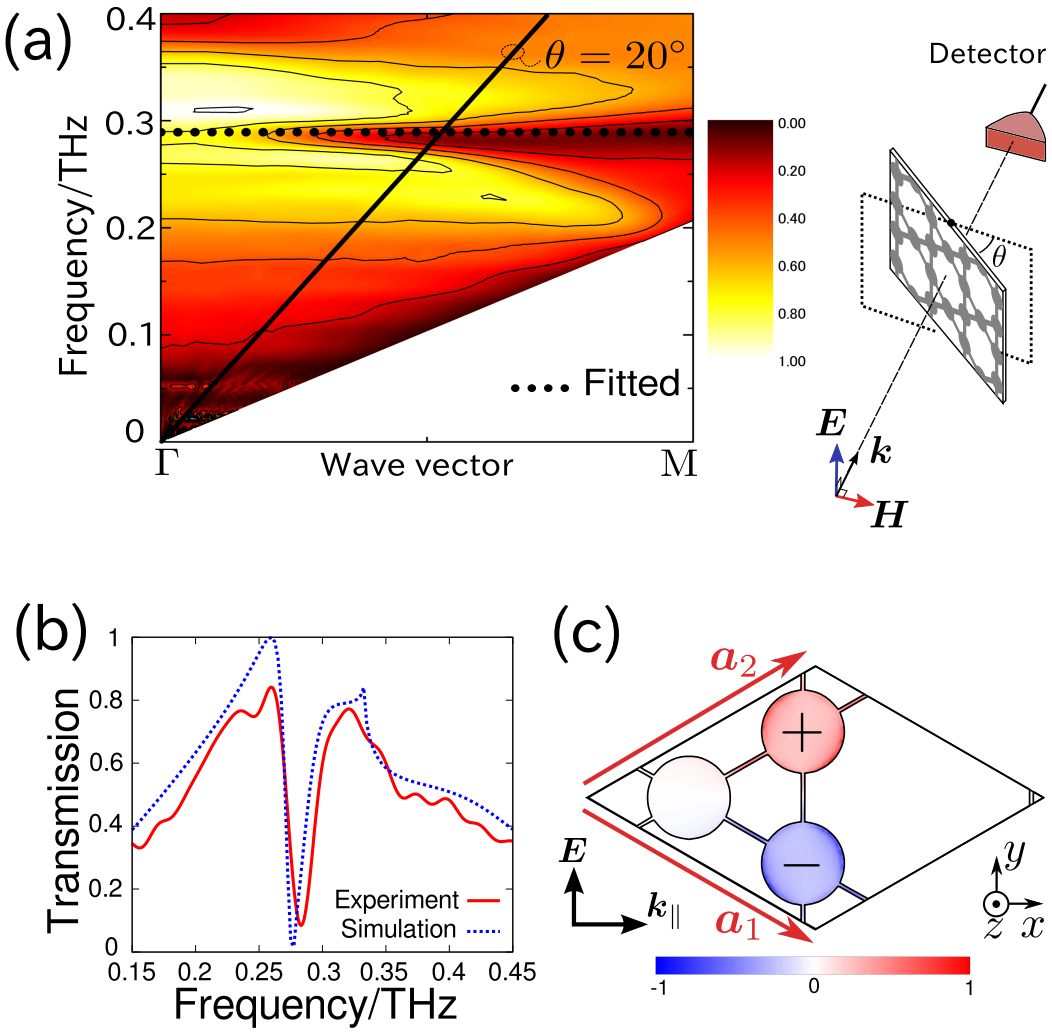

Figure 3.10: Perpendicular configuration ($\boldsymbol{E} \perp \boldsymbol{k}_{\parallel}$) - (a) Experimentally obtained transmission diagram of KBDRs. A flat transmission band is observed around 0.28 THz and theoretically fitted by the dotted line. The solid line corresponds to $\theta = 20°$. The experimental setup is also shown in the right. (b) Transmission spectrum for $\theta = 20°$ obtained by simulation and experiment. (c) Surface electric charge distribution obtained by simulation at a transmission minimum of 0.278 THz for $\theta = 20°$ in the unit cell.

Now, we consider charge conservation law. The charge conservation law at the i-th disk is written as follows:

$$\frac{\mathrm{d}q_i}{\mathrm{d}t} = \sum_j A_{ij} I_{ij}. \tag{3.16}$$

From Eqs. (3.15) and (3.16), we obtain

$$\frac{\mathrm{d}^2 q_i}{\mathrm{d}t^2} = -\frac{1}{L} \sum_j A_{ij} (\phi_i - \phi_j). \tag{3.17}$$

For KBDRs, Eq. (3.17) is reduced to

$$\frac{1}{L} \begin{bmatrix} 4 & -[1+\mathrm{e}^{-\mathrm{i}\boldsymbol{k}_\parallel \cdot \boldsymbol{a}_2}] & -[1+\mathrm{e}^{-\mathrm{i}\boldsymbol{k}_\parallel \cdot \boldsymbol{a}_1}] \\ -[1+\mathrm{e}^{\mathrm{i}\boldsymbol{k}_\parallel \cdot \boldsymbol{a}_2}] & 4 & -[1+\mathrm{e}^{\mathrm{i}\boldsymbol{k}_\parallel \cdot (\boldsymbol{a}_2 - \boldsymbol{a}_1)}] \\ -[1+\mathrm{e}^{\mathrm{i}\boldsymbol{k}_\parallel \cdot \boldsymbol{a}_1}] & -[1+\mathrm{e}^{\mathrm{i}\boldsymbol{k}_\parallel \cdot (\boldsymbol{a}_1 - \boldsymbol{a}_2)}] & 4 \end{bmatrix} \begin{bmatrix} \tilde{\phi}_1 \\ \tilde{\phi}_2 \\ \tilde{\phi}_3 \end{bmatrix} = \omega^2 \begin{bmatrix} \tilde{q}_1 \\ \tilde{q}_2 \\ \tilde{q}_3 \end{bmatrix} \tag{3.18}$$

in the frequency domain. Finally, we obtain

$$H \begin{bmatrix} \tilde{q}_1 \\ \tilde{q}_2 \\ \tilde{q}_3 \end{bmatrix} = \left(\frac{\omega}{\omega_0} \right)^2 \begin{bmatrix} \tilde{q}_1 \\ \tilde{q}_2 \\ \tilde{q}_3 \end{bmatrix}, \tag{3.19}$$

where $H = SX$, and $\omega_o = \sqrt{U/L}$. Here, S and X are defined as follows:

$$S := \begin{bmatrix} 1 & [1+\mathrm{e}^{-\mathrm{i}\boldsymbol{k}_\parallel \cdot \boldsymbol{a}_2}]\eta & [1+\mathrm{e}^{-\mathrm{i}\boldsymbol{k}_\parallel \cdot \boldsymbol{a}_1}]\eta \\ [1+\mathrm{e}^{\mathrm{i}\boldsymbol{k}_\parallel \cdot \boldsymbol{a}_2}]\eta & 1 & [1+\mathrm{e}^{\mathrm{i}\boldsymbol{k}_\parallel \cdot (\boldsymbol{a}_2 - \boldsymbol{a}_1)}]\eta \\ [1+\mathrm{e}^{\mathrm{i}\boldsymbol{k}_\parallel \cdot \boldsymbol{a}_1}]\eta & [1+\mathrm{e}^{\mathrm{i}\boldsymbol{k}_\parallel \cdot (\boldsymbol{a}_1 - \boldsymbol{a}_2)}]\eta & 1 \end{bmatrix}, \tag{3.20}$$

$$X := \begin{bmatrix} 4 & -[1+\mathrm{e}^{-\mathrm{i}\boldsymbol{k}_\parallel \cdot \boldsymbol{a}_2}] & -[1+\mathrm{e}^{-\mathrm{i}\boldsymbol{k}_\parallel \cdot \boldsymbol{a}_1}] \\ -[1+\mathrm{e}^{\mathrm{i}\boldsymbol{k}_\parallel \cdot \boldsymbol{a}_2}] & 4 & -[1+\mathrm{e}^{\mathrm{i}\boldsymbol{k}_\parallel \cdot (\boldsymbol{a}_2 - \boldsymbol{a}_1)}] \\ -[1+\mathrm{e}^{\mathrm{i}\boldsymbol{k}_\parallel \cdot \boldsymbol{a}_1}] & -[1+\mathrm{e}^{\mathrm{i}\boldsymbol{k}_\parallel \cdot (\boldsymbol{a}_1 - \boldsymbol{a}_2)}] & 4 \end{bmatrix}. \tag{3.21}$$

Solving Eq. (3.19), we find

$$\frac{\omega}{\omega_0} = \sqrt{6-12\eta}, \sqrt{3-2\eta F \pm \sqrt{3+2F+12\eta(\eta-1)+8\eta(\eta-1)F}}. \tag{3.22}$$

Although Eq (3.22) is different from Eq. (3.5), we can see the qualitative similarity between them: (i) flat-band formation and (ii) coupling coefficients κ and η govern the closeness between the second and third highest bands. We fit the reflection band for parallel configuration by using Eq. (3.22), and obtain $\eta = -0.143$ and $\omega_0 = 2\pi \times 0.104\,\mathrm{THz}$. The fitted curve is shown in Fig. 3.11.

Electromagnetic flat bands for all crystal directions have been reported for photonic crystals with square symmetry, theoretically [111] and experimentally [112]. In this

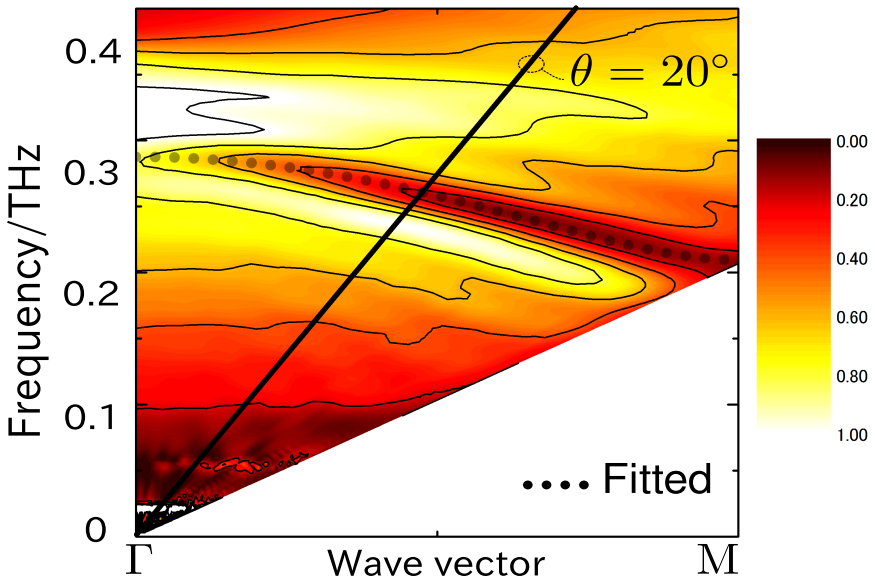

Figure 3.11: Another fitting for parallel configuration ($\boldsymbol{E}_{\parallel} \parallel \boldsymbol{k}_{\parallel}$) - The transmission minima are fitted by Eq. (3.22).

case, the flat bands are formed due to good lateral confinement (high Q factor) of the quadropole modes, which lack preferential coupling directions, at defects of photonic crystals. On the other hand, the flat band for KBDRs is not caused by highly confined modes, but by the topological nature of the kagomé lattice. The kagomé lattice prevents excited modes from propagating despite the existence of strong coupling. Thus, the physical origin of the flat band on KBDRs differs from that for photonic crystals [111, 112]. We note that the flat band for propagating modes has been theoretically predicted for square waveguide networks [105]. Our system is considered as an experimental realization of the flat band for the propagating mode.

The flat band in the kagomé lattice comes from local interference effects. The global symmetry (i.e., periodicity of the lattice) is not necessarily required because local symmetries can support the localized mode. The resonance independent of the incident angle could be expected for the metallic structure having localized modes with the same resonant frequency, even without periodicity.

3.6 Summary

In this chapter, we studied theoretically and experimentally the electromagnetic flat band on a metallic kagomé lattice. Kagomé-type bar-disk resonators were proposed to realize the flat band. A dispersion relation composed of three bands was theoretically predicted for KBDRs. The highest band was flat for all wavevectors. Two bands formed by transmission minima depending on the polarization of the incident terahertz beams were observed experimentally. One of the bands corresponded to the flat band. Theoretical fitting showed good agreement for these modes. By simulation, we revealed that the flat band was caused by the topological nature of the kagomé lattice.

The flat band can be applicable to slow light, which is useful for the control of group velocity [113, 114], high sensitive sensing, and other applications. In the flat band, the effective mass of photons becomes very heavy and their correlation has an important role. Multiphoton correlation effects in kagomé lattices are important in terms of fundamental physics and should be studied in the future.

Chapter 4

Frequency-independent response of self-complementary metasurfaces

4.1 Background

In addition to isometric symmetry of metamaterials, the theory of electromagnetism has another symmetry with respect to the interchange of electric and magnetic fields. This symmetry is called the *electromagnetic duality*, and can be generalized to a continuous symmetry with respect to internal rotations of electric and magnetic fields. This continuous symmetry is directly related to a helicity conservation law [115–122]. We note that these symmetries had been gradually discovered since the late 19th century [123–125].

The electromagnetic duality is closely related to Babinet's principle [126]. Given a thin metallic metasurface, we can construct the complementary metasurface by using a structural inversion to interchange the holes and the metals. Babinet's principle relates the scattering fields of the complementary metasurfaces to those of the original one. This principle is based on the fact that the structural inversion is consistent with electromagnetic duality. A rigorous Babinet's principle for electromagnetic waves was simultaneously formulated by several groups [127–132]. It was extended to absorbing surfaces [133], impedance surfaces [134, 135], and surfaces with lumped elements [136]. It is important to note that the generalization for impedance surfaces was performed by extending the structural inversion to the impedance one. Recently, several complementary metasurfaces have been fabricated and tested in the microwave [137, 138],

terahertz [139], and near-infrared regions [140]. Near-field images of complementary metasurfaces have been obtained in the terahertz range [141]. and switching of reflection has been realized by using a complementary metasurface with a twisted nematic cell in the near-infrared region [142]. Babinet's principle is also useful for designing negative refractive index metamaterials [143].

Generally, the structure of a metasurface is not invariant under impedance inversion. If a metasurface is identical to its complement, it is called a *self-complementary* metasurface. As an application, such self-complementary artificial surfaces have been used for efficient polarizers [144, 145]. In the field of antenna design, it is known that a self-complementary antenna has a constant input impedance [146, 147]. Therefore, self-complementary metasurfaces are expected to exhibit a frequency-independent response. It has been shown that an almost self-complementary spiral terahertz metasurface has a constant response only in the high-frequency range [148]. There have been some efforts to achieve a frequency-independent response with self-complementary checkerboard metasurfaces [149, 150], but it is known empirically that such a metasurface does not exist. Self-complementary metasurfaces have not been analyzed thoroughly enough; for example, conditions for the frequency-independent response have not been discussed thoroughly, and an elaborate theory is needed. In this chapter, we study electromagnetic scattering by self-complementary metasurfaces more rigorously and establish several useful theorems. In particular, we focus on the incidences of circularly polarized plane waves onto self-complementary metasurfaces, because circularly polarized light matches with electromagnetic duality.

4.2 Electromagnetic duality

The electric and magnetic fields are represented by a polar vector field $\boldsymbol{E}$ and an axial vector field $\boldsymbol{H}$, respectively. Under spatial inversion, polar vectors are reversed in direction, while axial vectors are invariant. If we fix the orientation of the three-dimensional Euclid space $\mathbb{E}_3$, axial vectors are represented by two polar vectors corresponding to the two orientations of $\mathbb{E}_3$, respectively [151]. Two types of vectors are required in order not to assume specific orientation of space $\mathbb{E}_3$. An electromagnetic field is represented by $(\boldsymbol{E}, \boldsymbol{H})$. The set of electromagnetic fields constitutes a vector space, namely, a direct

sum of vector spaces, with the scalar product defined by $s(\boldsymbol{E}, \boldsymbol{H}) := (s\boldsymbol{E}, s\boldsymbol{H})$ for a scalar s, and the sum $(\boldsymbol{E}_1, \boldsymbol{H}_1) + (\boldsymbol{E}_2, \boldsymbol{H}_2) := (\boldsymbol{E}_1 + \boldsymbol{E}_2, \boldsymbol{H}_1 + \boldsymbol{H}_2)$.

Maxwell's theory of electromagnetism has an internal symmetry between electric and magnetic fields, but the symmetry operation is not a simple exchange. Maxwell's equations without sources and the vacuum constitutive relations ($\boldsymbol{D} = \varepsilon_0 \boldsymbol{E}$ and $\boldsymbol{B} = \mu_0 \boldsymbol{H}$) are invariant under the following transformation:

$$\boldsymbol{E} \to Z_0 \boldsymbol{H}, \qquad \boldsymbol{H} \to -\boldsymbol{E}/Z_0, \tag{4.1}$$

$$\boldsymbol{D} \to \boldsymbol{B}/Z_0, \qquad \boldsymbol{B} \to -Z_0 \boldsymbol{D}, \tag{4.2}$$

with electric displacement $\boldsymbol{D}$ and magnetic flux density $\boldsymbol{B}$. The permittivity, permeability, and impedance of vacuum are represented by ε_0, μ_0, and the intrinsic impedance of vacuum $Z_0 = \sqrt{\mu_0/\varepsilon_0}$, respectively. This internal symmetry is called the "electromagnetic duality." Note that we need to fix an orientation of $\mathbb{E}_3$ to exchange polar and axial vectors by using Eqs. (4.1) and (4.2). This is similar to considering an imaginary number i as an anti-clockwise rotation by $\pi/2$, which determines an orientation of the complex plane. It is also valid to use $\mathrm{j} = -\mathrm{i}$ as an anti-clockwise rotation (this is the convention in engineering). In the rest of this work, we use the right-handed system for internal transformations.

The electromagnetic duality extends to a continuous symmetry of electromagnetic fields. The duality rotation by θ is defined by

$$\mathcal{R}_\theta(\boldsymbol{E}, \boldsymbol{H}) = \left(\boldsymbol{E}\cos\theta + Z_0 \boldsymbol{H}\sin\theta, -\frac{\boldsymbol{E}}{Z_0}\sin\theta + \boldsymbol{H}\cos\theta\right). \tag{4.3}$$

This transformation is considered to be a rotation with respect to the internal degree of freedom. The transformation given by Eqs. (4.1) and (4.2) corresponds to the duality rotation by $\theta = \pi/2$. The duality rotation mixes the two linear polarized plane waves. Here, we use tildes to represent the complex amplitudes for sinusoidally oscillating fields with angular frequency ω. For example, a sinusoidally oscillating real-valued scalar field F is represented by $F = \tilde{F}\mathrm{e}^{-\mathrm{i}\omega t} + \tilde{F}^*\mathrm{e}^{\mathrm{i}\omega t}$, where $\tilde{F}$ is the complex amplitude and $\tilde{F}^*$ is its complex conjugate. With this notation, we have $\mathcal{R}_\theta(\tilde{\boldsymbol{E}}_{\mathrm{LCP}}, \tilde{\boldsymbol{H}}_{\mathrm{LCP}}) = \mathrm{e}^{-\mathrm{i}\theta}(\tilde{\boldsymbol{E}}_{\mathrm{LCP}}, \tilde{\boldsymbol{H}}_{\mathrm{LCP}})$ for a left circularly polarized wave $(\tilde{\boldsymbol{E}}_{\mathrm{LCP}}, \tilde{\boldsymbol{H}}_{\mathrm{LCP}})$ from the point of view of the receiver. For a right circularly polarized wave $(\tilde{\boldsymbol{E}}_{\mathrm{RCP}}, \tilde{\boldsymbol{H}}_{\mathrm{RCP}})$, $\mathcal{R}_\theta(\tilde{\boldsymbol{E}}_{\mathrm{RCP}}, \tilde{\boldsymbol{H}}_{\mathrm{RCP}}) = \mathrm{e}^{\mathrm{i}\theta}(\tilde{\boldsymbol{E}}_{\mathrm{RCP}}, \tilde{\boldsymbol{H}}_{\mathrm{RCP}})$ is satisfied. Therefore, circularly polarized plane waves are eigenstates of $\mathcal{R}_\theta$.

4.3 Babinet's principle for metasurfaces with resistive elements

In this section, we derive Babinet's principle for metasurfaces with resistive elements. In deriving Babinet's principle, we consider two scattering problems. We assume that a metasurface is placed in a vacuum for each problem. In the first problem [problem (a)],

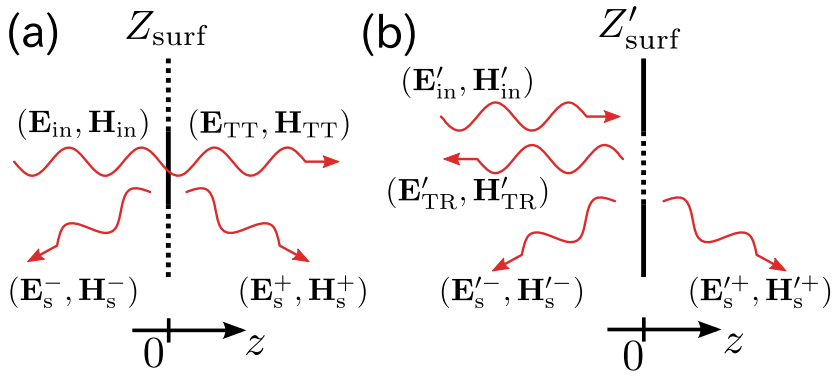

Figure 4.1: Two problems - These problems are related through Babinet's principle.

an incident electromagnetic wave $(\boldsymbol{E}_{\mathrm{in}}, \boldsymbol{H}_{\mathrm{in}})$ is scattered by the metasurface with a surface impedance Z_{surf} on the surface $z = 0$ [see Fig. 4.1(a)]. Note that Z_{surf} is a function of (x, y), but we omit the parameters for simplicity. The incident wave radiates from the sources in $z \leq 0$. If there was no metasurface, the source would produce $(\boldsymbol{E}_{\mathrm{in}}, \boldsymbol{H}_{\mathrm{in}})$ in $z \leq 0$ and $(\boldsymbol{E}_{\mathrm{TT}}, \boldsymbol{H}_{\mathrm{TT}})$ in $z \geq 0$. Here, TT represents a totally transmitted wave. The incident wave is not restricted to plane waves and can even include near-field components. If there is a metasurface, surface currents and charges are induced by the incident wave. They radiate the following scattered fields: $(\boldsymbol{E}_{\mathrm{s}}^{-}, \boldsymbol{H}_{\mathrm{s}}^{-})$ in $z \leq 0$ and $(\boldsymbol{E}_{\mathrm{s}}^{+}, \boldsymbol{H}_{\mathrm{s}}^{+})$ in $z \geq 0$.

Next, we set up the second problem [problem (b)]. In this problem, an incident wave $(\boldsymbol{E}'_{\mathrm{in}}, \boldsymbol{H}'_{\mathrm{in}})$ from sources in $z \leq 0$ enters the metasurface at $z = 0$ with a surface impedance Z'_{surf} varying on $z = 0$ [see Fig. 4.1(b)]. Here, $(\boldsymbol{E}'_{\mathrm{in}}, \boldsymbol{H}'_{\mathrm{in}})$ is defined in $z \leq 0$. If a perfect electric conductor (PEC) sheet is placed at $z = 0$, the incident wave is totally reflected. This totally reflected wave in $z \leq 0$ is represented by $(\boldsymbol{E}'_{\mathrm{TR}}, \boldsymbol{H}'_{\mathrm{TR}})$. The effect of the metasurface that differs from the PEC sheet emerges as the remaining fields $(\boldsymbol{E}_{\mathrm{s}}'^{\pm}, \boldsymbol{H}_{\mathrm{s}}'^{\pm})$, where $-$ and $+$ represent the fields in $z \leq 0$ and $z \geq 0$, respectively.

In general, these two problems are completely distinct. If we assume a specific condition for the surface impedances, the scattering fields of the two problems are related as described in the following theorem.

Theorem 1. *We assume that the incident wave is* $(\boldsymbol{E}'_{\mathrm{in}}, \boldsymbol{H}'_{\mathrm{in}}) = \mathcal{R}_{-\pi/2}(\boldsymbol{E}_{\mathrm{in}}, \boldsymbol{H}_{\mathrm{in}}) = (-Z_0\boldsymbol{H}_{\mathrm{in}}, \boldsymbol{E}_{\mathrm{in}}/Z_0)$*. If* Z_{surf} *and* Z'_{surf} *satisfy* $Z_{\mathrm{surf}}\, Z'_{\mathrm{surf}} = (Z_0/2)^2$ *at any point with* $z = 0$*, the scattering fields of problem (b) are given by* $(\boldsymbol{E}'^{\pm}_{\mathrm{s}}, \boldsymbol{H}'^{\pm}_{\mathrm{s}}) = \mathcal{R}_{\pm\pi/2}(\boldsymbol{E}^{\pm}_{\mathrm{s}}, \boldsymbol{H}^{\pm}_{\mathrm{s}}) = \pm(Z_0\boldsymbol{H}^{\pm}_{\mathrm{s}}, -\boldsymbol{E}^{\pm}_{\mathrm{s}}/Z_0)$ *using the solution of problem (a).*

Proof. Here, we define a unit vector $\boldsymbol{e}_z$ parallel to the z axis, and the projection operator $\mathcal{P} = -\boldsymbol{e}_z \times \boldsymbol{e}_z\times$, which eliminates z-components of vectors. First, we consider problem (a). The scattered fields $(\boldsymbol{E}^{\pm}_{\mathrm{s}}, \boldsymbol{H}^{\pm}_{\mathrm{s}})$ are symmetric with respect to $z = 0$. Then, $\mathcal{P}\boldsymbol{E}^{+}_{\mathrm{s}} = \mathcal{P}\boldsymbol{E}^{-}_{\mathrm{s}}$ and $\mathcal{P}\boldsymbol{H}^{+}_{\mathrm{s}} = -\mathcal{P}\boldsymbol{H}^{-}_{\mathrm{s}}$ are satisfied on $z = 0$. The electric boundary condition $\mathcal{P}(\boldsymbol{E}_{\mathrm{TT}} + \boldsymbol{E}^{+}_{\mathrm{s}}) = \mathcal{P}(\boldsymbol{E}_{\mathrm{in}} + \boldsymbol{E}^{-}_{\mathrm{s}})$ on $z = 0$ is automatically satisfied. Another boundary condition on $z = 0$ is given by $\mathcal{P}(\boldsymbol{E}_{\mathrm{in}} + \boldsymbol{E}^{-}_{\mathrm{s}}) = Z_{\mathrm{surf}}\, \boldsymbol{e}_z \times (\boldsymbol{H}^{+}_{\mathrm{s}} - \boldsymbol{H}^{-}_{\mathrm{s}})$. With $\mathcal{P}\boldsymbol{H}^{+}_{\mathrm{s}} = -\mathcal{P}\boldsymbol{H}^{-}_{\mathrm{s}}$, we obtain the following equation for $z = 0$:

$$\mathcal{P}(\boldsymbol{E}_{\mathrm{in}} + \boldsymbol{E}^{-}_{\mathrm{s}}) = 2Z_{\mathrm{surf}}\, \boldsymbol{e}_z \times \boldsymbol{H}^{+}_{\mathrm{s}}. \tag{4.4}$$

In problem (b), we show that the fields $(\boldsymbol{E}'^{\pm}_{\mathrm{s}}, \boldsymbol{H}'^{\pm}_{\mathrm{s}})$ defined by $\mathcal{R}_{\pm\pi/2}(\boldsymbol{E}^{\pm}_{\mathrm{s}}, \boldsymbol{H}^{\pm}_{\mathrm{s}})$ satisfy all boundary conditions for the incident wave $(\boldsymbol{E}'_{\mathrm{in}}, \boldsymbol{H}'_{\mathrm{in}}) = \mathcal{R}_{-\pi/2}(\boldsymbol{E}_{\mathrm{in}}, \boldsymbol{H}_{\mathrm{in}})$. The fields $(\boldsymbol{E}'^{\pm}_{\mathrm{s}}, \boldsymbol{H}'^{\pm}_{\mathrm{s}}) = \pm(Z_0\boldsymbol{H}^{\pm}_{\mathrm{s}}, -\boldsymbol{E}^{\pm}_{\mathrm{s}}/Z_0)$ are also symmetric with respect to $z = 0$. From $\mathcal{P}\boldsymbol{E}'_{\mathrm{in}} = -\mathcal{P}\boldsymbol{E}'_{\mathrm{TR}}$ and $\mathcal{P}\boldsymbol{E}'^{-}_{\mathrm{s}} = \mathcal{P}\boldsymbol{E}'^{+}_{\mathrm{s}}$ on $z = 0$, the electric boundary condition $\mathcal{P}(\boldsymbol{E}'_{\mathrm{in}}+\boldsymbol{E}'_{\mathrm{TR}}+\boldsymbol{E}'^{-}_{\mathrm{s}}) = \mathcal{P}\boldsymbol{E}'^{+}_{\mathrm{s}}$ is satisfied. Additionally, the following boundary condition should be satisfied on $z = 0$:

$$\begin{aligned}\mathcal{P}\boldsymbol{E}'^{+}_{\mathrm{s}} &= Z'_{\mathrm{surf}}\, \boldsymbol{e}_z \times (\boldsymbol{H}'^{+}_{\mathrm{s}} - \boldsymbol{H}'^{-}_{\mathrm{s}} - \boldsymbol{H}'_{\mathrm{in}} - \boldsymbol{H}'_{\mathrm{TR}}) \\ &= -2Z'_{\mathrm{surf}}\, \boldsymbol{e}_z \times (\boldsymbol{H}'_{\mathrm{in}} + \boldsymbol{H}'^{-}_{\mathrm{s}}),\end{aligned} \tag{4.5}$$

where we use $\mathcal{P}\boldsymbol{H}'^{+}_{\mathrm{s}} = -\mathcal{P}\boldsymbol{H}'^{-}_{\mathrm{s}}$ and $\mathcal{P}\boldsymbol{H}'_{\mathrm{in}} = \mathcal{P}\boldsymbol{H}'_{\mathrm{TR}}$ on $z = 0$ (the derivation of $\mathcal{P}\boldsymbol{H}'_{\mathrm{in}} = \mathcal{P}\boldsymbol{H}'_{\mathrm{TR}}$ is shown in Appendix A.1). Operating with $\boldsymbol{e}_z\times$ on Eq. (4.5) and comparing with Eq. (4.4), we have $Z_{\mathrm{surf}}\, Z'_{\mathrm{surf}} = (Z_0/2)^2$. Thus all boundary conditions are satisfied for problem (b) with $Z'_{\mathrm{surf}} = {Z_0}^2/(4Z_{\mathrm{surf}})$. □

For the case of $Z_{\mathrm{surf}} = \infty$ (hole), the complementary surface is PEC with $Z'_{\mathrm{surf}} = 0$, and vice versa. Therefore, the above theorem includes the standard Babinet's principle.

The extensions for tensor impedances [134] and lumped elements [136] have also been investigated.

Next, we discuss the relationship of the transmission and reflection coefficients in problems (a) and (b). From here on, we assume that all fields oscillate sinusoidally with angular frequency ω and are represented by complex amplitudes. We consider a periodic metasurface with lattice vectors $\boldsymbol{a}_1$ and $\boldsymbol{a}_2$. Physically, a metasurface without periodicity can be regarded as $|\boldsymbol{a}_1|,\ |\boldsymbol{a}_2| \to \infty$. This corresponds to the transition from box quantization to free space quantization in quantum mechanics. The reciprocal vectors are represented by $\boldsymbol{b}_1$ and $\boldsymbol{b}_2$ satisfying $\boldsymbol{a}_i \cdot \boldsymbol{b}_j = 2\pi\delta_{ij}$ (δ_{ij} is the Kronecker delta). Additionally, we assume that the incident wave is a plane wave $(\tilde{\boldsymbol{E}}_{\mathrm{in}}, \tilde{\boldsymbol{H}}_{\mathrm{in}}) = (\check{\boldsymbol{E}}_0 \mathrm{e}^{\mathrm{i}\boldsymbol{k}_0\cdot\boldsymbol{x}}, \check{\boldsymbol{H}}_0 \mathrm{e}^{\mathrm{i}\boldsymbol{k}_0\cdot\boldsymbol{x}})$ with $\check{\boldsymbol{H}}_0 = {Z_0}^{-1}\boldsymbol{k}_0 \times \check{\boldsymbol{E}}_0/|\boldsymbol{k}_0|$ for a wave vector $\boldsymbol{k}_0$. Here we use the checkmark symbol in order to express complex amplitudes for a plane wave with a definite wave vector.

In problem (a), the scattered wave $(\tilde{\boldsymbol{E}}_{\mathrm{s}}^{+}, \tilde{\boldsymbol{H}}_{\mathrm{s}}^{+})$ on $z = 0$ has Fourier components with the in-plane wave vector $\underline{\boldsymbol{k}}_{pq} := p\boldsymbol{b}_1 + q\boldsymbol{b}_2 + \mathcal{P}\boldsymbol{k}_0$ for $(p, q) \in \mathbb{Z}^2$. In this chapter, we focus on the 0th-order modes with $(p, q) = (0, 0)$ in order to simplify the notation. The general case is summarized in Appendix A.2. We decompose the 0th-order complex fields of problem (a) in $z \geq 0$ as $\sum_{\alpha=1,2} t_\alpha(\tilde{\boldsymbol{E}}_\alpha^{+}, \tilde{\boldsymbol{H}}_\alpha^{+})$ with complex transmission coefficients t_α, where we define $(\tilde{\boldsymbol{E}}_1^{+}, \tilde{\boldsymbol{H}}_1^{+}) := (\tilde{\boldsymbol{E}}_{\mathrm{TT}}, \tilde{\boldsymbol{H}}_{\mathrm{TT}})$, and its perpendicular polarization state $(\tilde{\boldsymbol{E}}_2^{+}, \tilde{\boldsymbol{H}}_2^{+})$. The mode $(\tilde{\boldsymbol{E}}_2^{+}, \tilde{\boldsymbol{H}}_2^{+})$ is normalized to carry the same power flow of $(\tilde{\boldsymbol{E}}_1^{+}, \tilde{\boldsymbol{H}}_1^{+})$. We also define $(\tilde{\boldsymbol{E}}_\alpha^{-}, \tilde{\boldsymbol{H}}_\alpha^{-})$ as the mirror symmetric field of $(\tilde{\boldsymbol{E}}_\alpha^{+}, \tilde{\boldsymbol{H}}_\alpha^{+})$ with respect to $z = 0$. In $z \leq 0$, the 0th-order field is represented by $(\tilde{\boldsymbol{E}}_{\mathrm{in}}, \tilde{\boldsymbol{H}}_{\mathrm{in}}) + \sum_{\alpha=1,2} r_\alpha(\tilde{\boldsymbol{E}}_\alpha^{-}, \tilde{\boldsymbol{H}}_\alpha^{-})$ with complex reflection coefficients r_α. For problem (b), we define $(\tilde{\boldsymbol{E}}_\alpha^{\prime\pm}, \tilde{\boldsymbol{H}}_\alpha^{\prime\pm}) := \mathcal{R}_{\mp\pi/2}(\tilde{\boldsymbol{E}}_\alpha^{\pm}, \tilde{\boldsymbol{H}}_\alpha^{\pm})$. The 0th-order fields are written as $\sum_{\alpha=1,2} t'_\alpha(\tilde{\boldsymbol{E}}_\alpha^{\prime+}, \tilde{\boldsymbol{H}}_\alpha^{\prime+})$ in $z \geq 0$, and $(\tilde{\boldsymbol{E}}'_{\mathrm{in}}, \tilde{\boldsymbol{H}}'_{\mathrm{in}}) + \sum_{\alpha=1,2} r'_\alpha(\tilde{\boldsymbol{E}}_\alpha^{\prime-}, \tilde{\boldsymbol{H}}_\alpha^{\prime-})$ in $z \leq 0$.

Now we formulate Babinet's principle for complex coefficients as follows:

Theorem 2. *The coefficients of the two problems are related as* $t_1 + t'_1 = 1$, $r_1 + r'_1 = -1$, *and* $t_2 + t'_2 = 0$, $r_2 + r'_2 = 0$.

Proof. For problem (a), the 0th-order component of the scattered field in $z \geq 0$ is given by

$$(\tilde{\boldsymbol{E}}_{\mathrm{s}0}^{+}, \tilde{\boldsymbol{H}}_{\mathrm{s}0}^{+}) = -(\tilde{\boldsymbol{E}}_1^{+}, \tilde{\boldsymbol{H}}_1^{+}) + \sum_{\alpha=1,2} t_\alpha(\tilde{\boldsymbol{E}}_\alpha^{+}, \tilde{\boldsymbol{H}}_\alpha^{+}). \tag{4.6}$$

In problem (b), the 0th-order component of $(\tilde{\boldsymbol{E}}_{\rm s}'^{+}, \tilde{\boldsymbol{H}}_{\rm s}'^{+})$ is

$$(\tilde{\boldsymbol{E}}_{\rm s0}'^{+}, \tilde{\boldsymbol{H}}_{\rm s0}'^{+}) = \sum_{\alpha=1,2} t_\alpha'(\tilde{\boldsymbol{E}}_\alpha'^{+}, \tilde{\boldsymbol{H}}_\alpha'^{+}). \tag{4.7}$$

Applying $\mathcal{R}_{-\pi/2}$ to Eq. (4.7), we have

$$(\tilde{\boldsymbol{E}}_{\rm s0}^{+}, \tilde{\boldsymbol{H}}_{\rm s0}^{+}) = -\sum_{\alpha=1,2} t_\alpha'(\tilde{\boldsymbol{E}}_\alpha^{+}, \tilde{\boldsymbol{H}}_\alpha^{+}), \tag{4.8}$$

where we use $(\boldsymbol{E}_{\rm s0}'^{+}, \boldsymbol{H}_{\rm s0}'^{+}) = \mathcal{R}_{\pi/2}(\boldsymbol{E}_{\rm s0}^{+}, \boldsymbol{H}_{\rm s0}^{+})$ and $(\boldsymbol{E}_\alpha'^{+}, \boldsymbol{H}_\alpha'^{+}) = \mathcal{R}_{-\pi/2}(\boldsymbol{E}_\alpha^{+}, \boldsymbol{H}_\alpha^{+})$. Comparing Eq. (4.8) with Eq. (4.6), we obtain $t_1 + t_1' = 1$ and $t_2 + t_2' = 0$. The remaining equations are derived from a similar discussion for $z \leq 0$. □

4.4 Self-complementary metasurfaces

For a metasurface with a surface impedance $Z_{\rm surf}$, we can create the complementary metasurface with $Z_{\rm surf}' = {Z_0}^2/(4Z_{\rm surf})$. This operation is called an *impedance inversion about* $Z_0/2$. Two metasurfaces are congruent if one can be transformed into the other by a combination of translations, rotations and reflections. When a metasurface is congruent to its complementary one, we say that it is *self-complementary*. We emphasize that the self-complementarity is not the same as the point-group symmetry. Several examples of self-complementary metasurfaces are shown in Fig. 4.2.

For a left circularly polarized incident wave, we define $t_{\rm LL} := t_1$, $t_{\rm RL} := t_2$, and $r_{\rm RL} := r_1$, $r_{\rm LL} := r_2$. We also use $t_{\rm RR} := t_1$, $t_{\rm LR} := t_2$, and $r_{\rm LR} := r_1$, $r_{\rm RR} := r_2$ for a right circularly polarized incident wave. From reciprocity and the mirror symmetry of a metasurface with respect to $z = 0$, the following theorem is derived.

Theorem 3. *In the case of normal incidence of a circularly polarized plane wave onto a metasurface,* $t_{\rm RR} = t_{\rm LL}$ *and* $r_{\rm LR} = r_{\rm RL}$ *are satisfied.*

Proof. We consider two situations. In the first, the incident wave is a left circularly polarized wave $(\tilde{\boldsymbol{E}}_{\rm in}, \tilde{\boldsymbol{H}}_{\rm in}) = (\check{E}_0\boldsymbol{e}_+, -{\rm i}\check{H}_0\boldsymbol{e}_+){\rm e}^{{\rm i}k_0 z}$ from $z \leq 0$, where $\check{H}_0 = \check{E}_0/Z_0$ and $\boldsymbol{e}_\pm := (\boldsymbol{e}_x \pm {\rm i}\boldsymbol{e}_y)/\sqrt{2}$ with unit vectors $\boldsymbol{e}_x$ and $\boldsymbol{e}_y$ along x and y axes. The total field is represented by $(\tilde{\boldsymbol{E}}_{\rm f}, \tilde{\boldsymbol{H}}_{\rm f})$. In the second situation, an incident wave from $z \geq 0$ is $(\tilde{\boldsymbol{E}}_{\rm in}, \tilde{\boldsymbol{H}}_{\rm in}) = (\check{E}_0\boldsymbol{e}_-, {\rm i}\check{H}_0\boldsymbol{e}_-){\rm e}^{-{\rm i}k_0 z}$, and the total field is denoted by $(\tilde{\boldsymbol{E}}_{\rm b}, \tilde{\boldsymbol{H}}_{\rm b})$. If we perform the coordinate transformation $z \to -z$, the second situation can be

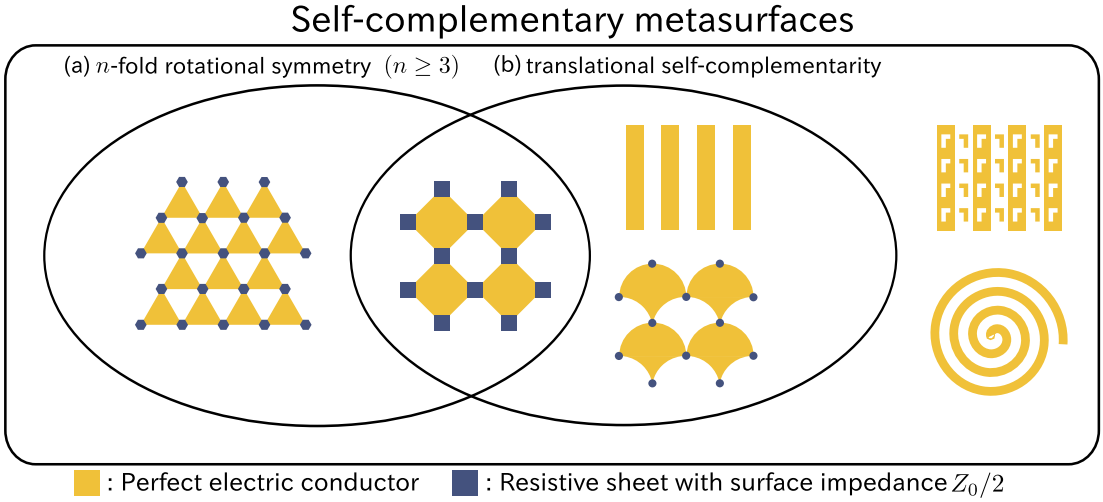

Figure 4.2: Examples of self-complementary metasurfaces - The class of self-complementary metasurfaces includes two specific subclasses with (a) n-fold rotational symmetry ($n \geq 3$) and (b) translational self-complementarity.

transformed to the scattering problem for a right circularly polarized incident wave from $z \leq 0$, because of the symmetry between the front and back of the metasurface. Then, t_1 of the second situation is equivalent to t_{RR}.

We represent the unit cell on $z = 0$ by U, and consider $V = U \times [h/2, h/2]$ with $h > 0$. For the normal incidence, we can impose periodic boundary conditions on two pairs of opposite faces of $\partial U \times [h/2, h/2]$. From the Lorentz reciprocity theorem [152]

$$\int_{\partial V} (\tilde{\boldsymbol{E}}_{\mathrm{f}} \times \tilde{\boldsymbol{H}}_{\mathrm{b}} - \tilde{\boldsymbol{E}}_{\mathrm{b}} \times \tilde{\boldsymbol{H}}_{\mathrm{f}}) \cdot \mathrm{d}\boldsymbol{S} = 0 \tag{4.9}$$

and $\boldsymbol{e}_+ \times \boldsymbol{e}_- = -\mathrm{i}\boldsymbol{e}_{\mathrm{z}}$, we obtain $t_{\mathrm{RR}} = t_{\mathrm{LL}}$. Because electric fields are continuous on $z = 0$, $1 + r_{\mathrm{LR}} = t_{\mathrm{RR}}$ and $1 + r_{\mathrm{RL}} = t_{\mathrm{LL}}$ are satisfied. Then, $r_{\mathrm{LR}} = r_{\mathrm{RL}}$ is proved. □

By using Theorems 2 and 3, we can arrive at the following theorem.

Theorem 4. *In the case of normal incidence of a circularly polarized plane wave onto a self-complementary metasurface,* $t_{\mathrm{RR}} = t_{\mathrm{LL}} = 1/2$ *and* $r_{\mathrm{LR}} = r_{\mathrm{RL}} = -1/2$ *are satisfied.*

Proof. This situation is regarded as problem (a) shown in Fig. 4.1. Because the metasurface is self-complementary, its complement returns to the original metasurface by the finite numbers of reflections. The product of these operations is denoted by $\mathcal{X}$. Problem (b) related to problem (a) through Theorem 1 is considered. Applying $\mathcal{X}$ to all fields and structures of problem (b), we have problem (c) [See Fig.4.3]. Now, we

consider the two cases where even and odd numbers of the reflections are involved in $\mathcal{X}$. In the even case, $(\tilde{\boldsymbol{E}}_{\rm in}, \tilde{\boldsymbol{H}}_{\rm in})$ is an eigenmode for $\mathcal{X}$. Therefore, problem (c) is identical to problem (a) except for the total phase, and $t_1' = t_1$ is satisfied, where the transmission coefficient t_1' of problem (b) is defined in Sec. 4.3. In the case of odd reflections, the polarization is changed by $\mathcal{X}$ (for example, from LCP to RCP), but Theorem 3 assures $t_1' = t_1$. Finally, we obtain $t_1' = t_1 = 1/2$ from Theorem 2 for both cases. □

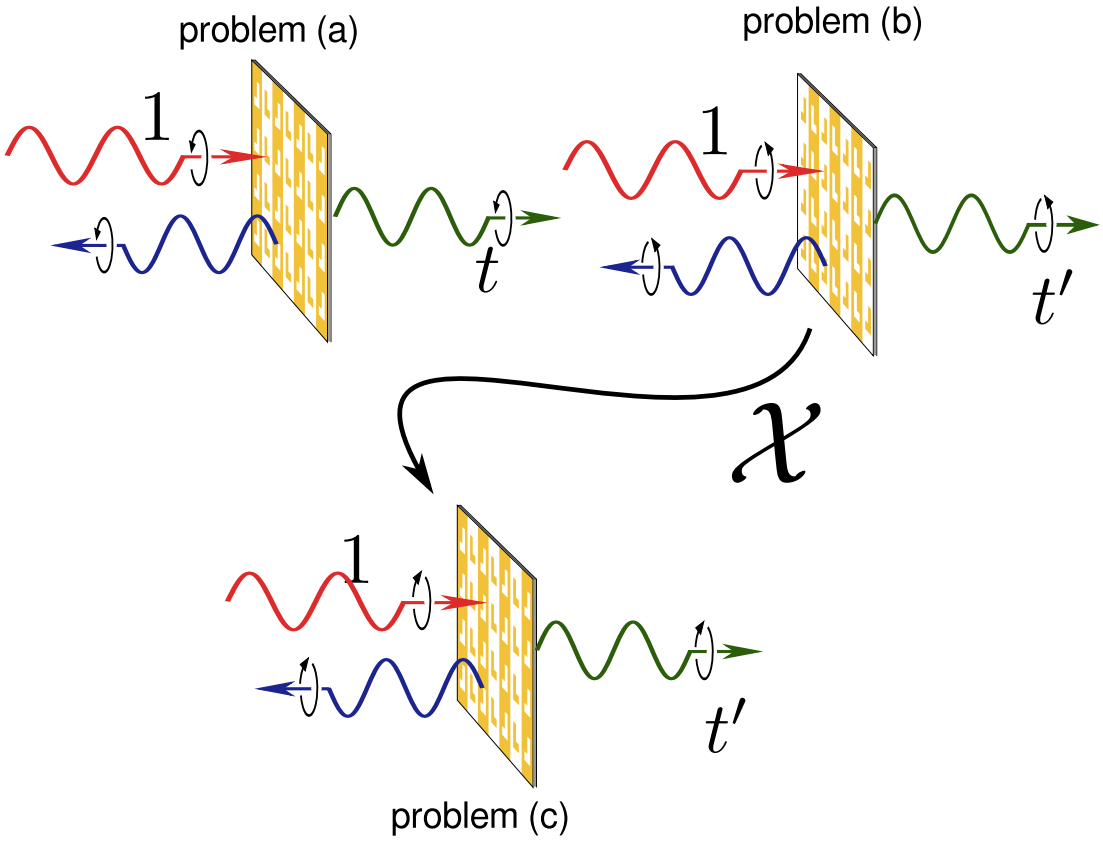

Figure 4.3: Proof for normal incidence - Under χ, problem (b) is transformed to problem (c) which is the same problem (a) without the total phase.

We note that the frequency-independent transmission of self-complementary metasurfaces is valid in the high-frequency range with diffraction. In the following, we consider subclasses of self-complementary metasurfaces shown in Fig. 4.2.

If a metasurface has rotational symmetry in addition to self-complementarity [see Fig. 4.2(a)], we have the following theorem.

4. FREQUENCY-INDEPENDENT RESPONSE OF SELF-COMPLEMENTARY METASURFACES

Theorem 5. *For normal incidence of a plane wave with an arbitrary polarization onto a self-complementary metasurface with n-fold rotational symmetry* ($n \geq 3$)*,* $t_1 = 1/2$*,* $r_1 = -1/2$ *and* $t_2 = 0$*,* $r_2 = 0$ *are satisfied. Half the incident power is absorbed by the metasurface in the frequency range without diffraction.*

Proof. We consider two incident waves in $z \leq 0$: $(\tilde{\boldsymbol{E}}_{\rm in}^{\rm L}, \tilde{\boldsymbol{H}}_{\rm in}^{\rm L}) = (\check{E}_0 \boldsymbol{e}_+, -\mathrm{i}\check{H}_0 \boldsymbol{e}_+)\mathrm{e}^{\mathrm{i}k_0 z}$ and $(\tilde{\boldsymbol{E}}_{\rm in}^{\rm R}, \tilde{\boldsymbol{H}}_{\rm in}^{\rm R}) = (\check{E}_0 \boldsymbol{e}_-, \mathrm{i}\check{H}_0 \boldsymbol{e}_-)\mathrm{e}^{\mathrm{i}k_0 z}$. Here, we define $(\tilde{\boldsymbol{E}}_\alpha^{+,\beta}, \tilde{\boldsymbol{H}}_\alpha^{+,\beta})$ as $(\tilde{\boldsymbol{E}}_\alpha^{+}, \tilde{\boldsymbol{H}}_\alpha^{+})$ for an incident wave with polarization β. We adjust the phase of $(\tilde{\boldsymbol{E}}_2^{+}, \tilde{\boldsymbol{H}}_2^{+})$ so as to satisfy $(\tilde{\boldsymbol{E}}_2^{+,\mathrm{R}}, \tilde{\boldsymbol{H}}_2^{+,\mathrm{R}}) = (\tilde{\boldsymbol{E}}_1^{+,\mathrm{L}}, \tilde{\boldsymbol{H}}_1^{+,\mathrm{L}})$ and $(\tilde{\boldsymbol{E}}_2^{+,\mathrm{L}}, \tilde{\boldsymbol{H}}_2^{+,\mathrm{L}}) = (\tilde{\boldsymbol{E}}_1^{+,\mathrm{R}}, \tilde{\boldsymbol{H}}_1^{+,\mathrm{R}})$ on $z = 0$, for each incident wave. In this situation, we can define a complex transmittance matrix

$$\tau = \begin{bmatrix} t_{\rm LL} & t_{\rm LR} \\ t_{\rm RL} & t_{\rm RR} \end{bmatrix}. \tag{4.10}$$

For a circularly polarized basis, a rotation by $2\pi/n$ about z axis is represented by

$$P := \begin{bmatrix} \mathrm{e}^{-\mathrm{i}\frac{2\pi}{n}} & 0 \\ 0 & \mathrm{e}^{\mathrm{i}\frac{2\pi}{n}} \end{bmatrix}. \tag{4.11}$$

Because of n-fold symmetry, $P^{-1}\tau P = \tau$ is satisfied, and then $t_{\rm RL} = t_{\rm LR} = 0$. Therefore, we obtain

$$\tau = \begin{bmatrix} \frac{1}{2} & 0 \\ 0 & \frac{1}{2} \end{bmatrix}, \tag{4.12}$$

from Theorem 4. Because τ is proportional to the identity matrix, $t_1 = 1/2$, $r_1 = -1/2$ and $t_2 = 0$, $r_2 = 0$ are satisfied for an incident plane wave with an arbitrary polarization.

In the frequency range without diffraction, the Fourier components of $(\tilde{\boldsymbol{E}}_{\rm s}^{\pm}, \tilde{\boldsymbol{H}}_{\rm s}^{\pm})$ with $(p, q) \neq 0$ are evanescent waves. For evanescent waves, the real part of the z-component of Poynting vectors is zero; therefore, they do not carry energy out of $z = 0$. The remaining power $A = 1 - |t_1|^2 - |r_1|^2 = 1/2$ is absorbed in the metasurface. □

From Theorem 5, we find that the metasurface can absorb total incident energy as follows:

Theorem 6. *If we excite a self-complementary metasurface with n-fold rotational symmetry* ($n \geq 3$) *by two in-phase plane waves* $(\check{\boldsymbol{E}}_0, \check{\boldsymbol{H}}_0)\mathrm{e}^{\mathrm{i}k_0 z}$ *from* $z \leq 0$ *and* $(\check{\boldsymbol{E}}_0, -\check{\boldsymbol{H}}_0)\mathrm{e}^{-\mathrm{i}k_0 z}$ *from* $z \geq 0$ *with an arbitrary polarization* $(\check{\boldsymbol{E}}_0, \check{\boldsymbol{H}}_0)$*, the incident power is perfectly absorbed in the frequency range without diffraction.*

Proof. In the case of one excitation $(\check{\boldsymbol{E}}_0, \check{\boldsymbol{H}}_0)\mathrm{e}^{\mathrm{i}k_0 z}$ from $z \leq 0$, half of the power is absorbed in the frequency range without diffraction. If we excite from both sides in phase, the electric field is doubled, and then absorption is quadrupled. Therefore, all of the incident power is absorbed. □

If we excite the above self-complementary metasurface by two antiphase plane waves, there is no absorption. This is because boundary conditions at $z = 0$ are already satisfied without induced currents and charges. The perfect absorption is only realized when two beams have the correct relative phase and amplitude. This function is referred to as coherent perfect absorption [153, 154]. We note that self-complementarity is not a necessary condition for the frequency-independent response described in Theorem 7 because a similar frequency-independent response can be seen in other systems, such as percolated metallic films [155–161] and two identical lamellar gratings [162].

There is another interesting class of self-complementary metasurfaces. If a metasurface returns to the original one by just a translation after the impedance inversion about $Z_0/2$, we say that it has *translational self-complementarity* [see Fig. 4.2(b)]. This subclass of self-complementary metasurfaces has the following property.

Theorem 7. *In the case of an oblique incidence of a circularly polarized plane wave onto a metasurface with translational self-complementarity,* $t_{\mathrm{RR}} = t_{\mathrm{LL}} = 1/2$ *and* $r_{\mathrm{LR}} = r_{\mathrm{RL}} = -1/2$ *are satisfied.*

Proof. We regard this situation as problem (a) shown in Fig. 4.1. The metasurface returns to the original position by a translation $\mathcal{T}$ together with the impedance inversion. Problem (b) can be related to problem (a) through Theorem 1. We introduce problem (c) in which the incident wave and the metasurface of problem (b) are translated by $\mathcal{T}$ [See Fig.4.4]. From the definition of $\mathcal{T}$, the metasurface of problem (c) is the same as that in problem (a). The incident field of problem (c) is written as $\mathcal{T}\mathcal{R}_{-\pi/2}(\tilde{\boldsymbol{E}}_{\mathrm{in}}, \tilde{\boldsymbol{H}}_{\mathrm{in}})$. Because $(\tilde{\boldsymbol{E}}_{\mathrm{in}}, \tilde{\boldsymbol{H}}_{\mathrm{in}})$ is an eigenmode for $\mathcal{T}\mathcal{R}_{-\pi/2}$, the incident wave of problem (c) is identical to that of problem (a) except for the total phase. In this way, $t'_1 = t_1$ and $r'_1 = r_1$ are confirmed. From Theorem 2, we have $t'_1 = t_1 = 1/2$ and $r'_1 = r_1 = -1/2$. □

This theorem shows that self-complementary metasurfaces can be used as beam splitters. The extension for general diffraction orders is discussed in Appendix A.3.

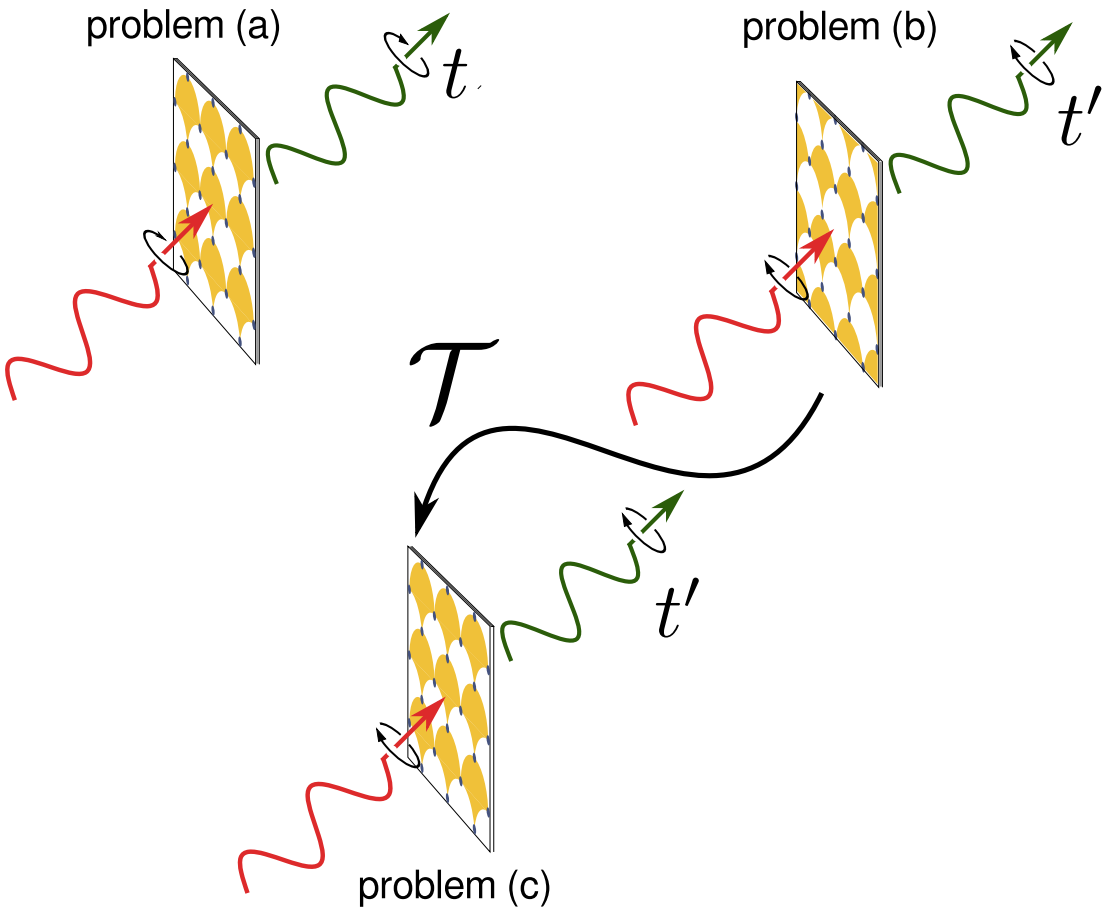

Figure 4.4: Proof for an oblique incidence - Under $\mathcal{T}$, problem (b) is transformed to problem (c) which is the same problem (a) without the total phase.

4.5 Examples: checkerboard metasurfaces

In this section, we apply the current theory for checkerboard metasurfaces [149, 150, 163–165] and confirm its validity by simulations. First, we consider an ideal checkerboard metasurface shown in Fig. 4.5(a). It is expected that the ideal checkerboard metasurface should exhibit a frequency-independent response due to its self-complementarity. However, it is known that the ideal checkerboard metasurface cannot be realized. This is explained as follows [150]. The electromagnetic response of the checkerboard metasurface drastically changes depending on whether the square metals are connected or not. The transmittance and reflectance do not converge when the structure approaches the ideal checkerboard metasurface. Furthermore, it has also been reported that there is an instability in numerical calculations for the ideal checkerboard metasurface, and the checkerboard metasurfaces exhibit percolation effects near the ideal checkerboard metasurface [164].

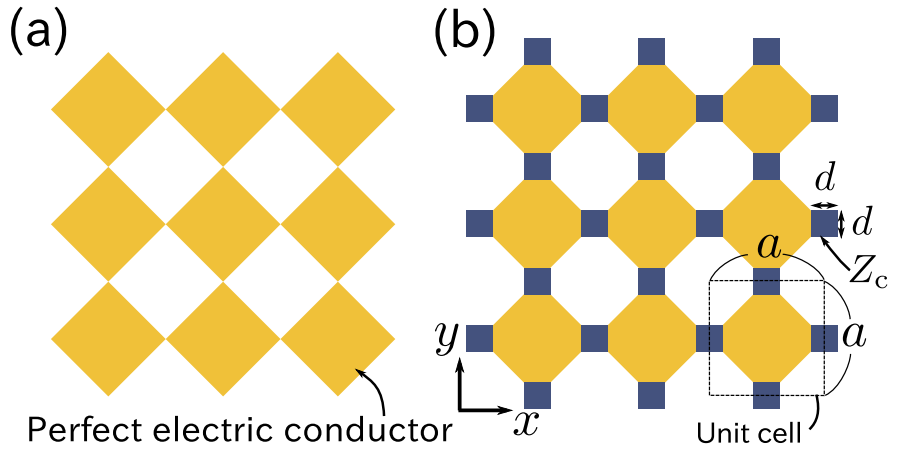

Figure 4.5: Two checkerboards - (a) Ideal checkerboard metasurface (b) Resistive checkerboard metasurface

By using our theory, we can give another explanation without relying on asymptotic behaviors. From Theorem 5, the power transmission $T = |t_1|^2$ and reflection $R = |r_1|^2$ should satisfy $T = R = 1/4$ for the ideal checkerboard metasurface with 4-fold rotational symmetry. However, energy conservation means $T + R = 1$ in the frequency range without diffraction, because there is no absorption in the perfect checkerboard metasurface. This contradiction implies that the ideal checkerboard metasurface is unphysical.

The above explanation gives us another insight: we may realize the frequency-independent response of a checkerboard metasurface if resistive elements are introduced. We replace the singular contacts with tiny resistive sheets with a surface impedance Z_c and obtain *a resistive checkerboard metasurface* shown in Fig. 4.5(b). When $Z_c = Z_0/2$ is satisfied, the resistive checkerboard metasurface is self-complementary and is expected to exhibit a frequency-independent response.

For confirmation of our theory, we calculate the electromagnetic response of resistive checkerboard metasurfaces on $z = 0$ by a commercial finite-element method solver (ANSOFT HFSS). In the simulation, normal incident x-polarized plane wave is injected onto resistive checkerboard metasurfaces with $d/a = 0.2$, where a and d are the side length of the square unit cell and that of impedance sheet, respectively. By imposing periodic boundaries on four sides, the electromagnetic fields in the unit cell are calculated for $Z_c = 0$, $Z_0/2$, and ∞. We take into account diffracted modes with $\{(p, q, \alpha)| -1 \le p \le 1,\ -1 \le q \le 1,\ \alpha = 1, 2\}$ (18 modes), where (p, q) and α are defined in Sec. 4.3 and Appendix A.2.

Figure 4.6(a) displays the spectra of power transmission $|t_1|^2$ for resistive checkerboard metasurfaces with $Z_c = 0$, $Z_0/2$, and ∞. The frequency in the horizontal axis is normalized by $f_0 := c_0/a$ (c_0 is the speed of light in a vacuum). Above the frequency f_0, diffracted waves can propagate in free space. The checkerboard metasurfaces with $Z_c = 0$ and ∞ resonate at the same frequency $f/f_0 = 0.89$. Babinet's principle assures that the sum of these transmission spectra equals 1 under the diffraction frequency[1], because the checkerboard metasurface with $Z_c = \infty$ is complementary to that with $Z_c = 0$. This assure that the transmission at cross points of the two curves with $Z_c = 0$ and ∞ must be 0.5 for $f \le f_0$. For the resistive checkerboard metasurface with $Z_c = Z_0/2$, transmission equals to 1/4 independent of frequency, even when diffraction takes place ($f \ge f_0$). This constant response seems very strange, because metasurfaces made from metal usually exhibit a resonant response, but it can be explained by Theorem 5. In addition to the magnitude of transmission, we also confirm the phase of t_1. For $0 < f/f_0 \le 1.25$, we have $|\operatorname{Im}[t_1]/\operatorname{Re}[t_1]| < 1.2 \times 10^{-2}$. This result shows $t_1 = 1/2$ expected by Theorem 5.

[1]Babinet's principle leads to $t_1 + t_1' = 1$. Energy conservation law is $|t_1|^2 + |r_1|^2 = 1$ for $f \le f_0$. Due to $r_1 = t_1 - 1 = t_1'$, $|t_1|^2 + |t_1'|^2 = 1$ is satisfied.

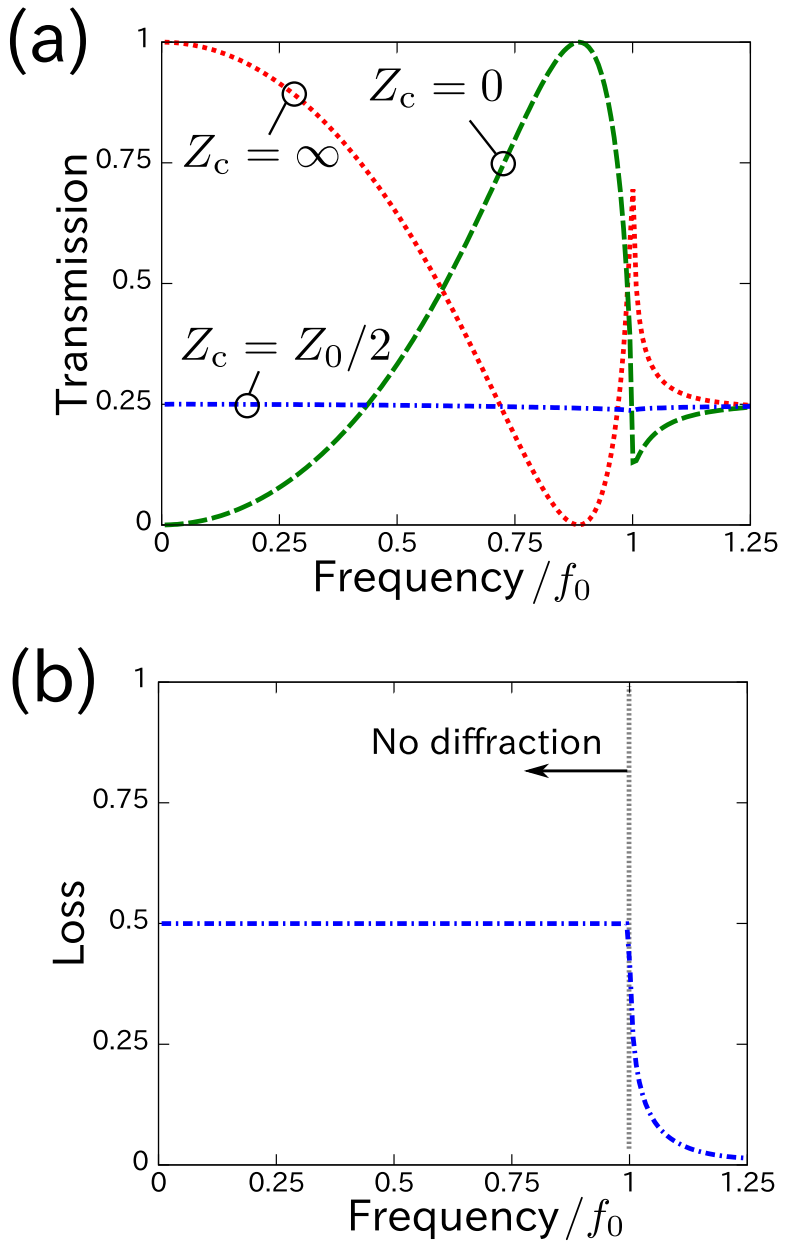

Figure 4.6: Simulation results for the normal incidence - (a) Power transmission and loss spectra for normally incident x-polarized plane waves entering into resistive checkerboard metasurfaces with $d/a = 0.2$. (b) Power transmission spectra for resistive checkerboard metasurfaces with $Z_c = 0$, $Z_0/2$, and ∞. The right graph shows the loss spectrum calculated for the self-complementary resistive checkerboard metasurface with $Z_c = Z_0/2$.

Figure 4.6(b) shows the spectrum of energy loss for the resistive checkerboard metasurface with $Z_c = Z_0/2$. The loss is calculated by integration of the Poynting vector over the resistive sheets. In the frequency range $f \leq f_0$, we can see that half the incident power is absorbed by the metasurface, while the electromagnetic energy is converted to diffracted modes under the diffraction frequency[1]. These results agree with Theorem 5, and coherent perfect absorption can be realized for the two-side excitations. Perfect absorption occurs for any d/a. The resistive checkerboard metasurface with tiny resistive sheets can absorb energy in very small regions. This property can be useful for the enhancement of non-linearity of resistance.

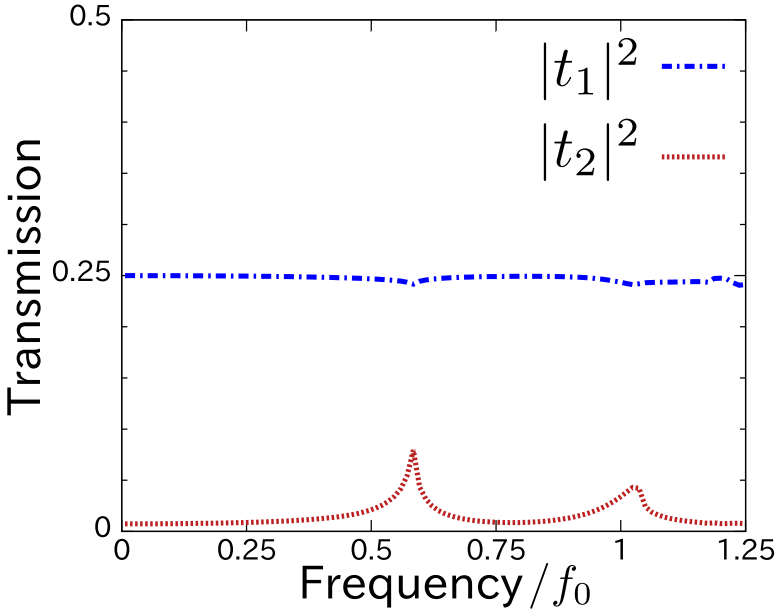

Figure 4.7: Simulation result for an oblique incidence - The calculated spectra of $|t_1|^2$ and $|t_2|^2$ for an oblique incident circularly polarized plane wave entering into the resistive checkerboard metasurfaces with $Z_c = Z_0/2$ and $d/a = 0.2$. The incident wave has a wave vector $\boldsymbol{k}_0 = (k_0 \sin\theta, 0, k_0 \cos\theta)$ with $\theta = \pi/4$. In these simulations, the frequencies are normalized by $f_0 = c_0/a$.

The resistive checkerboard metasurface with $Z_c = Z_0/2$ also has translational self-complementarity. Then, it exhibits frequency-independent response for oblique incident waves. By using HFSS, we calculated the response of the resistive checkerboard metasurfaces with $Z_c = Z_0/2$ for an oblique incidence of a circularly polarized plane wave with incident angle 45° in the xz-plane. In this case, we obtain the same transmission

[1] We checked the validity of energy conservation law in $f \geq f_0$ by adding S parameters and the loss.

spectra for the right and left circularly polarized incident waves [1]. The obtained spectra of $|t_1|^2$ and $|t_2|^2$ are shown in Fig. 4.7. We can see that $|t_1|^2 = 1/4$, while $|t_2|^2$ has two non-zero resonant peaks at $f/f_0 = 0.58$ and 1.02. Slight changes of $|t_1|^2$ are considered numerical errors. For $0 < f/f_0 \leq 1.25$, we have $|\operatorname{Im}[t_1]/\operatorname{Re}[t_1]| < 1.7 \times 10^{-2}$. This result supports the validity of Theorem 7. The two peaks of $|t_2|^2$ are originated from the interaction between lattice sites. Periodic systems exhibit such singular behaviors when a diffracted beam grazes to the plane $z = 0$ (Rayleigh condition), [3] and in our system, the Rayleigh condition is satisfied at $f/f_0 = 1$ and $f/f_0 = 2 - \sqrt{2} = 0.586$. These frequencies correspond to the peaks shown in the graph. Then, $|t_2|^2$ shows resonant behaviors near these frequencies, while $|t_1|^2$ should be constant because of translational self-complementarity.

4.6 Discussion

In order to increase the absorption, we consider the multilayer composed of self-complementary metasurfaces with n-fold ($n \geq 3$) rotational symmetry below the diffraction frequency. These metasurfaces are placed on $z = 0,\ l,\ 2l,\ 3l,\ \cdots$. For normal incidence from $z < 0$, the total complex reflection coefficient is denoted by r_∞. We can calculate r_∞ from the following equation:

$$\begin{aligned} r_\infty &= -\frac{1}{2} + \frac{1}{4}\alpha\left[1 + \frac{\alpha}{2} + \left(\frac{\alpha}{2}\right)^2 + \cdots\right] \\ &= -\frac{1}{2} + \frac{\alpha}{4 - 2\alpha}, \end{aligned} \tag{4.13}$$

where $\alpha = r_\infty \mathrm{e}^{2\mathrm{i}kl}$. Here, we define $\varphi = 2kl$. The calculated absorption $A(\varphi) = 1 - |r_\infty|^2$ is shown in Fig 4.8. Minimum and maximum of absorption are $A(0) = 1 - (-1 + \sqrt{5})^2/4 = 0.618$, and $A(\pi) = 1 - (3 - \sqrt{5})^2/4 = 0.854$, respectively. For $\varphi = \pi$, multiple reflections are destructively interfered, then the reflection is minimized and the absorption is maximized. Although the absorption is increased by using multilayer, the frequency-independent response is vanished by the interference effects.

So far, we consider only metasurfaces without substrates. If substrates are introduced, Babinet's principle will not be valid. This is because Babinet's principle is based

[1] The resistive checkerboard metasurfaces on $z = 0$ are invariant when we perform the rotation by 180° about x axis after the mirror reflection $z \to -z$. Because the helicity of an incident wave is changed under this operation, $t_{\mathrm{RR}} = t_{\mathrm{LL}}$ and $|t_{\mathrm{RL}}| = |t_{\mathrm{LR}}|$ are derived.

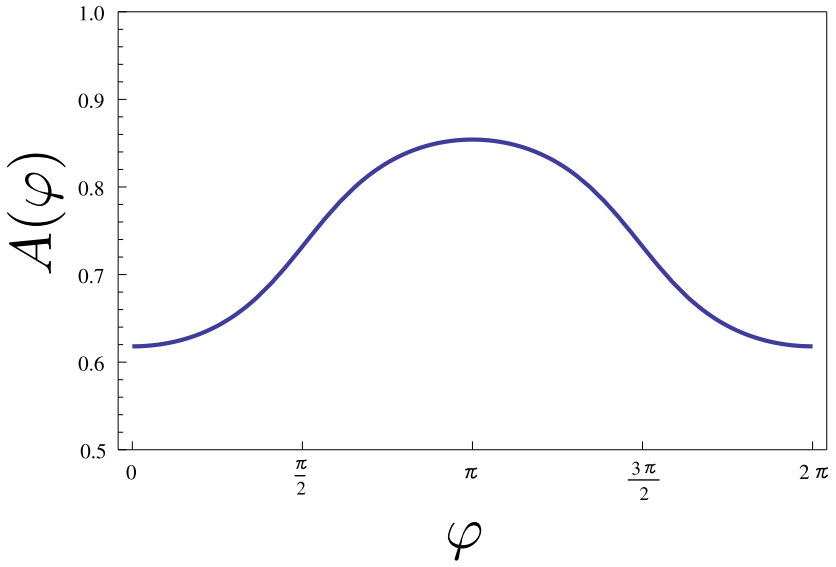

Figure 4.8: Absorption by multilayer self-complementary metasurfaces - The absorption is calculated for multilayer self-complementary metasurfaces with n-fold ($n \geq 3$) rotational symmetry below the diffraction frequency.

on the mirror symmetry with respect to $z = 0$. It is empirically known that Babinet's principle can be approximately valid in low frequency range for a metasurface with a substrate [166]. Therefore, it is expect that frequency-independent response of self-complementary metasurfaces can be realized approximately. However, the impedance inversion $Z_{\text{surf}}Z'_{\text{surf}} = (Z_0/2)^2$ should be modified.

Finally, we discuss the extension possibility to the acoustic waves. Scalar Babinet's principle is reviewed in Appendix A.4. The theorem correspond to Theorem 1 is given in Appendix A.4.2. In this theory, two boundary (soft and hard) conditions are used. Babinet's principle relates scattering problems of a hard thin material, and the same-shape aperture in a soft screen. Under the corresponding structural inversion, no surface is invariant. Therefore, it may be difficult to realize the self-complementary acoustic surfaces. Further studies are needed for acoustic theory.

4.7 Summary

In this chapter, we analyzed theoretically electromagnetic plane-wave scattering by self-complementary metasurfaces. In order to study the response of self-complementary

metasurfaces, we first described the electromagnetic duality and Babinet's principle with resistive elements. Next, by applying Babinet's principle, we obtained the relation of scattering coefficients for a metasurface and its complement. Using this result, we revealed that the frequency-independent transmission and reflection are realized for self-complementary metasurfaces. In the case of normal incidence of a circularly polarized plane wave onto a self-complementary metasurface, complex transmission and reflection coefficients of the 0th-order diffraction must be $1/2$ and $-1/2$, respectively. If a self-complementary metasurface additionally has n-fold rotational symmetry ($n \geq 3$), the above result is valid for normal incidence of a plane wave with an arbitrary polarization. Furthermore, we found that this type of metasurface acts as a coherent perfect absorber. We also studied metasurfaces with translational self-complementarity. For an oblique incidence of a circularly polarized plane wave to a metasurface with translational self-complementarity, complex transmission and reflection coefficients of the 0th diffraction order also equal to $1/2$ and $-1/2$, respectively. These results are confirmed by numerical simulations for resistive checkerboard metasurfaces.

Chapter 5

Conclusions and future work

This research studied the characteristics of metasurfaces in terms of lattice symmetry and self-complementarity. In the following sections, conclusions are presented and future work is discussed.

5.1 Conclusion

In Chap. 2, we investigated tight-binding models in circuit theory. We first presented the circuit-theoretical framework by using bra-ket notation, which enables us to calculate the response of circuits using a method analogous to quantum mechanics, which is familiar to physicists. Next, we proposed simple circuit models, which are described by similar equations to quantum tight-binding models. These models can be implemented as metamaterials. Finally we looked for the phenomena caused by lattice symmetry. In particular, we systematically discussed flat-band formation in circuits and showed that flat bands are formed in circuits with the symmetry of Lieb-, Tasaki-, and Mielke-type lattices. These flat bands lead to slow group velocities for all wave vectors.

In Chap. 3, we experimentally confirmed a flat band formation and studied metallic kagomé lattices. First, we theoretically showed that it has flat bands, which had never been previously demonstrated experimentally in electromagnetism. Next, we fabricated a sample by etching and experimented with it using terahertz time-domain spectroscopy. Both the second and highest bands were observed as transmission minima. The latter corresponds to the flat band. The flatness of the bands can be applied to frequency filters that are independent of the incident angles. Slowing down the group

velocity of a photon in the flat band also leads to increased interactions with matter. Therefore, such a metallic structure can also be applied to sensors.

In Chap. 4, we investigated the general properties of self-complementary metasurfaces. Under impedance inversion, which is the extension of exchanging apertures with metals, self-complementary metasurfaces are invariant except for translations and rotations. First, we discussed Babinet's principle with resistive elements. Next, we used it to prove that frequency-independent transmission occurs for a normal incidence of circularly polarized plane waves to a self-complementary metasurface even if diffraction occurs. This means that the concept of self-complementarity can be utilized for realizing broad band metamaterials. Second, we investigated the self-complementary metasurfaces with n-fold rotational symmetry ($n \geq 3$) and learned that they exhibit frequency-independent transmission for the normal incidence of a plane wave with arbitrary polarization. Half of the incident power is absorbed by such metasurfaces. If we excite the metasurface from the double side in the phase, this class of metasurfaces can act as coherent perfect absorbers. Third, we studied metasurfaces that are self-complementary compatible with translation and revealed that the complex amplitudes in the transmission are also 1/2 for the oblique incidence of circularly polarized plane waves to metasurfaces with translational self-complementarity. This property is applicable to beam splitters. Finally, we investigated the controversy of checkerboard metasurfaces: whether they exhibit frequency-independent responses. Using our theory, we shed new light on this problem. Replacing singular contacts with resistive pads, we demonstrated frequency-independent responses by numerical simulation. We also identified why ideal checkerboard metasurfaces show chaotic behavior. Such ideal structures contradict energy conservation laws, so they cannot be realized.

5.2 Future work

In Chaps. 2 and 3, we used a simple-circuit theoretical model and experimentally confirmed its validity. However, simple models have not been derived rigorously from concrete structures using a general circuit-theoretical method. This problem can be resolved using the partial element equivalent circuit (PEEC) method with appropriate basic functions.

In Chap. 3, we confirmed the flat band in the frequency domain. The measurement gave the wavepacket's group velocity through $\mathrm{d}\omega/\mathrm{d}\boldsymbol{k}$. However, this is an indirect method to study wavepacket dynamics. Standard terahertz time-domain spectroscopy is not appropriate for investigating confinement in the time-domain because the terahertz pulse has a broad spectrum. Time-domain measurements using a narrower-spectrum source should be performed to evaluate the wavepacket dynamics. Such an experiment can be performed when we use a pulse generator, at least, in the microwave regime [113].

Note that since flat bands can be realized in the optical regime, their demonstration and application should be considered. In the optical regime, the loss of metals must also be considered. Electron-beam lithography can be utilized to fabricate samples.

Multiphoton correlation effects in kagomé lattices are also important in terms of fundamental physics and should be studied. This can be realized by nonlinearity in high intensity field excitation.

In Chap. 4, we developed the theory of plane-wave scattering for self-complementary metasurfaces. Self-complementarity is a sufficient condition, but it is not a necessary condition for frequency-independent responses. For example, frequency-independent electromagnetic responses are also observed in percolated systems. The necessary conditions should be theoretically investigated in the future.

Experimental confirmation of frequency-independent responses should also be performed. Although it is hard to use perfect metals and tunable resistive sheets in the optical regime, experiments are possible in the terahertz and microwave regimes. My coworker (Mr. Urade) will report the experimental verification in the terahertz range. For the terahertz regime, a standard photolithography technique is applicable to fabricate samples on a substrate. Typically, Si is used for the substrate, but this invalidates the standard Babinet's principle because the mirror symmetry is broken with respect to the interface. For metallic structures on the substrate, a controversy continues over which value should be averaged, permittivity or the refractive index [166, 167]. So far, since no theoretical framework exists that systematically treats the substrate effect, a comprehensive theory should be formulated.

Furthermore, we must reconsider the sufficient conditions for Babinet's principle. Its extensions for metasurfaces with two dielectric components, ε_1 and ε_2, have been developed by Marqués's group [168, 169]. Since such a metasurface has only dielectric

components, it is applicable to the optical regime. In this theory, ε_1 is exchanged with ε_2. This replacement does not agree with the impedance inversion by $Z_{\mathrm{surf}}Z'_{\mathrm{surf}} = (Z_0/2)^2$, but Marqués showed that a similar relation to Babinet's principle can be formulated [168]. This suggests the realization of self-complementary metasurfaces in optical regimes.

We should also consider Babinet's principle beyond electromagnetism. As discussed in Chap. 4, Babinet's principle for acoustic waves is somewhat different from electromagnetic ones. In electromagnetism, electromagnetic duality plays an important role in Babinet's principle, but acoustic systems don't have electromagnetic duality. This poses a naive question: "What is the physical origin of Babinet's principle?" Its true physical meaning should be revealed by resolving these problems.

Appendix A

Supplementary materials for Chap. 4

A.1 The relation between totally transmitted and totally reflected waves

We consider an incident wave $(\boldsymbol{E}_{\rm in}, \boldsymbol{H}_{\rm in})$ in $z \leq 0$ and the totally transmitted wave $(\boldsymbol{E}_{\rm TT}, \boldsymbol{H}_{\rm TT})$ in $z \geq 0$. If there is a surface made of PEC on $z = 0$, the incident wave is totally reflected. This totally reflected wave is denoted by $(\boldsymbol{E}_{\rm TR}, \boldsymbol{H}_{\rm TR})$. We show that $(\boldsymbol{E}_{\rm TR}, \boldsymbol{H}_{\rm TR})$ can be represented by $(\boldsymbol{E}_{\rm TT}, \boldsymbol{H}_{\rm TT})$ like the method of images used in electrostatics. We define $\mathcal{M}$ as the mirror reflection with respect to $z = 0$. If we assume

$$(\boldsymbol{E}_{\rm TR}, \boldsymbol{H}_{\rm TR}) = -(\mathcal{M}\boldsymbol{E}_{\rm TT}, \mathcal{M}\boldsymbol{H}_{\rm TT}), \tag{A.1}$$

the boundary condition of perfect electric conductor is satisfied. This is because $\mathcal{P}(\boldsymbol{E}_{\rm in} + \boldsymbol{E}_{\rm TR}) = \mathcal{P}(\boldsymbol{E}_{\rm in} - \mathcal{M}\boldsymbol{E}_{\rm TT}) = 0$ for $z = 0$. Then, the definition of Eq. (A.1) is valid. Because magnetic fields are axial vectors, $\mathcal{P}\mathcal{M}\boldsymbol{H}_{\rm TT} = -\mathcal{P}\boldsymbol{H}_{\rm in}$ is satisfied on $z = 0$. From this equation and Eq. (A.1),

$$\mathcal{P}\boldsymbol{H}_{\rm TR} = \mathcal{P}\boldsymbol{H}_{\rm in} \tag{A.2}$$

is satisfied for $z = 0$.

A.2 Relation of scattering coefficients for all diffracted components

We generalize Theorem 2 to include all diffracted modes. The two problems discussed in Sec. 4.3 are considered. For $(p,q)=(0,0)$, we define $(\tilde{\boldsymbol{E}}^{+}_{pq,1},\tilde{\boldsymbol{H}}^{+}_{pq,1}) := (\tilde{\boldsymbol{E}}_{\mathrm{TT}},\tilde{\boldsymbol{H}}_{\mathrm{TT}})$ and its perpendicular polarization state $(\tilde{\boldsymbol{E}}^{+}_{pq,2},\tilde{\boldsymbol{H}}^{+}_{pq,2})$. For $(p,q)\neq(0,0)$, we also define $(\tilde{\boldsymbol{E}}^{+}_{pq,1},\tilde{\boldsymbol{H}}^{+}_{pq,1})$ and $(\tilde{\boldsymbol{E}}^{+}_{pq,2},\tilde{\boldsymbol{H}}^{+}_{pq,2})$ that are two orthogonal polarized modes with the factor $\mathrm{e}^{\mathrm{i}\underline{\boldsymbol{k}}_{pq}\cdot\boldsymbol{x}}\mathrm{e}^{\mathrm{i}k_z z}$, where $k_z=\sqrt{|\boldsymbol{k}_0|^2-|\underline{\boldsymbol{k}}_{pq}|^2}$ ($\mathrm{Im}\,k_z\geq 0$). The mirror symmetric fields of $(\tilde{\boldsymbol{E}}^{+}_{pq,\alpha},\tilde{\boldsymbol{H}}^{+}_{pq,\alpha})$ with respect to $z=0$ are denoted by $(\tilde{\boldsymbol{E}}^{-}_{pq,\alpha},\tilde{\boldsymbol{H}}^{-}_{pq,\alpha})$.

We then decompose the complex field of problem (a) in $z\geq 0$ as

$$\sum_{(p,q)\in\mathbb{Z}^2}\sum_{\alpha=1,2} t_{pq,\alpha}(\tilde{\boldsymbol{E}}^{+}_{pq,\alpha},\tilde{\boldsymbol{H}}^{+}_{pq,\alpha})$$

with complex transmission coefficients $t_{pq,\alpha}$. In $z\leq 0$, the field is given by

$$(\tilde{\boldsymbol{E}}_{\mathrm{in}},\tilde{\boldsymbol{H}}_{\mathrm{in}})+\sum_{(p,q)\in\mathbb{Z}^2}\sum_{\alpha=1,2} r_{pq,\alpha}(\tilde{\boldsymbol{E}}^{-}_{pq,\alpha},\tilde{\boldsymbol{H}}^{-}_{pq,\alpha}).$$

For problem (b), we define $(\tilde{\boldsymbol{E}}'^{\pm}_{pq,\alpha},\tilde{\boldsymbol{H}}'^{\pm}_{pq,\alpha}) := \mathcal{R}_{\mp\pi/2}(\tilde{\boldsymbol{E}}^{\pm}_{pq,\alpha},\tilde{\boldsymbol{H}}^{\pm}_{pq,\alpha})$. The fields in problem (b) are represented as follows:

$$\sum_{(p,q)\in\mathbb{Z}^2}\sum_{\alpha=1,2} t'_{pq,\alpha}(\tilde{\boldsymbol{E}}'^{+}_{pq,\alpha},\tilde{\boldsymbol{H}}'^{+}_{pq,\alpha})$$

in $z\geq 0$, and

$$(\tilde{\boldsymbol{E}}'_{\mathrm{in}},\tilde{\boldsymbol{H}}'_{\mathrm{in}})+\sum_{(p,q)\in\mathbb{Z}^2}\sum_{\alpha=1,2} r'_{pq,\alpha}(\tilde{\boldsymbol{E}}'^{-}_{pq,\alpha},\tilde{\boldsymbol{H}}'^{-}_{pq,\alpha})$$

in $z\leq 0$. Now, we can generalize Theorem 2 as follows:

Theorem 8. *$t_{00,1}+t'_{00,1}=1$, $r_{00,1}+r'_{00,1}=-1$, and $t_{pq,\alpha}+t'_{pq,\alpha}=0$, $r_{pq,\alpha}+r'_{pq,\alpha}=0$ for $(p,q,\alpha)\neq(0,0,1)$.*

The proof of Theorem 8 is similar to that of Theorem 2.

A.3 General order diffraction by metasurfaces with translational self-complementarity

We discuss the general scattering components of diffracted waves by metasurfaces with translational self-complementarity. An oblique incidence of a circularly polarized plane

wave is considered. We define $W := \{(p,q) \in \mathbb{Z}^2; |\underline{\boldsymbol{k}}_{pq}| < |\boldsymbol{k}_0|\}$. For $(p,q) \in W$, the waves with the wave vector $\underline{\boldsymbol{k}}_{pq} \pm \sqrt{{k_0}^2 - |\underline{\boldsymbol{k}}_{pq}|^2}\,\boldsymbol{e}_z$ are not evanescent but propagating plane waves. $(\tilde{\boldsymbol{E}}^+_{00,1}, \tilde{\boldsymbol{H}}^+_{00,1})$ represents the totally transmitted plane wave with circular polarization. For $(p,q) \in W$ satisfying $(p,q) \neq (0,0)$, $(\tilde{\boldsymbol{E}}^+_{pq,1}, \tilde{\boldsymbol{H}}^+_{pq,1})$ are selected to be the circularly polarized plane waves with the same helicity of $(\tilde{\boldsymbol{E}}^+_{00,1}, \tilde{\boldsymbol{H}}^+_{00,1})$. Now, Theorem 7 is extended as follows:

Theorem 9. *For the 0th-order modes, we have* $t_{00,1} = t'_{00,1} = 1/2$ *and* $r_{00,1} = r'_{00,1} = -1/2$. *For* $(p,q) \in W$ *satisfying* $(p,q) \neq (0,0)$, *we have* $t_{pq,1} = t'_{pq,1} = 0$ *and* $r_{pq,1} = r'_{pq,1} = 0$.

This theorem is proved in the same manner as Theorem 7. The latter part of this theorem shows that helicities must be converted for propagating waves with $(p,q) \neq (0,0)$ diffracted by metasurfaces with translational self-complementarity.

A.4 Babinet's principle for scalar wave

Here, we review Babinet's principle for scalar waves. At first, we show the simple derivation through Huygens-Fresnel principle. Next, another formulation without any approximation is shown.

A.4.1 Through the Kirchhoff approximation

We consider an opaque thin material placed on $z = 0$. The position of the material is expressed as A. The remaining part of $z = 0$ except for A is denoted by B. Then, A + B is the plane $z = 0$. The opaque thin material is illuminated by the incident wave $\tilde{\psi}_{\mathrm{in}}$ from $z < 0$, where $\tilde{\psi}_{\mathrm{in}}$ is defined without screen. From Kirchhoff's integral [170], the total wave $\tilde{\psi}$ in $z \geq 0$ [problem (a)] is given by

$$\tilde{\psi}(\boldsymbol{x}) = \frac{1}{4\pi} \int_B \frac{\mathrm{e}^{\mathrm{i}kR}}{R} \boldsymbol{e}_z \cdot \left[\nabla' \tilde{\psi} + \mathrm{i}k \left(1 + \frac{\mathrm{i}}{kR} \right) \frac{\boldsymbol{R}}{R} \tilde{\psi} \right] \mathrm{d}S', \tag{A.3}$$

where $\boldsymbol{R} = \boldsymbol{x} - \boldsymbol{x}'$. Now, the following Kirchhoff approximation is assumed:

1. $\tilde{\psi}$ and $\partial\tilde{\psi}/\partial z$ are 0 except for A.
2. On B, $\tilde{\psi}$ and $\partial\tilde{\psi}/\partial z$ are given by those of incident waves in the absence of any screen.

Then, the diffracted wave is given by

$$\tilde{\psi}(\boldsymbol{x}) = \frac{1}{4\pi}\int_{\mathrm{B}} \frac{\mathrm{e}^{\mathrm{i}kR}}{R}\boldsymbol{e}_z \cdot \left[\nabla'\tilde{\psi}_{\mathrm{in}} + \mathrm{i}k\left(1+\frac{\mathrm{i}}{kR}\right)\frac{\boldsymbol{R}}{R}\tilde{\psi}_{\mathrm{in}}\right]\mathrm{d}S'. \tag{A.4}$$

Next, we consider the complementary problem (b). In problem (b), we consider the aperture on $z = 0$ screen. The shape of aperture is the same shape as A. The total wave $\tilde{\psi}'$ in $z \geq 0$ is given by

$$\tilde{\psi}'(\boldsymbol{x}) = \frac{1}{4\pi}\int_{\mathrm{A}} \frac{\mathrm{e}^{\mathrm{i}kR}}{R}\boldsymbol{e}_z \cdot \left[\nabla'\tilde{\psi}_{\mathrm{i}} + \mathrm{i}k\left(1+\frac{\mathrm{i}}{kR}\right)\frac{\boldsymbol{R}}{R}\tilde{\psi}_{\mathrm{i}}\right]\mathrm{d}S'. \tag{A.5}$$

Then, we add these equations and obtain the Babinet's principle for scalar waves:

$$\tilde{\psi}_{\mathrm{in}} = \tilde{\psi} + \tilde{\psi}', \tag{A.6}$$

in $z \geq 0$. The above discussion depends on the validity of the Kirchhoff approximation. This approximation has been criticized from various points of views. It is known that this approximation is valid for an aperture in a black screen whose linear dimensions are large compared to the wavelength [171].

A.4.2 Rigorous scalar Babinet's principle

This subsection is based on Bouwkamp's paper [172]. We introduce two boundary conditions for surfaces:

- Soft boundary: $\tilde{\psi} = 0$.
- Hard boundary: $\partial\tilde{\psi}/\partial n = 0$, where n is the coordinate normal to the surface.

In acoustics [173], the normal component of velocity vector $\tilde{\boldsymbol{v}} = -\nabla\tilde{\psi}$ to the surface is 0 on the hard boundary (ψ represents the potential). The pressure is proportional to $\tilde{\psi}$, so it is 0 on the soft boundary.

At first, we consider incident wave $\tilde{\psi}(x, y, z)$ is illuminated from $z \leq 0$ to the thin planar soft boundary A on $z = 0$. This situation is called problem (a1), and shown in Fig. A.1 (1). The other part of $z = 0$ except A is denoted by B. The incident wave can be decomposed to symmetric component $[\tilde{\psi}(x, y, z)+\tilde{\psi}(x, y, -z)]/2$, and antisymmetric one $[\tilde{\psi}(x, y, z) - \tilde{\psi}(x, y, -z)]/2$. For the antisymmetric component, the soft-boundary condition is automatically satisfied and there is no scattered wave. The symmetric

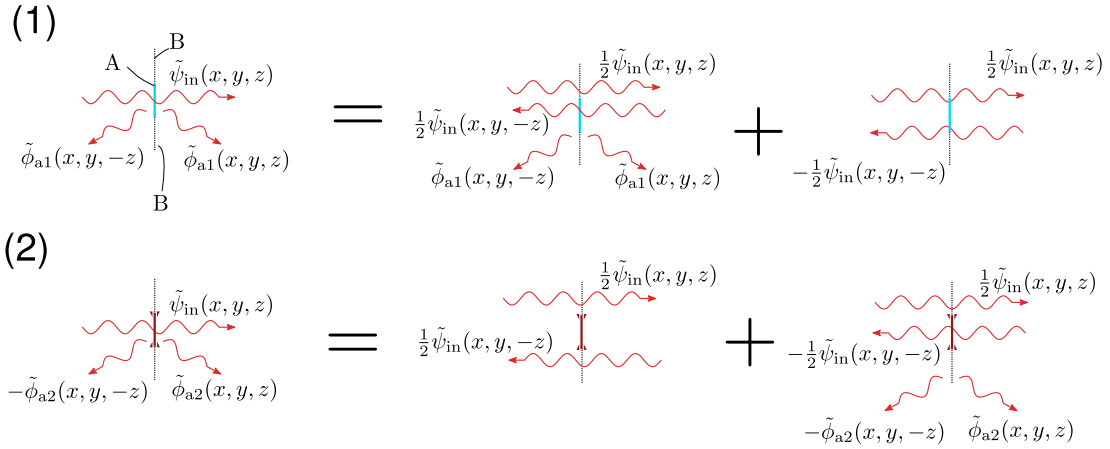

Figure A.1: Two problem with different boundary conditions - (1) problem with the soft boundary. (2) problem with the hard boundary

incident component is scattered symmetrically as shown in Fig. A.1 (1). Then, the total field in problem (a1) is given by

$$\tilde{\psi} = \begin{cases} \tilde{\psi}_{\rm in}(x,y,z) + \tilde{\phi}_{\rm a1}(x,y,-z) & (z \leq 0) \\ \tilde{\psi}_{\rm in}(x,y,z) + \tilde{\phi}_{\rm a1}(x,y,z) & (z \geq 0) \end{cases}. \tag{A.7}$$

Boundary conditions on $z = 0$ are written as follows:

- On A: $\tilde{\phi}_{\rm a1} = -\tilde{\psi}_{\rm in}$ (soft boundary).
- On B: $\partial\tilde{\phi}_{\rm a1}/\partial z = 0$ (continuity of $\partial\tilde{\psi}/\partial z$).

If we assume the radiation boundary for $\tilde{\phi}_{\rm a1}$ at infinity, the solution of the Helmholtz equation can be solved uniquely[1]. Similarly, we can consider the scattering by the same shape with the hard boundary [problem (a2)] as in Fig. A.1 (2). In this case, symmetrical incident component creates no scattered waves. Therefore, antisymmetric scattered fields $\pm\tilde{\phi}_{\rm a2}(x,y,\pm z)$ are generated. Then, the total field in problem (a2) is given by

$$\tilde{\psi} = \begin{cases} \tilde{\psi}_{\rm in}(x,y,z) - \tilde{\phi}_{\rm a2}(x,y,-z) & (z \leq 0) \\ \tilde{\psi}_{\rm in}(x,y,z) + \tilde{\phi}_{\rm a2}(x,y,z) & (z \geq 0) \end{cases}. \tag{A.8}$$

The boundary conditions on $z = 0$ are written as follows:

- On A: $\partial\tilde{\phi}_{\rm a2}/\partial z = -\partial\tilde{\psi}_{\rm in}/\partial z$ (hard boundary).

[1] Rigorously, some mathematical conditions are needed [172].

- On B: $\tilde{\phi}_{\mathrm{a}2} = 0$ (continuity of $\tilde{\psi}$).

Here, we consider complementary problems in which the surface and aperture are exchanged [See Fig. A.2]. In problem (b1), the total field is given by

$$\tilde{\psi} = \begin{cases} \tilde{\psi}_{\mathrm{in}}(x,y,z) - \tilde{\psi}_{\mathrm{in}}(x,y,-z) + \tilde{\phi}_{\mathrm{b}1}(x,y,-z) & (z \leq 0) \\ \tilde{\phi}_{\mathrm{b}1}(x,y,z) & (z \geq 0) \end{cases}. \tag{A.9}$$

If we assume

$$\tilde{\phi}_{\mathrm{b}1}(x,y,z) = -\tilde{\phi}_{\mathrm{a}2}(x,y,z) \qquad (z \geq 0), \tag{A.10}$$

the following boundary conditions are automatically satisfied:

- On A: $\partial\tilde{\phi}_{\mathrm{b}1}/\partial z = \partial\tilde{\psi}_{\mathrm{in}}/\partial z$ (continuity of $\partial\tilde{\psi}/\partial z$).
- On B: $\tilde{\phi}_{\mathrm{b}1} = 0$ (soft boundary)

In problem (b2), total field are given by

$$\tilde{\psi} = \begin{cases} \tilde{\psi}_{\mathrm{in}}(x,y,z) + \tilde{\psi}_{\mathrm{in}}(x,y,-z) - \tilde{\phi}_{\mathrm{b}2}(x,y,-z) & (z \leq 0) \\ \tilde{\phi}_{\mathrm{b}2}(x,y,z) & (z \geq 0) \end{cases}. \tag{A.11}$$

If we assume

$$\tilde{\phi}_{\mathrm{b}2}(x,y,z) = -\tilde{\phi}_{\mathrm{a}1}(x,y,z) \qquad (z \geq 0), \tag{A.12}$$

the following boundary conditions are satisfied:

- On A: $\tilde{\phi}_{\mathrm{b}2} = \tilde{\psi}_{\mathrm{in}}$ (continuity of $\tilde{\psi}$)
- On B: $\partial\tilde{\phi}_{\mathrm{b}2}/\partial z = 0$ (hard boundary).

As described above, problem (a1) and problem (b2) [problem (a2) and problem (b1)] are related. These are rigorous version of scalar Babinet's principle. However, the practical implementation of ideal boundary conditions in acoustics may be difficult.

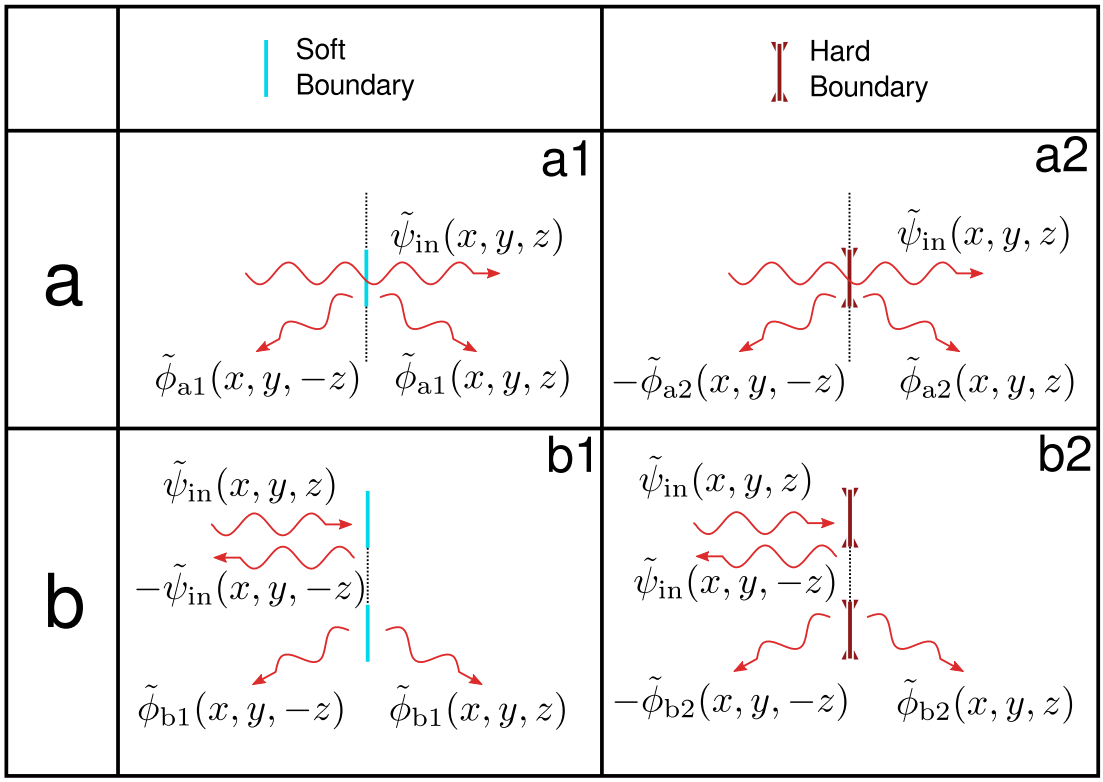

Figure A.2: Four problems for scalar Babinet's principle - Babinet's principle are formulated for (a1) $\leftrightarrow$ (b2), and (a2) $\leftrightarrow$ (b1).

References

[1] T. W. Ebbesen, H. J. Lezec, H. F. Ghaemi, T. Thio, and P. A. Wolff, "Extraordinary optical transmission through sub-wavelength hole arrays," Nature **391**, 667 (1998).

[2] H. Bethe, "Theory of Diffraction by Small Holes," Phys. Rev. **66**, 163 (1944).

[3] F. J. García de Abajo, "Colloquium: Light scattering by particle and hole arrays," Rev. Mod. Phys. **79**, 1267 (2007).

[4] R. Wood, "XLII. On a remarkable case of uneven distribution of light in a diffraction grating spectrum," Philos. Mag. **4**, 396 (1902).

[5] R. Wood, "Anomalous Diffraction Gratings," Phys. Rev. **48**, 928 (1935).

[6] U. Fano, "The Theory of Anomalous Diffraction Gratings and of Quasi-Stationary Waves on Metallic Surfaces (Sommerfelds Waves)," J. Opt. Soc. Am. **31**, 213 (1941).

[7] P. Lalanne and J. P. Hugonin, "Interaction between optical nano-objects at metallo-dielectric interfaces," Nature Physics **2**, 551 (2006).

[8] H. Liu and P. Lalanne, "Microscopic theory of the extraordinary optical transmission," Nature **452**, 728 (2008).

[9] F. van Beijnum, C. Rétif, C. B. Smiet, H. Liu, P. Lalanne, and M. P. van Exter, "Quasi-cylindrical wave contribution in experiments on extraordinary optical transmission," Nature **492**, 411 (2012).

[10] V. P. Bykov, "Spontaneous emission in a periodic structure," Sov. Phys. JETP **35**, 269 (1972).

[11] V. P. Bykov, "Spontaneous emission from a medium with a band spectrum," Sov. J. Quantum Electron. **4**, 861 (1975).

[12] K. Ohtaka, "Energy band of photons and low-energy photon diffraction," Phys. Rev. B **19**, 5057 (1979).

[13] E. Yablonovitch, "Inhibited Spontaneous Emission in Solid-State Physics and Electronics," Phys. Rev. Lett. **58**, 2059 (1987).

[14] S. John, "Strong localization of photons in certain disordered dielectric superlattices," Phys. Rev. Lett. **58**, 2486 (1987).

[15] J. Joannopoulos, S. Johnson, J. Winn, and R. Meade, *Photonic crystals: molding the flow of light*, 2nd ed. (Princeton university press, Princeton and Oxford, 2011).

[16] E. Yablonovitch and T. Gmitter, "Photonic band structure: The face-centered-cubic case," Phys. Rev. Lett. **63**, 1950 (1989).

REFERENCES

[17] E. Yablonovitch, T. Gmitter, and K. Leung, "Photonic band structure: The face-centered-cubic case employing nonspherical atoms," Phys. Rev. Lett. **67**, 2295 (1991).

[18] T. F. Krauss, R. M. D. L. Rue, and S. Brand, "Two-dimensional photonic-bandgap structures operating at near-infrared wavelengths," Nature **383**, 699 (1996).

[19] Y. Akahane, T. Asano, B.-S. Song, and S. Noda, "High-Q photonic nanocavity in a two-dimensional photonic crystal," Nature **425**, 944 (2003).

[20] E. Kuramochi, H. Taniyama, T. Tanabe, K. Kawasaki, Y.-G. Roh, and M. Notomi, "Ultrahigh-Q one-dimensional photonic crystal nanocavities with modulated mode-gap barriers on SiO2 claddings and on air claddings," Opt. Express **18**, 15859 (2010).

[21] Y. Taguchi, Y. Takahashi, Y. Sato, T. Asano, and S. Noda, "Statistical studies of photonic heterostructure nanocavities with an average Q factor of three million," Opt. Express **19**, 11916 (2011).

[22] T. Baba, "Slow light in photonic crystals," Nat. Photon. **2**, 465 (2008).

[23] R. M. Walser, "Metamaterials: What are they? What are they good for?" in *APS meeting* (Minneapolis, 2000) [http://flux.aps.org/meetings/YR00/MAR00/abs/S9240001.html].

[24] E. Yablonovitch, "Photonic Bandgap Structures as Meta-Materials," in *APS meeting* (Minneapolis, 2000) [http://flux.aps.org/meetings/YR00/MAR00/abs/S9240002.html].

[25] A. Lakhtakia, "Sculptured Thin Films: Accomplishments and Promises," in *APS meeting* (Minneapolis, 2000) [http://flux.aps.org/meetings/YR00/MAR00/abs/S9240003.html].

[26] C. T. Black, "Electron Tunneling in Self-Assembled Nanocrystal Superlattices," in *APS meeting* (Minneapolis, 2000) [http://flux.aps.org/meetings/YR00/MAR00/abs/S9240004.html].

[27] R. W. Ziolkowski, "Synthesis of Smart Skins Using Artificial Dielectric and Magnetic Molecules," in *APS meeting* (Minneapolis, 2000)
[http://flux.aps.org/meetings/YR00/MAR00/abs/S9240005.html].

[28] D. Smith, W. Padilla, D. Vier, S. Nemat-Nasser, and S. Schultz, "Composite Medium with Simultaneously Negative Permeability and Permittivity," Phys. Rev. Lett. **84**, 4184 (2000).

[29] V. G. Veselago, "The electrodynamics of substances with simultaneously negative values of ϵ and μ," Sov. Phys. Usp. **10**, 509 (1968).

[30] J. B. Pendry, A. J. Holden, W. J. Stewart, and I. Youngs, "Extremely Low Frequency Plasmons in Metallic Mesostructures," Phys. Rev. Lett. **76**, 4773 (1996).

[31] J. Pendry, A. Holden, D. Robbins, and W. Stewart, "Magnetism from conductors and enhanced nonlinear phenomena," IEEE Trans. Microwave Theory Tech. **47**, 2075 (1999).

[32] D. R. Smith, D. C. Vier, N. Kroll, and S. Schultz, "Direct calculation of permeability and permittivity for a left-handed metamaterial," Appl. Phys. Lett. **77**, 2246 (2000).

[33] R. A. Shelby, D. R. Smith, and S. Schultz, "Experimental verification of a negative index of refraction," Science **292**, 77 (2001).

[34] J. Valentine, S. Zhang, T. Zentgraf, E. Ulin-Avila, D. A. Genov, G. Bartal, and X. Zhang, "Three-dimensional optical metamaterial with a negative refractive index," Nature **455**, 376 (2008).

[35] J. Pendry and S. Ramakrishna, "Focusing light using negative refraction," J. Phys.: Condens. Matter **15**, 6345 (2003).

[36] A. Lagarkov and V. Kissel, "Near-Perfect Imaging in a Focusing System Based on a Left-Handed-Material Plate," Phys. Rev. Lett. **92**, 077401 (2004).

[37] K. Aydin, I. Bulu, and E. Ozbay, "Subwavelength resolution with a negative-index metamaterial superlens," Appl. Phys. Lett. **90**, 254102 (2007).

[38] D. O. S. Melville, R. J. Blaikie, and C. R. Wolf, "Submicron imaging with a planar silver lens," Appl. Phys. Lett. **84**, 4403 (2004).

[39] D. O. S. Melville and R. J. Blaikie, "Super-resolution imaging through a planar silver layer," Opt. Express **13**, 2127 (2005).

[40] D. O. S. Melville and R. J. Blaikie, "Experimental comparison of resolution and pattern fidelity in single- and double-layer planar lens lithography," J. Opt. Soc. Am. B **23**, 461 (2006).

[41] N. Fang, H. Lee, C. Sun, and X. Zhang, "Sub-diffraction-limited optical imaging with a silver superlens," Science **308**, 534 (2005).

[42] H. Lee, Y. Xiong, N. Fang, W. Srituravanich, S. Durant, M. Ambati, C. Sun, and X. Zhang, "Realization of optical superlens imaging below the diffraction limit," New J. Phys. **7**, 255 (2005).

[43] D. Korobkin, Y. Urzhumov, and G. Shvets, "Enhanced near-field resolution in midinfrared using metamaterials," J. Opt. Soc. Am. B **23**, 468 (2006).

[44] T. Taubner, D. Korobkin, Y. Urzhumov, G. Shvets, and R. Hillenbrand, "Near-field microscopy through a SiC superlens," Science **313**, 1595 (2006).

[45] J. Pendry and S. Ramakrishna, "Near-field lenses in two dimensions," J. Phys.: Condens. Matter **14**, 8463 (2002).

[46] J. Pendry, "Perfect cylindrical lenses," Opt. Express **11**, 755 (2003).

[47] Z. Jacob, L. V. Alekseyev, and E. Narimanov, "Optical Hyperlens: Far-field imaging beyond the diffraction limit," Opt. Express **14**, 8247 (2006).

[48] A. Salandrino and N. Engheta, "Far-field subdiffraction optical microscopy using metamaterial crystals: Theory and simulations," Phys. Rev. B **74**, 075103 (2006).

[49] Z. Liu, H. Lee, Y. Xiong, C. Sun, and X. Zhang, "Far-field optical hyperlens magnifying sub-diffraction-limited objects," Science **315**, 1686 (2007).

[50] I. I. Smolyaninov, Y.-J. Hung, and C. C. Davis, "Magnifying superlens in the visible frequency range," Science **315**, 1699 (2007).

[51] U. Leonhardt, "Optical conformal mapping," Science **312**, 1777 (2006).

[52] J. B. Pendry, D. Schurig, and D. R. Smith, "Controlling electromagnetic fields," Science **312**, 1780 (2006).

[53] J. B. Pendry, A. Aubry, D. R. Smith, and S. a. Maier, "Transformation optics and subwavelength control of light," Science **337**, 549 (2012).

[54] F. L. Teixeira, "Differential form approach to the analysis of electromagnetic cloaking and masking," Microw. Opt. Technol. Lett. **49**, 2051 (2007).

[55] D. Schurig, J. J. Mock, B. J. Justice, S. A. Cummer, J. B. Pendry, A. F. Starr, and D. R. Smith, "Metamaterial electromagnetic cloak at microwave frequencies," Science **314**, 977 (2006).

[56] W. Cai, U. K. Chettiar, A. V. Kildishev, and V. M. Shalaev, "Optical cloaking with metamaterials," Nat. Photon. **1**, 224 (2007).

[57] R. Liu, C. Ji, J. J. Mock, J. Y. Chin, T. J. Cui, and D. R. Smith, "Broadband ground-plane cloak," Science **323**, 366 (2009).

[58] J. Valentine, J. Li, T. Zentgraf, G. Bartal, and X. Zhang, "An optical cloak made of dielectrics," Nat. Mater. **8**, 568 (2009).

[59] A. V. Kildishev, A. Boltasseva, and V. M. Shalaev, "Planar photonics with metasurfaces," Science **339**, 1232009 (2013).

[60] B. A. Munk, *Frequency Selective Surfaces: Theory and Design* (Wiley & Sons, New York, 2000).

[61] N. Yu, P. Genevet, M. A. Kats, F. Aieta, J.-P. Tetienne, F. Capasso, and Z. Gaburro, "Light propagation with phase discontinuities: generalized laws of reflection and refraction," Science **334**, 333 (2011).

[62] X. Ni, N. K. Emani, A. V. Kildishev, A. Boltasseva, and V. M. Shalaev, "Broadband light bending with plasmonic nanoantennas," Science **335**, 427 (2012).

[63] C. Pfeiffer and A. Grbic, "Metamaterial Huygens Surfaces: Tailoring Wave Fronts with Reflectionless Sheets," Phys. Rev. Lett. **110**, 197401 (2013).

[64] F. Monticone, N. M. Estakhri, and A. Alù, "Full Control of Nanoscale Optical Transmission with a Composite Metascreen," Phys. Rev. Lett. **110**, 203903 (2013).

[65] M. Kadic, T. Bückmann, R. Schittny, and M. Wegener, "Metamaterials beyond electromagnetism," Rep. Prog. Phys. **76**, 126501 (2013).

[66] N. Wongkasem, A. Akyurtlu, and K. A. Marx, "Group theory based design of isotropic negative refractive index metamaterials," Prog. Electromagn. Res. **63**, 295 (2006).

[67] J. D. Baena, L. Jelinek, and R. Marqués, "Towards a systematic design of isotropic bulk magnetic metamaterials using the cubic point groups of symmetry," Phys. Rev. B **76**, 245115 (2007).

[68] W. J. Padilla, "Group theoretical description of artificial electromagnetic metamaterials," Opt. Express **15**, 1639 (2007).

[69] C. M. Reinke, T. M. De la Mata Luque, M. F. Su, M. B. Sinclair, and I. El-Kady, "Group-theory approach to tailored electromagnetic properties of metamaterials: An inverse-problem solution," Phys. Rev. E **83**, 066603 (2011).

[70] O. Isik and K. P. Esselle, "Analysis of spiral metamaterials by use of group theory," Metamaterials **3**, 33 (2009).

[71] C. M. Bingham, H. Tao, X. Liu, R. D. Averitt, X. Zhang, and W. J. Padilla, "Planar wallpaper group metamaterials for novel terahertz applications," Opt. Express **16**, 18565 (2008).

[72] Y. Nakata, T. Okada, T. Nakanishi, and M. Kitano, "Circuit model for hybridization modes in metamaterials and its analogy to the quantum tight-binding model," Phys. Status Solidi B **249**, 2293 (2012).

[73] Y. Nakata, T. Okada, T. Nakanishi, and M. Kitano, "Observation of flat band for terahertz spoof plasmons in a metallic kagomé lattice," Phys. Rev. B **85**, 205128 (2012).

[74] Y. Nakata, Y. Urade, T. Nakanishi, and M. Kitano, "Plane-wave scattering by self-complementary metasurfaces in terms of electromagnetic duality and Babinet's principle," Phys. Rev. B **88**, 205138 (2013).

[75] H. Liu, Y. M. Liu, T. Li, S. M. Wang, S. N. Zhu, and X. Zhang, "Coupled magnetic plasmons in metamaterials," Phys. Status Solidi B **246**, 1397 (2009).

[76] N. Stefanou and A. Modinos, "Impurity bands in photonic insulators," Phys. Rev. B **57**, 12127 (1998).

[77] A. Yariv, Y. Xu, R. K. Lee, and A. Scherer, "Coupled-resonator optical waveguide: a proposal and analysis," Opt. Lett. **24**, 711 (1999).

[78] A. Boag and B. Z. Steinberg, "Narrow-band microcavity waveguides in photonic crystals," J. Opt. Soc. Am. A **18**, 2799 (2001).

[79] E. Lidorikis, M. M. Sigalas, E. N. Economou, and C. M. Soukoulis, "Tight-Binding Parametrization for Photonic Band Gap Materials," Phys. Rev. Lett. **81**, 1405 (1998).

[80] M. Bayindir, B. Temelkuran, and E. Ozbay, "Tight-Binding Description of the Coupled Defect Modes in Three-Dimensional Photonic Crystals," Phys. Rev. Lett. **84**, 2140 (2000).

[81] Y. Hara, T. Mukaiyama, K. Takeda, and M. Kuwata-Gonokami, "Heavy Photon States in Photonic Chains of Resonantly Coupled Cavities with Supermonodispersive Microspheres," Phys. Rev. Lett. **94**, 203905 (2005).

[82] M. Notomi, E. Kuramochi, and T. Tanabe, "Large-scale arrays of ultrahigh-Q coupled nanocavities," Nat. Photon. **2**, 741 (2008).

[83] D. Leuenberger, "Ab initio tight-binding approach to photonic-crystal based coupled cavity waveguides," J. Appl. Phys. **95**, 806 (2004).

[84] K. Busch, S. F. Mingaleev, A. Garcia-Martin, M. Schillinger, and D. Hermann, "The Wannier function approach to photonic crystal circuits," J. Phys.: Condens. Matter **15**, R1233 (2003).

[85] S. Endo, T. Oka, and H. Aoki, "Tight-binding photonic bands in metallophotonic waveguide networks and flat bands in kagome lattices," Phys. Rev. B **81**, 113104 (2010).

[86] H. Xu, Q. He, S. Xiao, B. Xi, J. Hao, and L. Zhou, "Tight-binding analysis of coupling effects in metamaterials," J. Appl. Phys. **109**, 023103 (2011).

[87] B. Xi, H. Xu, S. Xiao, and L. Zhou, "Theory of coupling in dispersive photonic systems," Phys. Rev. B **83**, 165115 (2011).

[88] M. E. Verbeek, "Partial element equivalent circuit (PEEC) models for onchip passives and interconnects," Int. J. Numer. Model. **17**, 61 (2004).

[89] N. Engheta, "Circuits with light at nanoscales: optical nanocircuits inspired by metamaterials," Science **317**, 1698 (2007).

[90] R. Marqués, F. Medina, and R. Rafii-El-Idrissi, "Role of bianisotropy in negative permeability and left-handed metamaterials," Phys. Rev. B **65**, 144440 (2002).

[91] M. Shamonin, E. Shamonina, V. Kalinin, and L. Solymar, "Properties of a metamaterial element: Analytical solutions and numerical simulations for a singly split double ring," J. Appl. Phys. **95**, 3778 (2004).

[92] M. Shamonin, E. Shamonina, V. Kalinin, and L. Solymar, "Resonant frequencies of a split-ring resonator: Analytical solutions and numerical simulations," Microw. Opt. Technol. Lett. **44**, 133 (2005).

[93] M. C. Wiltshire, E. Shamonina, I. R. Young, and L. Solymar, "Dispersion characteristics of magneto-inductive waves: comparison between theory and experiment," Electron. Lett. **39**, 215 (2003).

[94] G. K. G. Carter and G. Kron, "A.C. Network Analyzer Study of the Schrödinger Equation," Phys. Rev. **67**, 44 (1945).

[95] E. Shamonina, V. A. Kalinin, K. H. Ringhofer, and L. Solymar, "Magnetoinductive waves in one, two, and three dimensions," J. Appl. Phys. **92**, 6252 (2002).

[96] E. Shamonina, V. Kalinin, K. H. Ringhofer, and L. Solymar, "Magneto-inductive waveguide," Electron. Lett. **38**, 371 (2002).

[97] G. Kron, "Electric Circuit Models of the Schrödinger Equation," Phys. Rev. **67**, 39 (1945).

[98] H. Liu, D. Genov, D. Wu, Y. Liu, and J. Steele, "Magnetic plasmon propagation along a chain of connected subwavelength resonators at infrared frequencies," Phys. Rev. Lett. **97**, 243902 (2006).

[99] H. Liu, T. Li, Q. J. Wang, Z. H. Zhu, S. M. Wang, J. Q. Li, S. N. Zhu, Y. Y. Zhu, and X. Zhang, "Extraordinary optical transmission induced by excitation of a magnetic plasmon propagation mode in a diatomic chain of slit-hole resonators," Phys. Rev. B **79**, 024304 (2009).

[100] E. Lieb, "Two theorems on the Hubbard model," Phys. Rev. Lett. **62**, 1201 (1989).

[101] H. Tasaki, "Ferromagnetism in the Hubbard models with degenerate single-electron ground states," Phys. Rev. Lett. **69**, 1608 (1992).

[102] A. Mielke, "Ferromagnetism in the Hubbard model on line graphs and further considerations," J. Phys. A **24**, 3311 (1991).

[103] J. Nielsen, T. Sondergaard, S. Barkou, A. Bjarklev, J. Broeng, and M. Nielsen, "Two-dimensional Kagome structure, fundamental hexagonal photonic crystal configuration," Electron. Lett. **35**, 1736 (1999).

[104] H. Takeda, T. Takashima, and K. Yoshino, "Flat photonic bands in two-dimensional photonic crystals with kagome lattices," J. Phys.: Condens. Matter **16**, 6317 (2004).

[105] E. Feigenbaum and H. A. Atwater, "Resonant Guided Wave Networks," Phys. Rev. Lett. **104**, 147402 (2010).

[106] J. L. Atwood, "Kagomé lattice: A molecular toolkit for magnetism," Nat. Mater. **1**, 91 (2002).

[107] C. Zhu, H. Liu, S. M. Wang, T. Li, J. X. Cao, Y. J. Zheng, L. Li, Y. Wang, S. N. Zhu, and X. Zhang, "Electric and magnetic excitation of coherent magnetic plasmon waves in a one-dimensional meta-chain," Opt. Express **18**, 26268 (2010).

[108] M. Tani, S. Matsuura, K. Sakai, and S. Nakashima, "Emission characteristics of photoconductive antennas based on low-temperature-grown GaAs and semi-insulating GaAs," Appl. Opt. **36**, 7853 (1997).

[109] Y.-S. Lee, *Principles of Terahertz Science and Technology* (Springer, New York, 2008).

[110] L. Solymar and E. Shamonina, *Waves in Metamaterials* (Oxford, 2009) p. 385.

[111] H. Altug and J. Vučković, "Two-dimensional coupled photonic crystal resonator arrays," Appl. Phys. Lett. **84**, 161 (2004).

[112] H. Altug and J. Vučković, "Experimental demonstration of the slow group velocity of light in two-dimensional coupled photonic crystal microcavity arrays," Appl. Phys. Lett. **86**, 111102 (2005).

[113] Y. Tamayama, T. Nakanishi, and M. Kitano, "Variable group delay in a metamaterial with field-gradient-induced transparency," Phys. Rev. B **85**, 073102 (2012).

[114] Y. Tamayama, T. Nakanishi, Y. Wakasa, T. Kanazawa, K. Sugiyama, and M. Kitano, "Electromagnetic response of a metamaterial with field-gradient-induced transparency," Phys. Rev. B **82**, 165130 (2010).

[115] M. G. Calkin, "An Invariance Property of the Free Electromagnetic Field," Am. J. Phys. **33**, 958 (1965).

[116] D. Zwanziger, "Quantum Field Theory of Particles with Both Electric and Magnetic Charges," Phys. Rev. **176**, 1489 (1968).

[117] S. Deser and C. Teitelboim, "Duality transformations of Abelian and non-Abelian gauge fields," Phys. Rev. D **13**, 1592 (1976).

[118] P. D. Drummond, "Dual symmetric Lagrangians and conservation laws," Phys. Rev. A **60**, R3331 (1999).

[119] S. M. Barnett, R. P. Cameron, and A. M. Yao, "Duplex symmetry and its relation to the conservation of optical helicity," Phys. Rev. A **86**, 013845 (2012).

[120] R. P. Cameron and S. M. Barnett, "Electricmagnetic symmetry and Noether's theorem," New J. Phys. **14**, 123019 (2012).

[121] K. Y. Bliokh, A. Y. Bekshaev, and F. Nori, "Dual electromagnetism: helicity, spin, momentum and angular momentum," New J. Phys. **15**, 033026 (2013).

[122] I. Fernandez-Corbaton, X. Zambrana-Puyalto, N. Tischler, X. Vidal, M. L. Juan, and G. Molina-Terriza, "Electromagnetic Duality Symmetry and Helicity Conservation for the Macroscopic Maxwells Equations," Phys. Rev. Lett. **111**, 060401 (2013).

[123] O. Heaviside, "On the Forces, Stresses, and Fluxes of Energy in the Electromagnetic Field," Phil. Trans. R. Soc. Lond. A **183**, 423 (1892).

[124] J. Larmor, "A Dynamical Theory of the Electric and Luminiferous Medium," Phil. Trans. Roy. Soc. **190**, 205 (1893).

[125] G. Y. Rainich, "Electrodynamics in the general relativity theory," Trans. Am. Math. Soc. **27**, 106 (1925).

[126] M. Babinet, "Mémoires d'optique Météorologique," C. R. Acad. Sci. **4**, 638 (1837).

[127] H. Booker, "Slot aerials and their relation to complementary wire aerials (Babinet's principle)," J. IEE (London), part IIIA **93**, 620 (1946).

[128] E. T. Copson, "An Integral-Equation Method of Solving Plane Diffraction Problems," Proc. R. Soc. Lond. A. **186**, 100 (1946).

[129] J. Mexner, "Das Babinetsche Prinzip der Optik," Z. Naturforschg. **1**, 496 (1946).

[130] M. Leontovich, "On a theorem in the theory of diffraction and its application to diffraction by a narrow slit of arbitrary length," Zh. Eksp. Theor. Fiz. **16**, 474 (1946).

[131] L. D. Landau, E. M. Lifshitz, and L. P. Pitaevskii, *Electrodynamics of Continuous Media*, 2nd ed. (Pergamon Press, Oxford, 1984).

[132] M. Kotani, H. Takahashi, and T. Kihara, "On the leaking of electromagnetic waves," in *Recent developments in the measurement of ultrashort waves (in Japanese)* (Korona, Tokyo, 1948) pp. 126–134.

[133] H. E. J. Neugebauer, "Extension of Babinet's Principle to Absorbing and Transparent Materials, and Approximate Theory of Backscattering by Plane, Absorbing Disks," J. Appl. Phys. **28**, 302 (1957).

[134] C. E. Baum and B. K. Singaraju, "Generalization of Babinet's principle in terms of the combined field to include impedance loaded aperture antennas and scatterers," Interaction Note No.217 (Air Force Weapons Lab., Kirtland Air Force Base, NM 87117) (1974).

[135] C. E. Baum and H. N. Kritikos, eds., *Electromagnetic Symmetry* (Taylor & Francis, Washington, 1995).

[136] J. Moore, "Extension of the Babinet principle to scatterers with lumped impedance loads," Electron. Lett. **29**, 301 (1993).

[137] F. Falcone, T. Lopetegi, M. A. G. Laso, J. D. Baena, J. Bonache, M. Beruete, R. Marqués, F. Martín, and M. Sorolla, "Babinet Principle Applied to the Design of Metasurfaces and Metamaterials," Phys. Rev. Lett. **93**, 197401 (2004).

[138] I. A. I. Al-Naib, C. Jansen, and M. Koch, "Applying the Babinet principle to asymmetric resonators," Electron. Lett. **44**, 1228 (2008).

[139] H.-T. Chen, J. F. O'Hara, A. J. Taylor, R. D. Averitt, C. Highstrete, M. Lee, and W. J. Padilla, "Complementary planar terahertz metamaterials," Opt. Express **15**, 1084 (2007).

[140] T. Zentgraf, T. P. Meyrath, A. Seidel, S. Kaiser, H. Giessen, C. Rockstuhl, and F. Lederer, "Babinets principle for optical frequency metamaterials and nanoantennas," Phys. Rev. B **76**, 033407 (2007).

[141] A. Bitzer, A. Ortner, H. Merbold, T. Feurer, and M. Walther, "Terahertz near-field microscopy of complementary planar metamaterials: Babinet's principle," Opt. Express **19**, 2537 (2011).

[142] Y. U. Lee, E. Y. Choi, J. H. Woo, E. S. Kim, and J. W. Wu, "Reflection resonance switching in metamaterial twisted nematics cell," Opt. Express **21**, 17492 (2013).

[143] L. Zhang, T. Koschny, and C. M. Soukoulis, "Creating double negative index materials using the Babinet principle with one metasurface," Phys. Rev. B **87**, 045101 (2013).

[144] M. Beruete, M. Navarro Cía, I. Campillo, P. Goy, and M. Sorolla, "Quasioptical Polarizer Based on Self-Complementary Sub-Wavelength Hole Arrays," IEEE Microw. Wirel. Compon. Lett. **17**, 834 (2007).

[145] J. D. Ortiz, J. D. Baena, V. Losada, F. Medina, R. Marqués, and J. A. Quijano, "Self-Complementary Metasurface for Designing Narrow Band Pass/Stop Filters," IEEE Microw. Wirel. Compon. Lett. **23**, 291 (2013).

[146] Y. Mushiake, "Self-complementary antennas," IEEE Antennas Propag. Mag. **34**, 23 (1992).

[147] Y. Mushiake, *Self-Complementary Antennas: Principle of Self-Complementarity for Constant Impedance* (Springer, London, 1996).

[148] R. Singh, C. Rockstuhl, C. Menzel, T. P. Meyrath, M. He, H. Giessen, F. Lederer, and W. Zhang, "Spiral-type terahertz antennas and the manifestation of the Mushiake principle," Opt. Express **17**, 9971 (2009).

[149] R. C. Compton, J. C. Macfarlane, L. B. Whitbourn, M. M. Blanco, and R. C. McPhedran, "Babinet's Principle Applied to Ideal Beam-splitters for Submillimetre Waves," Opt. Acta **31**, 515 (1984).

[150] K. Takano, F. Miyamaru, K. Akiyama, Y. Chiyoda, H. Miyazaki, M. W. Takeda, Y. Abe, Y. Tokuda, H. Ito, and M. Hangyo, "Terahertz responses of near self-complementary metallic checkerboard patterns," in *Proceedings of the 34th International Conference on Infrared, Millimeter, and Terahertz Waves* (IEEE, New York, 2009).

[151] W. L. Burke, *Applied Differential Geometry* (Cambridge University Press, Cambridge, 1985).

[152] R. E. Collin, *Field theory of guided waves*, 2nd ed. (IEEE Press, New York, 1991).

[153] Y. D. Chong, L. Ge, H. Cao, and A. D. Stone, "Coherent Perfect Absorbers: Time-Reversed Lasers," Phys. Rev. Lett. **105**, 053901 (2010).

[154] W. Wan, Y. Chong, L. Ge, H. Noh, A. D. Stone, and H. Cao, "Time-reversed lasing and interferometric control of absorption," Science **331**, 889 (2011).

[155] Y. Yagil and G. Deutscher, "Transmittance of thin metal films near the percolation threshold," Thin Solid Films **152**, 465 (1987).

[156] Y. Yagil and G. Deutscher, "Scaling and renormalization in transmittance of thin metal films near the percolation threshold," Appl. Phys. Lett. **52**, 373 (1988).

[157] P. Gadenne, A. Beghdadi, and J. Lafait, "Optical cross-over analysis of granular gold films at percolation," Opt. Commun. **65**, 17 (1988).

[158] P. Gadenne, Y. Yagil, and G. Deutscher, "In-situ measurements of the optical properties of gold films near the percolation threshold," Physica A **157**, 279 (1989).

[159] A. Beghdadi, M. Gadenne, P. Gadenne, J. Lafait, A. Le Negrate, and A. Constans, "Criticism of the image analysis of discontinuous thin films," Physica A **157**, 64 (1989).

[160] C. A. Davis, D. R. McKenzie, and R. C. McPhedran, "Optical properties and microstructure of thin silver films," Opt. Commun. **85**, 70 (1991).

[161] A. K. Sarychev, D. J. Bergman, and Y. Yagil, "Theory of the optical and microwave properties of metal-dielectric films," Phys. Rev. B **51**, 5366 (1995).

[162] L. C. Botten, R. C. McPhedran, N. A. Nicorovici, and G. H. Derrick, "Periodic models for thin optimal absorbers of electromagnetic radiation," Phys. Rev. B **55**, R16072 (1997).

[163] J. D. Edmunds, A. P. Hibbins, J. R. Sambles, and I. J. Youngs, "Resonantly inverted microwave transmissivity threshold of metal grids," New J. Phys. **12**, 063007 (2010).

[164] K. Kempa, "Percolation effects in the checkerboard Babinet series of metamaterial structures," Phys. Status Solidi Rapid Res. Lett. **4**, 218 (2010).

[165] S. A. Ramakrishna, P. Mandal, K. Jeyadheepan, N. Shukla, S. Chakrabarti, M. Kadic, S. Enoch, and S. Guenneau, "Plasmonic interaction of visible light with gold nanoscale checkerboards," Phys. Rev. B **84**, 245424 (2011).

[166] R. C. Compton, L. B. Whitbourn, and R. C. McPhedran, "Strip gratings at a dielectric interface and application of Babinets principle," Appl. Opt. **23**, 3236 (1984).

[167] S. T. Shanahan and N. R. Heckenberg, "Transmission line model of substrate effects on capacitive mesh couplers," Appl. Opt. **20**, 4019 (1981).

[168] R. Marqués, V. Delgado, J. D. Baena, and J. D. Ortiz, "Complementarity and Babinet principle in optical nano-circuits and metamaterials," in *Metamaterials 2012: The Sixth International Congress on Advanced Electromagnetic Materials in Microwaves and Optics, St. Petersburg* (Louvain-la-Neuve, 2012) pp. 737–739.

[169] J. Baena, J. Ortiz, R. Marqués, and V. Delgado, "Duality in 2D optical nanocircuits," in *Metamaterials 2012: The Sixth International Congress on Advanced Electromagnetic Materials in Microwaves and Optics, St. Petersburg* (Louvain-la-Neuve, 2012) pp. 681–683.

[170] J. D. Jackson, *Classical Electrodynamics*, third edit ed. (Wiley, 1999).

[171] E. W. Marchand and E. Wolf, "Consistent Formulation of Kirchhoff's Diffraction Theory," J. Opt. Soc. Am. **56**, 1712 (1966).

[172] C. J. Bouwkamp, "Diffraction Theory," Rep. Prog. Phys. **17**, 35 (1954).

[173] B. Banerjee, *An Introduction to Metamaterials and Waves in Composites* (Taylor and Francis, Boca Raton, 2011).

Acknowledgements

I would like to express my gratitude to Prof. Masao Kitano who gave me a chance to study metamaterials in the graduate school of engineering. He introduced me the intuition of physics and the importance of circuits. I learned a lot of matters related and unrelated to the research from him. I would like to extend my gratitude to Prof. Osami Wada and Prof. Hirofumi Yamada for being part of my dissertation committee.

I wish to thank people in Kitano laboratory. Assistant Professor Toshihiro Nakanishi encouraged me and gave a lot of advice to me. He also taught me the importance of sports. I learned the attitude for experimental physics from Associate Professor Kazuhiko Sugiyama. I was impressed by the strict attitude of Dr. Yasuhiro Tamayama. I enjoyed a lot of discussion with Dr. Shuhei Tamate. I am particularly influenced by his great intuition on geometry and linear algebra. He has also supported me after his graduation. I am also thankful to Mr. Kazuhisa Ogawa. His zealous efforts to quantum optics gave me a lot of lessons. I express special gratitude to Mr. Yoshiro Urade in Kitano laboratory. I told him the previous research on checkerboard metasurfaces after I listened it in an international conference. He conducted the research on checkerboard metasurfaces from an independent standpoint. Without him, I have never accomplished to construct the theory of self-complementary metasurfaces. I am also grateful for the official assistance by Ms. Keiko Yamada and Ms. Chie Minari. I want to be grateful to all other members in Kitano laboratory.

I wish to thank people in the optical physics laboratory in the science department of Kyoto university. Prof. Koichiro Tanaka invited me to study terahertz metamaterials. I enjoyed a lot of discussion and jokes with Dr. Takanori Okada and Dr. Kazufumi Ooi. They introduced the previous work on

kagomé lattices, which was developed by Dr. Shimpei Endo in the University of Tokyo. I am also grateful to Dr. Endo for discussing physics with me directly.

I thank members in Hikihara laboratory of Kyoto university. Prof. Takashi Hikihara allowed me to use their laboratory equipment. Dr. Suketu Naik and Mr. Atsushi Yao taught me about tiny devices. I also enjoyed private life with Mr. Yao.

I am grateful to members in Hangyo laboratory of Osaka university. Especially, Dr. Masanori Hangyo and Dr. Keisuke Takano are acknowledged for discussing foundation of metamaterials. The study of self-complementary metasurface was inspired by their work.

This research was supported in part by Grants-in-Aid for Scientific Research No. 22109004, No. 22560041 and No. 25790065, the Global COE program Photonics and Electronics Science and Engineering at Kyoto University. The author is financially supported by the Japan Society for the Promotion of Science (JSPS). I express my appreciation to them.

I wish to thank my parents, my brother, my sister, and my relatives for supporting me. Ms. Mayuko Tanaka helped me in daily life. Finally, I would particularly like to express gratitude my deceased grand father Mr. Masao Hishikawa who taught me the spirit of science when I was a child.

List of publications and presentations

Journal articles

1. Yosuke Nakata, Takanori Okada, Toshihiro Nakanishi, and Masao Kitano, "Observation of flat band for terahertz spoof plasmon in a metallic kagomé lattice," APS, Physical Review B, **85**, 205128 (2012).
2. Yosuke Nakata, Takanori Okada, Toshihiro Nakanishi, and Masao Kitano, "Circuit model for hybridization modes in metamaterials and its analogy to the quantum tight-binding model," Wiley, Phys. Status Solidi B, **249**, 22932302 (2012).
3. Yosuke Nakata, Yoshiro Urade, Toshihiro Nakanishi, and Masao Kitano, "Plane-wave scattering by self-complementary metasurfaces in terms of electromagnetic duality and Babinet's principle," APS, Physical Review B, **88**, 205138 (2013).
4. Takanori Okada, Kazufumi Ooi, Yosuke Nakata, Koji Fujita, Katsuhisa Tanaka, and Koichiro Tanaka, "Direct creation of a photoinduced metallic structure and its optical properties in the terahertz frequency region," OSA, Optics Letters, **35**, 1719-1721 (2010).

International conferences (talk, refereed)

1. Yosuke Nakata, Yoshiro Urade, Toshihiro Nakanishi, and Masao Kitano, "Electromagnetic Response of Self-complementary Metasurfaces," PIERS 2013, Stockholm, Sweden (August 2013).
2. Yoshiro Urade, Yosuke Nakata, Toshihiro Nakanishi, and Masao Kitano, "Photoinduced Structural Transition in a Checkerboard-like Metasurface," Metamaterials' 2013, Bordeaux, France, accepted (September 2013).

International conferences (poster, refereed)

1. Yosuke Nakata, Takanori Okada, Toshihiro Nakanishi, and Masao Kitano, "Comprehensive circuit-theoretical method for analyzing hybridization modes in metamaterials," META'12, I-13, Paris, France (April 2012).
2. Yosuke Nakata, Takanori Okada, Toshihiro Nakanishi, and Masao Kitano, "Demonstration of flat band for terahertz coupled plasmon in metamaterials with kagomé symmetry," Metamaterials' 2012, Poster No. 22, St. Petersburg, Russia (September 2012).

International conferences (poster, non-refereed)

1. Yosuke Nakata, Takanori Okada, Toshihiro Nakanishi, and Masao Kitano, "A circuit-theoretical method for analyzing coupled modes in metamaterials," The 1st Korea-Japan Metamaterials Forum, Poster-15, Seoul, Korea (July 2011).

2. Yosuke Nakata, Takanori Okada, Toshihiro Nakanishi, and Masao Kitano, "Quantum-mechanical analogy for metamaterials with circuit models and its application," Global COE 5th International Symposium on Photonics and Electronics Science and Engineering, P-38, Kyoto, Japan (March 2012).
3. Yosuke Nakata, Takanori Okada, Toshihiro Nakanishi, and Masao Kitano, "Experimental demonstration of flat band for terahertz spoof plasmon with kagomé symmetry," The 2nd Korea-Japan Metamaterials Forum, P20, Tsukuba, Japan (June 2012).
4. Yosuke Nakata, Takanori Okada, Toshihiro Nakanishi, and Masao Kitano, "Flat band formation in a metallic kagomé lattice," Global COE 6th International Symposium on Photonics and Electronics Science and Engineering, P-18, Kyoto, Japan (March 2013).
5. Yosuke Nakata, Yoshiro Urade, Toshihiro Nakanishi, and Masao Kitano, "Classification of self-dual metasurfaces," The 3rd Korea-Japan Metamaterials Forum, Poster-17, Seoul, Korea (June 2013).
6. Yoshiro Urade, Yosuke Nakata, Toshihiro Nakanishi, and Masao Kitano, "Metamaterial analogue of self-dual electrical circuit," The 3rd Korea-Japan Metamaterials Forum, Poster-7, Seoul, Korea (June 2013).

Domestic conferences (talk)

1. Yosuke Nakata, Takanori Okada, Toshihiro Nakanishi, Kazuhiko Sugiyama, and Masao Kitano, "Terahertz magnetic plasmon on two-dimensional plasmonic kagome lattice," Fall Meeting of the Physical Society of Japan, Osaka (September 2010)
2. Yosuke Nakata, Takanori Okada, Toshihiro Nakanishi, and Masao Kitano, "Terahertz magnetic plasmon on two-dimensional plasmonic kagome lattice II," Annual Meeting of the Physical Society of Japan, Niigata (March 2011)
3. Yosuke Nakata, Takanori Okada, Toshihiro Nakanishi, and Masao Kitano, "General theory to analyze coupled modes in metamaterials modeled by circuits," Fall Meeting of the Physical Society of Japan, Toyama (September 2011)
4. Yosuke Nakata, Takanori Okada, Toshihiro Nakanishi, and Masao Kitano, "Terahertz magnetic plasmon on two-dimensional plasmonic kagome lattice III," Annual Meeting of the Physical Society of Japan, Hyogo (March 2012).
5. Yosuke Nakata, Yoshiro Urade, Toshihiro Nakanishi, and Masao Kitano, "Theoretical analysis for absorption property of self-complementary metasurface," Annual Meeting of the Physical Society of Japan, Hiroshima (March 2013)
6. Yosuke Nakata, "Meta self-duality: from circuits to metasurfaces," Meta X version 3.0 at NAIST, Nara, Japan (August 2013)
7. Yoshiro Urade, Yosuke Nakata, Kosuke Wada, Toshihiro Nakanishi, and Masao Kitano, "Multimode interference in a nested complementary metasurface," Fall Meeting of the Physical Society of Japan, Tokushima (September 2013)
8. Yoshiro Urade, Yosuke Nakata, Toshihiro Nakanishi, and Masao Kitano, "Transition between dual structures in a self-complementary metasurface with semiconductor by photoexcitation," Annual Meeting of the Physical Society of Japan, Hiroshima (March 2013)
9. Takanori Okada, Yosuke Nakata, Koichiro Tanaka, "Optical responses of photo-induced periodic structures in THz region," Fall Meeting of the Physical Society of Japan, Kumamoto (September 2009).
10. Takanori Okada, Yosuke Nakata, Koichiro Tanaka, "Optical responses of photo-induced periodic structures in THz region II," Annual Meeting of the Physical Society of Japan, Okayama (March 2010).